
**Universidad de Valladolid**

Escuela Técnica Superior de Ingenieros de Telecomunicación

Dpto. de Teoría de la Señal y Comunicaciones e Ingeniería Telemática

Tesis Doctoral

# Software solutions for two computationally intensive problems: reconstruction of dynamic MR and handling of alpha-stable distributions.

Presentada por **D. Javier Royuela del Val** para optar al grado de Doctor por la Universidad de Valladolid

Dirigida por:

**Carlos Alberola López y Federico Simmross Wattenberg**

Julio 2017

Valladolid, España

| | |
|---|---|
| Título: *Title:* | Software solutions for two computationally intensive problems: reconstruction of dynamic MR and handling of alpha-stable distributions. |
| Autor: *Author:* | D. Javier Royuela del Val |
| Directores: *Advisors:* | Carlos Alberola López y Federico Simmross Wattenberg |
| Departamento: *Department:* | Teoría de la Señal y Comunicaciones e Ingeniería Telemática |

Tribunal / *Committee*:

| | |
|---|---|
| Presidente: *President:* | Dr. D. Manuel Desco Menéndez |
| Vocal: *Vocal:* | Dr. D. Juan Antonio Hernández Tamames |
| Secretario: *Secretary:* | Dr. D. Santiago Aja Fernández |

acuerda otorgarle la calificación de

En Valladolid, a 7 de julio de 2017

*Let's hope that this is not just a trick. I always live with this feeling. What if I'm tricked? What if I believe into this just because it is beautiful? What if...?*

*Andrei Linde*

*https://youtu.be/ZlfIVEy_YOA*

# ACKNOWLEDGEMENTS

It is not easy to express in a few words all the gratitude deserved to so many people that have helped me during the hard process of getting the work presented this Thesis done.

First of all, I would like to thank my advisors Dr. Carlos Alberola López and Dr. Federico Simmross Wattenberg. Federico opened me the door of the Image Processing Laboratory when I was still an undergraduate student and encouraged me to start a PhD program. His advise and constant availability since then have been fundamental part of my PhD. Moreover, his profound technical knowledge in computing systems and in modeling with $\alpha$–stable distributions have allowed me to develop the efficient implementations presented. Carlos has always supported my work and helped me far beyond the role of a PhD advisor, specially at the moment of writing the papers presented in this Thesis. His general view of the field and identification of main objectives and contributions have definitively shaped my research activity.

I would like to thank Dr. Claudia Prieto and Dr. Muhammad Usman for their outstanding collaboration during my stay at London. There I had the opportunity to get familiar with true MRI raw data for the first time and with the techniques involved in non-Cartesian acquisitions. Most of the work presented in this Thesis with radial acquisitions is based both on data and techniques acquired with them. Thanks also to the people that were at King's during my stay and that made from that time a great experience: Gastao, Christoph, Andy and Ghislain.

I thank Dr. Javier Sánchez, from Philips Ibérica, his support and collaboration in all the technical aspects involving the acquisition of MRI data at the Philips Achieva equipment available at the University of Valladolid.

I am in debt with Dr. Lucilio Cordero Grande, former member of the Image Processing Laboratory. The MRI reconstruction methods presented in this

Thesis are built on top of his seminal idea about the introduction of the group-wise motion estimation technique in the reconstruction procedure. I would also like to thank Santiago Sanz Estébanez his initial implementation of the motion estimation technique in which the finally developed one is based.

Finally, I want to express my endless gratitude to my family for their love and support: my brothers (and sisters–in–law), parents, grand–mother and Ana. I has been a long time, and I could not have made without you. I would like to thank all the current and former members of the Image Laboratory Lab that have been around all these years. I have learn a lot from all of you and you have made the lab a great place to stay.

# ABSTRACT

The availability of ever higher computational power over the last years has changed the way in which multiple scientific and technical problems can be addressed. In this Thesis two computationally intensive problems of interest are faced, namely, the reconstruction of dynamic MR images from highly undersampled data and the numerical computations involved in handling $\alpha$-stable distributions for statistical modeling.

About the former problem, MRI is nowadays the diagnostic imaging technique of first choice for numerous diseases. Its main benefits are its outstanding versatility and soft-tissues contrast. However, it is often limited by the long examination times needed to acquire all the data required to reconstruct the desired images. One way to reduce this time is to reduce the amount of data used for reconstruction, shortening the examination time consequently. However, artifacts arise in the reconstructions as the number of samples is reduced. In order to eliminate these artifacts, some knowledge or *models* can be introduced about the structure of the images of interest during reconstruction. One of the main objectives of this Thesis is to provide a better model for the images under reconstruction than those currently available. In particular the reconstruction of cine cardiac MR images is faced. In this modality the motion of the heart along the cardiac cycle is studied. A model that takes into account not only the structure of the images but also the specific motion of the heart is presented. The model is introduced in a MRI reconstruction scheme adapted for different applications such as breath-hold and free-breathing acquisitions. Results using both simulations and in-vivo measurements from healthy volunteers and patients are presented.

About the latter problem, $\alpha$–stable distributions are a rich class of probability distribution functions of significance in many scientific fields. However, the lack of closed formulae for their probability density function and cumulative distribution function is a major drawback to use them in practice. Numerical

methods have to be used to evaluate them, what involves a high computational demand and hinders, for example, the estimation of their parameters from a data sample. In this Thesis some tools needed for the use of these distributions as a useful statistical model are provided; specifically, we have developed methods for fast and accurate numerical computation of densities and distribution functions as well as for the estimation of $\alpha$–stable parameters. These methods exploit the parallel computing capabilities of modern multi–core systems.

The code generated during the development of this Thesis and the additional supplementary material that can be found in the electronic version of the publications included in this Thesis are avaliable with the electronic version of this Thesis and at the website of the author at

`http:www.lpi.tel.uva.es/~jroyval`

# LIST OF ACRONYMS

**BH** breath–hold

**BLAST** broad-use linear acquisition speed-up technique

**bSSFP** balanced steady state free precession

**BW** backwards

**CDF** cumulative distribution function

**CF** characteristic function

**CS** compressed sensing

**CT** computed tomography

**CWT** complex wavelet transform

**DC** deformation corrected

**DICOM** digital imaging and communication in medicine

**DL** dictionary learning

**DT** dual tree

**ECG** electrocardiogram

**ED** end diastolic

**EF** ejection fraction

**ES** end systolic

**FB** free–breathing

**FFD** free form deformation

**FFT** fast Fourier transform

**FIESTA** fast imaging employing steady–state

**FOCUSS** focal underdetermined system solver

**FOV** field of view

**FT** Fourier transform

**FW** forwards

**GRAPPA** generalized autocalibrating partial parallel acquisition

**GW** groupwise

**HCM** hypertrophic cardiomyopathy

**IR** iterative reconstruction

**kt-SLR** k-t sparse low–rank

**LA** long axis

**LV** left ventricle

**M2D** multi–slice 2D

**MASTeR** motion–adaptive spatio–temporal regularization

**MC** motion compensation

**ME** motion estimation

**ML** maximum likelihood

**MR** magnetic resonance

**MRA** magnetic resonance (MR) angiography

**MRI** magnetic resonance (MR) imaging

**NESTA** Nesterov's algorithm

**NLINV** non–linear inversion

**NUFFT** non–uniform fast Fourier transform (FFT)

**PDF** probability density function

**PI** parallel imaging

**PPG** photoplethysmogram

**PS** partially separable

**PW** pairwise

**RE** registration error

**ROI** region of interest

**RT** real time

**SA** short axis

**SENSE** sensitivity encoding

**SER** signal to error ratio

**SNR** signal to noise ratio

**SSD** sum of squared differences

**SSIM** structural similarity

**TE** echo time

**TR** repetition time

**tTV** temporal TV

**TV** total variation

**VI** variance of the intensity

**XD-GRASP** extra dimensional golden radial sparse

# TABLE OF CONTENTS

**Acknowledgements** **v**

**Abstract** **vii**

**List of Acronyms** **ix**

**Table of contents** **xiii**

**1 Introduction** **1**
- 1.1 Motivation . . . 2
- 1.2 Background . . . 4
- 1.3 Objectives . . . 16
- 1.4 Methodology . . . 17
- 1.5 Thesis overview . . . 21

**2 Non-Rigid Groupwise Registration for Motion Estimation and Compensation in Compressed Sensing Reconstruction of Breath-Hold Cardiac Cine MRI** **25**
- 2.1 Introduction . . . 26
- 2.2 Theory . . . 29
- 2.3 Methods . . . 33
- 2.4 Results . . . 39
- 2.5 Discussion . . . 44
- 2.6 Conclusions . . . 47

**3 Jacobian Weighted Temporal Total Variation for Motion Compensated Compressed Sensing Reconstruction of Dynamic MRI** **51**
- 3.1 Introduction . . . 52

3.2 Theory . . . 53
3.3 Methods . . . 57
3.4 Results . . . 58
3.5 Discussion and Conclusions . . . 62

**4 Single Breath Hold Whole Heart Cine MRI With Iterative Groupwise Cardiac Motion Compensation and Sparse Regularization (kt-WiSE) 67**
4.1 Purpose . . . 67
4.2 Theory . . . 68
4.3 Methods . . . 69
4.4 Results and conclusions . . . 70

**5 Whole-heart single breath-hold cardiac cine: A robust motion-compensated compressed sensing reconstruction method 71**
5.1 Introduction . . . 72
5.2 Methods . . . 74
5.3 Results . . . 78
5.4 Discussion and conclusion . . . 81

**6 Multiresolution Reconstruction of Real-Time MRI with Motion Compensated Compressed Sensing: Application to 2D Free-Breathing Cardiac MRI 85**
6.1 Introduction . . . 86
6.2 Theory . . . 87
6.3 Application to 2D free-breathing cardiac magnetic resonance (MR) imaging (MRI) . . . 90
6.4 Results and discussion . . . 91
6.5 Conclusions . . . 93

**7 Cardio-respiratory Motion Estimation for Compressed Sensing Reconstruction of Free-breathing 2D cine MRI 95**
7.1 Synopsis . . . 95
7.2 Introduction . . . 96
7.3 Methods . . . 97

**8 Libstable: Fast, Parallel and High-Precision Computation of alpha-Stable Distributions in C, MATLAB and R 103**

8.1 Introduction . . . . . 104
8.2 Numerical methods in alpha-stable distributions . . . . . 106
8.3 Algorithms and implementation . . . . . 110
8.4 Results . . . . . 114
8.5 Usage of libstable . . . . . 116
8.6 Conclusions . . . . . 129

**9 Conclusions and future work** **131**
9.1 Contributions . . . . . 131
9.2 Limitations of the current work . . . . . 132
9.3 Future Work . . . . . 134

**Appendix: Resumen en castellano** **137**

CHAPTER

# ONE

# INTRODUCTION

Over the last years, the availability of ever higher computational power and the development of new processing and analysis techniques have changed the way in which multiple scientific and technical problems can be addressed today. As an example, current weather prediction techniques are based on the simulation of advanced climate models rather than on the analytical solution of equations derived from physical laws (Bauer et al., 2015). The reliability of the predictions is determined by the fidelity of the model and the precision with which it is simulated. The quality of the model and the feasibility to *run* it or to *evaluate* it precisely and fast enough is a critical point shared with other scientific fields. As a general rule, the development of more advanced models brings forth to an increase of their computational complexity. As a second example, in the last years iterative reconstruction (IR) methods have re-emerged in computed tomography (CT) imaging (Beister et al., 2012; Geyer et al., 2015). IR methods are able to obtain better images even from lower X-ray radiation doses than their direct counterpart methods at the only expense of a higher computational cost. Although IR methods were proposed in the early stages of the development of CT, only the large capacities of current computational systems have made them a clinically viable option.

In this Thesis we face two computationally intensive problems of interest, namely, the reconstruction of dynamic magnetic resonance (MR) images from highly undersampled data and the achievement of efficiency in numerical computations involved in handling $\alpha$-stable distributions for statistical modeling.

## 1.1 Motivation

Magnetic Resonance Imaging (MRI) is nowadays a key medical image technique that offers outstanding soft tissue contrast and high spatial resolution without the use of ionizing radiation. Moreover, contrast can be made sensitive to a wide range of tissue properties and physical phenomena such as T1/T2 relaxation, proton density, diffusion, flow, etc. (Vlaardingerbroek and Boer, 2003). Since its initial development in the decade of 1970, MRI has benefited from multiple and relevant advances in hardware, with stronger and more homogeneous fields and gradients, new fast excitation sequences such as balanced steady state free precession (bSSFP), and the simultaneous acquisition with several coils in parallel imaging (PI). However, the very nature of the data acquisition procedure as well as technical limitations and human physiological limits make MRI still a relative slow technique when compared to other modalities, such as CT. The need of long acquisition times is a problem specially in dynamic applications, in which the evolution of some phenomenon along time is studied. The available acquisition time is limited by the evolution of the phenomenon, or complex synchronization procedures have to be designed for the acquisition. Motion of the structures under study is a problem as well, since it notably degrades the quality of the final images, a problem that aggravates with long acquisition times.

Both shortcomings take place in breath–hold (BH) cardiac cine MRI, which is considered the gold standard for cardiac anatomical and functional imaging Bogaert et al. (2012). In cine MRI, the cardiac cycle is divided into a number of cardiac phases and an image is obtained for each of them. Given the short duration of a single cardiac phase, data acquisition has to be synchronized with an external signal —typically, an electrocardiogram (ECG) or a photoplethysmogram (PPG)— to combine data from multiple cardiac cycles. Moreover, to avoid respiratory motion, several apneas are required during the examination. In patients with diminished BH capacity this approach results in substantially compromised image quality (Chandarana et al., 2011). A respiratory-navigated, free–breathing (FB) examination can be performed as an alternative; however, it can result in unpredictably long acquisition times. Shortening the needed acquisition time can enable some of these patients to get a regular BH scan and, generally speaking: 1) improves patient comfort and reduces stress, 2) significantly reduces exam duration and the associated economical costs. Therefore, the development of faster acquisition methods is of great importance.

Over the last years, a wide range of new reconstruction techniques have been developed that do not rely on new hardware developments, but in the application of advanced signal processing techniques that allow to reconstruct the images from just a fraction of the data originally needed, shortening acquisition time consequently. These methods exploit the redundancy naturally present in real images. In *low–rank* related methods, data are assumed to be well described by a low dimensional space —with much lower dimensions than the number of data points— (Lingala et al., 2011). This low–rank structure is strictly imposed in partially separable (PS) techniques (Liang, 2007), in which a small set of temporal basis functions are learned from low spatial resolution data. In compressed sensing (CS) theory (Donoho, 2006), the low–dimensional structure is described by a known transform —in this discipline, the *sparse* domain—, in which our image can be represented with a few non zero coefficients. In dictionary learning (DL) methods (Caballero et al., 2014) the basis for the representation is learned from a set of training data.

One relevant drawback of the previous methods is the negative effect of motion in the *low–rankness* or *sparsity* of the images at hand, what limits the quality of the reconstructions and the maximum achievable acceleration factor. Some methods in the literature already address this aspect by introducing some kind of knowledge about this specific motion in the reconstruction procedure (Jung et al., 2009; Asif et al., 2013; Lingala et al., 2014; Mohsin et al., 2017) and have shown that the quality of the reconstruction improves when motion is considered during reconstruction. In these cases, a more complete model of the signal generation is considered, what explains their superior performance. Since we are facing a reconstruction problem, motion has to be extracted from the images under reconstruction themselves, which, in general, will be of limited quality and will also be affected by undersampling artifacts given the accelerated acquisition.

One of the main objectives of this Thesis is to develop and provide a better model for the images under reconstruction in CS based techniques when motion is present. We hypothesize that introducing an accurate and robust motion estimation (ME) technique during reconstruction can increase the sparsity of the representation and therefore the quality of the recovered images will improve for a given acceleration factor or, alternatively, higher acceleration factors will be achieved for the same reconstruction quality.

In the previous paragraphs, the relevance of employing an accurate model is

highlighted. In this aspect, $\alpha$–stable distributions are a rich class of probability distribution functions of significance in many scientific fields that have shown be provide a better model than classical distributions in very different scenarios. The increasing interest on $\alpha$-stable distributions is due, on the one hand, to the empirical evidence that they properly describe the behavior of real data exhibiting impulsiveness or strong asymmetries; on the other hand, the generalized central limit theorem provides theoretical support when the data under study can be interpreted as the superposition of many independent sources. Vegas-Sánchez-Ferrero et al. (2012) use them to characterize speckle noise in medical ultrasonic data and Salas-Gonzalez et al. (2013) to model white and gray matter of the brain in MRI. Li et al. (2014) use them to recover sparse signals under CS theory. Both of these proposals, in turn, have many applications on their own and the list is far from complete.

Nevertheless, the lack of closed formulae for their probability density function (PDF) and cumulative distribution function (CDF) is a major drawback to use them in practice. Numerical methods have to be used to evaluate them, what involves a high computational demand and hinders, for example, the estimation of their parameters from given data. In this Thesis we provide some tools needed for the use of these distributions as a useful statistical model. Methods for fast and accurate numerical computation of densities and distribution functions and for the estimation of $\alpha$–stable parameters are developed; these methods exploit the parallel computing capabilities of modern multi–core systems.

Both MRI reconstruction from highly undersampled data and handling with $\alpha$–stable distributions, although very different in nature, are problems that share a high computational cost as a common property. In this Thesis, careful attention has been paid to the development of efficient implementations in both application domains.

## 1.2 Background

### 1.2.1 Accelerated cardiac MRI

The main reason for MRI being a relatively slow technique is the one–dimensional character of the acquisition procedure. In traditional MRI single lines of k-space data are acquired per repetition time (TR) one after another. The total time to

acquire the needed data is therefore proportional to the number of lines needed to cover the k-space of the image. Even after the advent of bSSFP ultrafast imaging sequences, that allows TR as low as a few milliseconds, the time to acquire a single image is still high. For example, the time needed to acquire a 256x256 image, with a typical TR of 3 ms would be given by:

$$T_{acq} = T_R \times N_y = 3 \cdot 256 = 768\text{ms}$$

For comparison, in a typical setup the cardiac circle is divided in about 20 phases what, for a heart rate of 60 beats per minute, results in 50 ms phases, our temporal acquisition window per phase. Therefore, if no acceleration technique is applied, at least 15 cardiac cycles will be needed to acquire the needed data for the 20 cardiac phases. To complete the examination, between 10 and 16 slices covering the whole heart will be needed. Needless to say, each of these slices is acquired in a separate BH, with resting periods between them.

Reduced data acceleration techniques reduce the imaging time by skipping the acquisition of a fraction of the data needed. The application of an undersampling procedure in the k-space domain will lead to an aliasing effect in the image domain. Different imaging methods differ in the techniques and principles applied to recover from these undersampling artifacts.

In **parallel imaging (PI)**, data are acquired simultaneously by multiple coils or antennas. Even if the same k-space positions are acquired by all the coils, the data they receive are affected by different antenna profiles or *sensitivities*, therefore acquiring different information. In the sensitivity encoding (SENSE) framework, and using a compact matrix vector notation, the signal generation process for each coil can be modeled as (Pruessmann et al., 2001)

$$\mathbf{y}_c = \mathbf{E}_c\mathbf{m} = \mathbf{KFS}_c\mathbf{m} \tag{1.1}$$

where $\mathbf{m}$ is the true MRI image and $\mathbf{y}$ is the undersampled k-t data acquired by all the coils, defined as single column vectors. The encoding operator $\mathbf{E}_c$ consists of the multiplication with the coil sensitivity $\mathbf{S}_c$, the Fourier transform $\mathbf{F}$ and the application of an undersampling mask or trajectory $\mathbf{K}$ which keeps only the acquired k-space positions and is the same for all coils*. The acceleration factor

*When k-space data is acquired following a Cartesian grid, the application of $\mathbf{K}$ corresponds to the extraction of those samples in $\mathbf{FS}_c\mathbf{m}$ that are actually acquired. In non–Cartesian acquisitions, $\mathbf{K}$ typically involves a *degridding* step in which non–Cartesian positions within the grid are interpolated by means of a convolution kernel.

$R$ is given by the ratio of the total number k-space positions (rows in $\mathbf{F}$, equal to the length of $\mathbf{m}$) and the number of acquired positions (number of rows in $\mathbf{K}$). The data from all coils can be expressed simultaneously just by droping the coil index and considering the concatenation of the data from all the coils:

$$\mathbf{y} = \mathbf{E}\mathbf{m} = \begin{bmatrix} \mathbf{KFS}_1 \\ \mathbf{KFS}_2 \\ \vdots \\ \mathbf{KFS}_{N_c} \end{bmatrix} \mathbf{m} \tag{1.2}$$

The reconstruction problem can then be formulated as solving the system of linear equations in Eq. 1.2. As long as $R$ is lower than the number of coils ($N_c$), the system can be solved in a minimum squared error sense and $\mathbf{m}$ recovered. However, in real situations, the maximum achievable acceleration factor is limited by several factors such as noise, coil geometry, model errors and numerical instabilities that aggravate as $R$ increases.

The reconstruction problem can take advantage of redundancy naturally present in the data. In classical approaches, such as UNFOLD (Madore et al., 1999), k-t BLAST/SENSE (Tsao et al., 2003), data are acquired following a regular pattern in k-t space that leads to coherent aliasing in the spatio–temporal domain ($x$-$t$). The one dimensional Fourier transform (FT) transform can be applied to lead to a mixed spatio–temporal frequency representation (the $x$-$f$ domain) in which the signal spatio–temporal correlation leads to a compact representation. In this space, aliasing can be easily eliminated by filtering out the non–overlapping replicas. In k-t GRAPPA (Huang et al., 2005) the reconstruction is carried out in the k-space. A detailed review on these classical approaches has been published by Tsao and Kozerke (2012).

### 1.2.2 Compressed Sensing and Low–Rank techniques

More recently, **compressed sensing (CS)** theory (Candès et al., 2006; Donoho, 2006) has been successfully applied to MRI reconstruction (Lustig et al., 2007; Otazo et al., 2010; Usman et al., 2013; Chen et al., 2014; Feng et al., 2013; Lingala et al., 2015; Yoon et al., 2014). CS states that when an image can be represented by a small number of non–zero coefficients in some known transformation domain, it can be recovered from a small number of incoherent measurements.

Under this assumption, an in combination with PI, the reconstruction problem can be formulated as

$$\underset{\mathbf{m}}{\text{minimize}} \|\mathbf{\Phi m}\|_{\ell 1} \;\; s.t. \;\; \|\mathbf{y} - \mathbf{Em}\|_{\ell 2}^2 < \epsilon \tag{1.3}$$

where $\mathbf{\Phi}$ is the sparsifying transform. The threshold $\epsilon$ accounts for the noise level in the acquisition, thus allowing the final solution to deviate from the observed data. The constrained optimization problem in Eq. (1.3) can be converted into an unconstrained problem using a Lagrangian multiplier as follows:

$$\underset{\mathbf{m}}{\text{minimize}} \frac{1}{2} \parallel \mathbf{y} - \mathbf{Em} \parallel_{\ell_2}^2 + \lambda \parallel \mathbf{\Phi m} \parallel_{\ell_1} \tag{1.4}$$

where the parameter $\lambda$ establishes a trade off between data consistency and the sparsity of the solution, enforced by the $\ell_1$ norm term. Eq. 1.4 can be regarded as a regularized form of the linear reconstruction in Eq. 1.2.

In the CS theory (Donoho, 2006; Candès et al., 2006), the sparsity transform $\mathbf{\Phi}$ has to be fixed beforehand, based on some previous knowledge on the structure of the data. For example, in dynamic applications in which consecutive images are expected to be very similar, temporal differences can be applied to obtain a sparse representation, leading to temporal total variation (TV) methods such as kt-SPARSE-SENSE Feng et al. (2013).

Other methods have been proposed in which there is no need to know a specific transform. They rely on the more relaxed assumption that data can be well described in a low dimensional space —with far lower dimensions than the number of data points— , which is generally described as a **low–rank** structure. In PS techniques (Liang, 2007) a two-step procedure is followed. In a first step, a small set of temporal basis functions are learned from low spatial/high temporal resolution training data. In a second step, the whole sequence of images is reconstructed from a small number of measurements using the predetermined temporal basis as a signal model. The low–rank structure is therefore strictly imposed and fixed by the number of temporal basis used during reconstruction, that must be selected beforehand.

A more flexible approach is presented by (Lingala et al., 2011) in the k-t sparse low–rank (kt-SLR) method in which a low–rank constrain is directly introduced in the reconstruction. Both the temporal basis and the spatial weights are jointly estimated by solving:

$$\underset{\mathbf{M}}{\text{minimize}} \;\; \|\mathbf{y} - \mathbf{EM}\|_{\ell 2}^2 \;\; s.t. \;\; \text{rank}(\mathbf{M}) < r \tag{1.5}$$

In this case, the image under reconstruction $\mathbf{m}$ has been properly rearranged into a matrix form $\mathbf{M}$ so temporal and spatial correlations can be exploited. The rest of the terms are expressed with the same notation as in Eq. 1.3 to highlight the relation between both approaches.

The above constrained problem can be converted into an unconstrained one using Lagrange's multipliers and the rank penalty substituted by a spectral penalty term that promotes the low–rank structure of the solution. Moreover, an additional sparsity based regularization term is added:

$$\underset{\mathbf{M}}{\text{minimize}} \quad \|\mathbf{y} - \mathbf{E}\mathbf{M}\|_{\ell 2}^2 + \lambda_1 \varphi(\mathbf{M}) + \lambda_2 \psi(\mathbf{M}) \tag{1.6}$$

with

$$\varphi(\mathbf{M}) = \left( \sum_{l=1}^{L} \|\sigma_l\|^p \right)^{1/p} \quad ; \qquad \psi(\mathbf{M}) = \|\mathbf{M}\|_{TV} \tag{1.7}$$

where $\sigma_l$ are the singular values of $\mathbf{M}$ and $\|\cdot\|_{TV}$ stands for the spatio–temporal TV. It can be shown that for $p \leq 1$ Eq. 1.6 promotes solutions with few non–zero singular values (and, therefore, with low–rank structure) and at the same time with a sparse representation in the spatio–temporal differences space.

Low–rank methods have been specially successful in MRI perfusion imaging, in which the time evolution of the concentration of a contrast agent leads to intensity variations in the images along time. In this situation, the temporal evolution of the intensity profile can be assumed to be *smooth* and the low–rankness assumption promotes solutions with this behavior. On the contrary, in cardiac cine MRI the intensity fluctuations of a single pixel along time is, under ideal conditions, due only to the motion of the structures of the heart, leading to abrupt intensity fluctuations.

In this thesis we are interested in the effect of motion in the sparsity of cardiac cine images under reconstruction and how to compensate this effect to improve the quality of the reconstructed images and to achieve higher acceleration factors. To this end, we focus on CS based methods combined with ME techniques, which are introduced in the next section.

### 1.2.3 Compressed Sensing with Motion Compensation

When motion is present in the images being reconstructed, the *low–rankness* or *sparsity* of the signals at hand gets significantly reduced, what limits the

quality of the reconstructions and the maximum achievable acceleration factor. In order to overcome this limitation, in CS with ME/motion compensation (MC) the sparsity transform operator $\mathbf{\Phi}$ in Eq. 1.3 is modified to compensate the motion present in the images so the low–rank or sparse character of the images is restored.

In k-t focal underdetermined system solver (FOCUSS) with ME/MC (Jung et al., 2009) the unknown image $\mathbf{m}$ is decomposed into a predicted, $\mathbf{m}_{\text{pred}}$, and a residual image, $\Delta\mathbf{m}$:

$$\mathbf{m} = \mathbf{m}_{\text{pred}} + \Delta\mathbf{m} \tag{1.8}$$

The predicted signal $\mathbf{m}_{\text{pred}}$ is obtained by applying a block matching algorithm between each frame of $\mathbf{m}$ and a reference frame $\mathbf{m}_{\text{ref}}$. Since neither $\mathbf{m}_{\text{ref}}$ nor the true dynamic image are available for ME, a previous reconstruction step is performed with the original k-t FOCUSS algorithm without ME/MC proposed by Jung et al. (2007).

The residual signal is assumed to be sparse in the x-f domain, so the FT is applied along the temporal dimension and the reconstruction is formulated as

$$\underset{\mathbf{m}}{\text{minimize}}\ \frac{1}{2}\parallel \mathbf{y} - \mathbf{E}\mathbf{m} \parallel_{\ell_2}^2 + \lambda\|\mathbf{F}_{\text{t}}\Delta\mathbf{m}\|_{\ell_1} \tag{1.9}$$

On the other side, the motion–adaptive spatio–temporal regularization (MASTeR) procedure proposed by Asif et al. (2013) does not rely on a reference frame, but motion is estimated sequentially between each pair of consecutive frames to define a set of operators that predict each frame $\mathbf{m}_i$ out of its leading and trailing frames:

$$\begin{aligned} \mathbf{m}_i &= \mathcal{F}_{i-1}\mathbf{m}_{i-1} + \mathbf{f}_i \\ \mathbf{m}_i &= \mathcal{B}_{i+1}\mathbf{m}_{i+1} + \mathbf{b}_i \end{aligned} \tag{1.10}$$

where $\mathcal{F}_{i-1}$ and $\mathcal{B}_{i+1}$ denote the forward and backward MC operators. Residuals $\mathbf{f}_i$ and $\mathbf{b}_i$ are assumed to be sparse and are used as sparsity term:

$$\underset{\mathbf{m}}{\text{minimize}}\ \frac{1}{2}\parallel \mathbf{y} - \mathbf{E}\mathbf{m} \parallel_{\ell_2}^2 + \parallel \mathcal{M}\mathbf{m} \parallel_{\ell_1} \tag{1.11}$$

where $\mathcal{M}\mathbf{m}$ is the concatenation of the residual terms in Eq. (1.10).

The images used for ME are generally obtained from an initial reconstruction and will be affected by undersampling artifacts that the initial reconstruction procedure cannot eliminate. The ME stage can therefore be affected by these

artifacts and these errors will affect the quality of the reconstructed images. In the methods described so far, only the information of pairs of frames are available to the ME technique. In this Thesis we introduce a groupwise (GW) ME technique during reconstruction that uses the information from the whole sequence jointly. This way we obtain a robust motion ME technique an analyze how this translates into a higher quality of the reconstructed images.

### 1.2.4 Free–breathing acquisitions

In conventional cardiac cine MRI, only the beating motion of the heart is present, since during the acquisition the patient is asked to hold his/her breath. However, this approach significantly limits the time available for data acquisition. Spatio–temporal resolution and spatial coverage are consequently limited. Moreover, patients may have difficulties to hold their breath. A common alternative is to perform FB gated acquisition, in which a signal that indicates the position of the patient's diaphragm is registered. MRI data are then acquired only within a small gating window around certain respiratory state. This approach largely increases the duration of the examination and leads to unpredictably long scans, since useful data are acquired only during a small fraction of the available time.

In order to increase the scanning procedure efficiency several techniques have been proposed with a similar approach than those based on the estimation of the motion of the heart described above. Usman et al. (2013) propose to acquird data continuously using an efficient radial k-space acquisition scheme (Winkelmann et al., 2007). Low temporal resolution images are reconstructed that will, indeed, be affected by both respiratory and cardiac motions. However, respiratory motion can be estimated from these images and compensated in a second step, in which respiratory motion-free images are obtained.

Feng et al. (2016) follow a different approach in extra dimensional golden radial sparse (XD-GRASP) reconstructions. In this approach, data are continuously acquired and doubly classified or binned according to both the respiratory state and the corresponding cardiac phase at which the data were acquired. The acquisition and binning procedure is graphically depicted in figure 1.1. The final images are then reconstructed using a CS formulation with two temporal TV regularization terms, in which the temporal differences along either the cardiac or the respiratory phases are computed:

$$\underset{\mathbf{m}}{\text{minimize}}\ \frac{1}{2} \parallel \mathbf{y} - \mathbf{E}\mathbf{m} \parallel_{\ell_2}^2 + \lambda_1 \parallel \mathbf{m} \parallel_{TV_{cardiac}} + \lambda_2 \parallel \mathbf{m} \parallel_{TV_{respiratory}} \qquad (1.12)$$

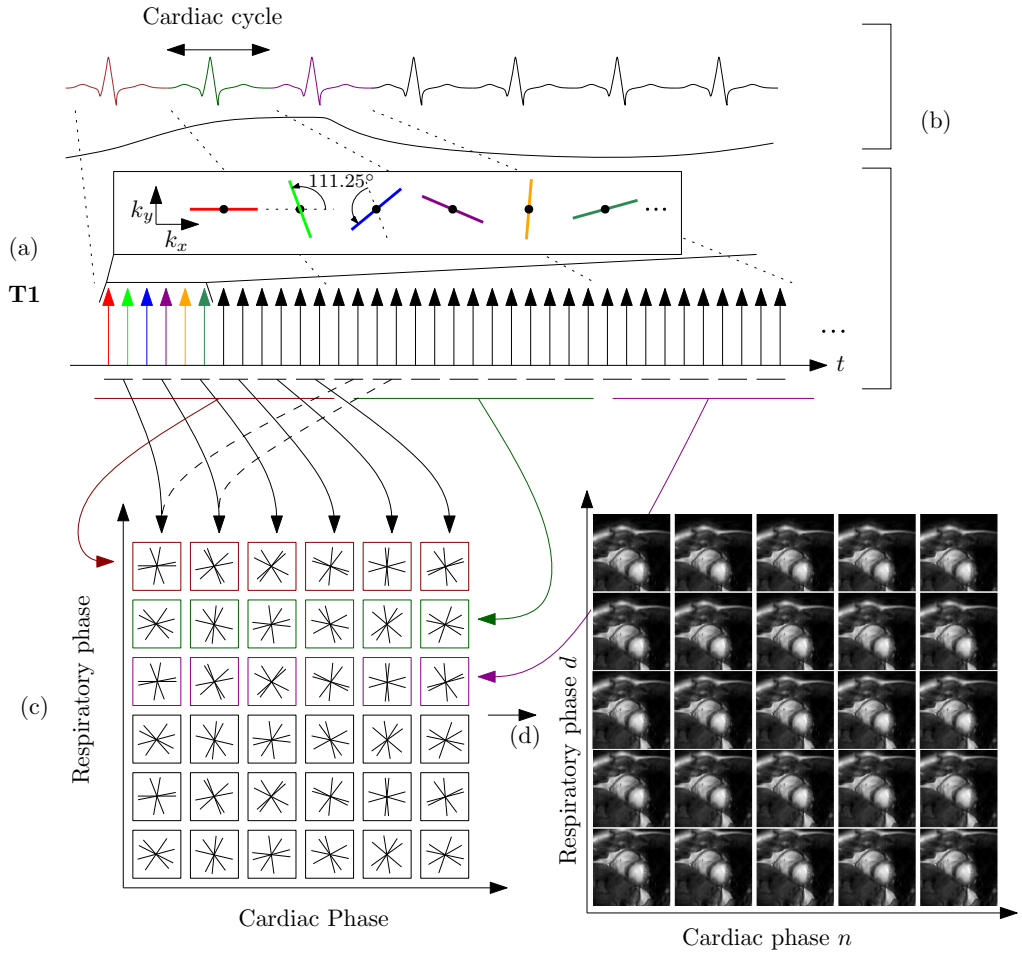


Figure 1.1: (a) Continuous acquisition with a golden-angle radial trajectory in k-space. (b) ECG and respiratory signal are simultaneously acquired and (c) data doubly binning according to respiratory and cardiac motion. (d) Reconstructed images with two-pseudo temporal dimension corresponding to cardiac and respiratory phases.

Under the XD-GRASP framework, a set of images is obtained arranged in a two dimensional lattice, which defines two pseudo–temporal dimensions: one for the cardiac phase and another one for the respiratory state. No correction for the respiratory or the cardiac motion has been carried out. In this thesis we propose to modify the temporal TV term in Eq. 1.12 to account for the specific cardio–respiratory motion.

### 1.2.5 Methods for $\alpha$–stable distributions

$\alpha$-stable distributions are a family of probability distributions that permit adjustable levels of heavy tails and skewness and include distributions such as Gaussian, Cauchy and Lévy as particular cases. They were first introduced by Lévy (1925) and have since been applied in many research fields. The increasing interest on $\alpha$-stable distributions is due, on the one hand, to the empirical evidence that they properly describe the behavior of real data exhibiting impulsiveness or strong asymmetries; on the other hand, the generalized central limit theorem (Samorodnitsky and Taqqu, 1994) states that the normalized sum of independent and identically distributed random variables with finite or infinite variance converges, if so, to an $\alpha$-stable distribution. This result provides theoretical support when the data under study can be interpreted as the superposition of many independent sources.

The major drawback for the application of $\alpha$-stable models is the lack of closed-form analytical expressions for their probability density function (PDF) or cumulative distribution function (CDF) except in particular cases, which makes the application of numerical methods a must. Besides, the non-existence of moments of order two or higher (except in the Gaussian case) increases the difficulty in estimating their parameters to fit real data. Several authors have addressed both the numerical evaluation of the PDF or CDF of $\alpha$-stable distributions (Nolan, 1997; Mittnik et al., 1999a; Belov, 2005; Menn and Rachev, 2006; Górska and Penson, 2011) and the estimation of their parameters (Fama and Roll, 1971; Koutrouvelis, 1981; McCulloch, 1986; Mittnik et al., 1999b; Nolan, 2001; Fan, 2006; Salas-Gonzalez et al., 2009) and have proposed different methods and algorithms for these purposes.

### Characteristic Function and Parametrization

$\alpha$-stable distributions are typically described by their characteristic function (CF) due to the fact that no closed expressions exist for their PDF in the general case. Let $\Phi(t) = \exp[\Psi(t)]$ denote this function with (Samorodnitsky and Taqqu, 1994):

$$\Psi(t)=\begin{cases} -|\sigma t|^{\alpha}\left[1-i\beta\tan\left(\frac{\pi\alpha}{2}\right)\operatorname{sign}(t)\right]+i\mu t, & \alpha\neq 1, \\ -|\sigma t|\left[1+i\beta\frac{2}{\pi}\operatorname{sign}(t)\ln\left(|t|\right)\right]+i\mu t, & \alpha=1, \end{cases} \tag{1.13}$$

where

$$\operatorname{sign}(t) \quad = \quad \begin{cases} 1, & t>0, \\ 0, & t=0, \\ -1, & t<0. \end{cases}$$

The four parameters above are (1) the stability index $\alpha \in (0, 2]$, (2) the skewness parameter $\beta \in [-1, 1]$, (3) the scale parameter $\sigma > 0$ and (4) the location parameter $\mu \in \mathbb{R}$. An $\alpha$-stable distribution is referred to as standard if $\sigma = 1$ and $\mu = 0$. When $\alpha = 2$ the distribution becomes normal with standard deviation $\sigma/\sqrt{2}$ and mean $\mu$ ($\beta$ becomes irrelevant). The Cauchy distribution results from setting $\alpha = 1$ and $\beta = 0$ with scale parameter $\sigma$ and location parameter $\mu$, and the Lévy distribution when $\alpha = 0.5$ and $\beta = 1$. These are the only cases for which the PDF can be expressed analytically. Otherwise, the PDF has to be calculated numerically.

### Numerical computation of $\alpha$-stable distributions

The PDF and CF of any probability function are related via the well known Fourier transform

$$f(x) = \frac{1}{2\pi}\int_{-\infty}^{+\infty}\phi(t)\mathrm{e}^{-itx}\,\mathrm{d}t = \frac{1}{2\pi}\int_{-\infty}^{+\infty}\mathrm{e}^{\psi(t)-itx}\,\mathrm{d}t. \tag{1.14}$$

When substituting Equation 1.13 in Equation 1.14 the resulting integral cannot be, as a rule, solved analytically; therefore it must be evaluated by numerical methods. To this end, the well-known fast Fourier transform (FFT) provides an algorithm to efficiently evaluate the previous integral. Mittnik et al. (1999a) apply the FFT directly to calculate the PDF. However, the algorithm provides the value of the integral on a set of evenly spaced points of evaluation and is only suitable for $\alpha$ close to 2, for which the tails of the distribution decay more

quickly. Menn and Rachev (2006) propose a method based on a refinement of the FFT to increase precision in the central part of the PDF. The tails of the distribution are calculated via a series expansion (Zolotarev, 1986), which provides an alternative expression as an infinite sum of decaying terms. The method is only applicable when $\alpha > 1$.

Górska and Penson (2011) follow a different approach and obtain explicit expressions for the PDF and CDF as series of generalized hypergeometric functions. However, the expressions involved in the calculation are expensive to evaluate and the results are only valid for some rational values of the parameters $\alpha$ and $\beta$, so they are not valid for the whole parameter space.

Direct integration of the expression in Equation 1.14 by numerical quadrature initially implies a high computational cost, but evaluation can be performed at any desired set of points without the need of additional interpolation steps and there is no restriction on the values of the distribution parameters. However when $\alpha$ is small the integrand oscillates very quickly and its amplitude decays slowly along the infinite integration interval, which limits the achievable precision Nolan (1999); Belov (2005).

Nolan (1997) obtains a new set of equations from the original ones by means of an analytic extension of the integrand to the complex plane. This way, a continuous, bounded, non-oscillating integrand is obtained. Moreover, the integration interval becomes finite. The expressions obtained allow the author to achieve, by numerical quadrature, a relative accuracy in the order of $10^{-14}$ in most of the parameter space. For numerical convenience, a slightly different parameterization of the distribution is employed, based on Zolotarev (1986) M parameterization. The modification introduced consists in a shift of the distribution along the abscissae axis in order to avoid the discontinuity of the distribution at $\alpha = 1$. We denote the change in parameterization by the subindex 0 and the resulting CF is given by $\Phi_0(t) = \exp[\Psi_0(t)]$ where

$$\Psi_0(t)=\begin{cases}-|\sigma t|^{\alpha}\left[1+i\beta\tan\left(\frac{\pi\alpha}{2}\right)\mathrm{sign}(t)\left(|\sigma t|^{1-\alpha}-1\right)\right]+i\mu_0 t, & \alpha\neq 1,\\ -|\sigma t|\left[1+i\beta\frac{2}{\pi}\mathrm{sign}(t)\ln\left(|\sigma t|\right)\right]+i\mu_0 t, & \alpha=1.\end{cases} \tag{1.15}$$

The parameters $\alpha$, $\beta$ and $\sigma$ keep their previous meaning while the original and modified location parameters $\mu$ and $\mu_0$ are related according to

$$\mu = \begin{cases} \mu_0 - \beta\tan\left(\frac{\alpha\pi}{2}\right)\sigma, & \alpha \neq 1,\\ \mu_0 - \beta\frac{2}{\pi}\sigma\ln(\sigma), & \alpha = 1. \end{cases} \tag{1.16}$$

With this modification, the resulting distribution is continuous in its four parameters, which is convenient when estimating the parameters of the distribution or approximating its PDF or CDF.

### Parameter estimation of $\alpha$-stable distributions

The lack of closed expressions for the PDF or CDF and the lack of finite higher order moments hinder the estimation of $\alpha$-stable parameters. Several methods have been proposed to this end. Hill (1975) and Koutrouvelis (1981) proposals apply a linear regression on the right tail of the empirical distribution and McCulloch (1986) provides a fast and simple algorithm based on sample quantiles and tabulated values. Maximum likelihood (ML) estimation is considered the most accurate estimator available for $\alpha$-stable distributions (Borak et al., 2011). However, numerical methods to both approximate the PDF and to maximize the likelihood of the sample must be used, which implies a very high computational cost due to the numerous PDF evaluations required to maximize the likelihood in the four-dimensional parameter space.

### Generation of $\alpha$-stable random variables

Given the lack of closed expressions for the CDF or its inverse (the quantile function, $\text{CDF}^{-1}$), the simulation of $\alpha$-stable distributed random variables cannot be achieved easily from a uniform random variable. Chambers et al. (1976) provided a direct method to generate an $\alpha$-stable random variable by means of the transformation of an exponential and a uniform random variable. The method proposed lacked a theoretical demonstration until Weron (1996) gave an explicit proof and slightly modified the original expressions. The resulting method is regarded as the fastest and the most accurate available (Weron, 2004).

### Available software solutions

Based on the methods described so far, several software tools are currently available. The program STABLE (Nolan, 2006) employs Nolan's expressions (Nolan, 1997) for the high precision computation of PDF, CDF and quantile function and maximum likelihood parameter estimation. However, a fully operational version of the software is not publicly available. Veillete (2010) has developed a

MATLAB package that also applies Nolan's expressions for high precision PDF and CDF evaluation and Koutrouvelis (1981) method for parameters estimation based on the CF. However, the performance obtained is low when trying to achieve high precision or when fitting a large data sample. A package with similar features and characteristics has been reported by Liang and Chen (2013).

## 1.3 Objectives

The main objective of this Thesis is **to propose and to apply better models as well as to provide the necessary tools to this end in two computationally intensive problems: the reconstruction of dynamic MR images from highly undersampled data and the application of $\alpha$–stable distributions for statistical modeling.**

The main objective can be divided in the following individual objectives:

1. To propose a better model for the reconstruction of dynamic MR images from highly undersampled data that takes into account not only the sparsity present in natural images, but also the time redundancy of the motion that takes place in those images, as well as to provide the software tools needed for its application. In particular, we focus on the reconstruction of cine cardiac MR images, in which the motion of the heart along the cardiac cycle is studied.

   To this end, we define the following sub-objectives:

   (a) To propose and to implement a technique for the estimation of the heart motion along the cardiac cycle. The proposed ME technique must be sufficiently flexible so as to describe the non-rigid heart motion accurately and, simultaneously, sufficiently robust against the artifacts present in the images obtained from highly undersampled data.

   (b) To propose and to develop dynamic MRI reconstruction methods that incorporate the knowledge about the heart motion in the procedure in order to obtain a sparser representation of the images at hand and to test the hypothesis about the effect of the introduction of the motion information by comparing the results obtained with those from related methods that 1) do not consider motion at all or 2) apply different ME techniques not so robust against undersampling.

(c) To propose and to develop an extension of the ME and reconstruction methods that is able to incorporate not only the motion of the heart along the cardiac cycle but also the respiration-induced chest motion, in order to enable acquisition times longer than the duration of a breath–hold. This would make the accelerated MRI methods suitable to free–breathing applications.

(d) To test the feasibility of the proposed method to obtain correct values of commonly used cardiac function indicators, namely, ventricular volumes and ejection fraction (EF).

(e) For each of the previous sub-objectives, to develop an efficient implementation that exploits the parallel computing capabilities of modern multi–core systems.

2. To develop the needed tools to apply the $\alpha$–stable distribution as a statistical model in a feasible manner. To this end:

(a) To develop and to implement a technique for the numerical evaluation of the PDF, CDF and quantile function of $\alpha$–stable distributions with high precision and taking advantage of the parallel computation capabilities of current computation systems.

(b) To develop and to implement a technique for the estimation of the parameters of an $\alpha$–stable distribution from a given sample that facilitates the application of these distributions as a first order statistical model.

(c) To test the performance and precision of the developed techniques in comparison with other alternatives available in the literature implemented with different languages and tools.

(d) To provide an easy-to-use software solution based on the developed tools and to integrate it in common programming languages and scientific programming environments.

## 1.4 Methodology

In this section the methodology applied throughout the Thesis is described and the contributions presented in the subsequent chapters are related to each other.

### 1.4.1 2D Dynamic MR imaging

As previously described, one the the main objectives of this Thesis is to validate the hypothesis that introducing an accurate and robust ME technique improves the results obtained in CS based reconstructions. Therefore, and throughout all the work presented in this Thesis, comparisons and validations have been carried out against related CS methods and the effect of the ME in the sparsity of the images analyzed.

The validation experiments have been realized using four different sources of data, when applicable:

1. Synthetically generated k–space data using the XCAT tool (Segars et al., 2010; Wissmann et al., 2014), in which the exact solution (i.e., the images) and the motion are known beforehand. This permits to evaluate the performance of the proposed methods both in ideal conditions and when controlled signal degradations are introduced, and for different acceleration factors. However, synthetically generated functions are in general simpler —so sparser— than real images, what facilitates their reconstruction.

2. Simulated k–space data obtained from magnitude DICOM images both from healthy subjects and patients. This permits to validate the method for images with a more realistic structure than synthetic ones and in subjects with different heart abnormalities. However, in this data phase information in the originally complex images is lost.

3. True raw k–space data obtained from Cartesian fully sampled acquisitions. This permits to validate the proposed methods in a realistic situation. Data are retrospectively undersampled to simulate different acceleration factors.

4. True raw k–space data obtained from Golden Radial acquisitions. In this approach data are continuously acquired and different acceleration factors are obtainted by setting the acquisition time or temporal resolution, when applicable.

We have first tackled the problem by introducing groupwise non–rigid registration techniques as a robust ME procedure for cardiac cine images. This methodology was first proposed by our group (Cordero-Grande et al., 2013) for

breathing-derived misalignment correction in first-pass cardiac perfusion imaging and has been adapted in this thesis to the cine problem. In the former, an elastic multimodal approach was used since not only breathing-derived misalignment was considered (for which possibly rigid registration may be argued to suffice), but also artifacts derived from ECG gating imprecisions were observed in our datasets. However, for the cine problem the heart motion along the whole cardiac cycle should be estimated and compensated for, in order for sparsity in the whole time sequence to be fostered and better reconstructions be obtained. These ideas are introduced in a standard CS with SENSE PI based scheme (Liang et al., 2009; Otazo et al., 2010) for the reconstruction of short axis (SA) views of the heart in BH cine MRI. The resulting reconstruction method provides better quality (considering both qualitative and quantitative metrics) than the related methods considered, including those which make use of alternative non–groupwise ME methods. **Chapter 2**, which constitutes the first core paper on which this thesis is based, explains in detail these ideas.

The method just described incorporates in the optimization function two regularization terms that account for both spatial and temporal regularization. Consequently, the method makes use of two weighting parameters that need to be set from some *training data*. This has been improved by proposing a new regularization metric for the reconstruction problem that 1) shows convenient discretization properties that leverage computational cost, 2) provides theoretical support to some results previously reported in chapter 2 and 3) enables the elimination of the spatial regularization term which, additionally, reduces computational cost and reconstruction time and reduces the number of weighting parameters to just one, simplifying its practical application, consequently. The effects of both the new regularization metric and the removal of the spatial regularization are analyzed separately. The robustness of the method is tested by using very different initial guesses, which have led the algorithm to converge to almost identical solutions. These ideas are described in detail in **Chapter 3**, which constitutes the second core paper of the thesis.

We have proposed the former two methods for Cartesian k-space trajectories originally. However, we have had the chance to make use of a more advanced data acquisition scheme based on Golden Radial trajectories proposed by Winkelmann et al. (2007). This more efficient data acquisition procedure enables higher acceleration factors and, specifically, we could achieve the reconstruction of a stack of 12 SA slices covering the whole heart acquired in a single

BH for a healthy volunteer. The reconstruction method used is the adaptation of chapter 2 to this type of coordinates. **Chapter 4** describes the result of this work, which was possible thanks to our collaboration with Claudia Prieto and Muhammad Usman, from King's College London, UK.

Next step has been the inclusion of Golden Radial trajectories to the methodology described in chapter 3. In addition, we meant to test the robustness of both the ME and the reconstruction methods against noise. This has been done by means of simulation using a computational phantom (Segars et al., 2010). In this case, since we know the ground truth, numerical studies can be carried out. In addition, eight healthy volunteers are examined with the single BH accelerated method proposed and global cardiac functional parameters have been calculated from the images. These indicators are in agreement with those obtained from regular, non–accelerated, multi-BH acquisitions, so we can conclude that the accelerated single-BH proposed method is a feasible tool for the quantification of the global function of the heart. Details are described in **Chapter 5**.

We have also meant to apply our methods to real time MRI of the heart. In this case, as opposed to in those previously described, patient breathing will be present and should be correctly accounted for, together with the natural heart motion. In this case we have resorted to a temporal multiresolution pyramid for successive reconstructions; at the coarsest level of the pyramid we obtain preliminary CS reconstructions by making use of multiple k-space lines that come from different phases of the cardiac cycle. Therefore, these images will show clear motion blurring and derived degradations. However, successive levels of the pyramid will be constructed out of these images by balancing two sources of data, namely, the original measured data and motion-compensated intermediate images in between those reconstructed in the upper level of the pyramid. Temporal resolution of 25ms with an in-plane spatial resolution of 2mm was achieved with better image quality than related methods. This is described in **Chapter 6**.

Even though the results of the previous chapter enable imaging the moving heart during FB, the short acquisition time available in real time acquisitions, given by the desired temporal resolution, limits the achievable image quality and spatial resolution. In order to overcome this limitation, while keeping free-breathing capabilities, we have followed a different methodology; in this case, the acquired data are double binned attending to both the cardiac and the respiratory phases at which they are acquired. This approach results in two major

differences with respect to the previous chapters: 1) now the acquisition time is not limited by either the temporal resolution or patient breath-hold capability of the patient; 2) now both respiratory and cardiac motions can be distinguished. The ME technique is adapted to represent both cardiac and respiratory motions. Results on synthetic and real data are shown in **Chapter 7**. At the time of the writing of this document, we also have results on volunteers.

### 1.4.2 $\alpha$-stable distributions

As indicated above, calculations related to the $\alpha$-stable distributions are computationally demanding due to the lack of closed form expressions. Our contribution in this field has been on parallel programming. Specifically, we have developed a library that offers highly parallelized, fast and high precision evaluation of density, distribution and quantile functions, random variable generation and several $\alpha$–stable parameter estimation algorithms. A 25–fold increase on performance was achieved in the computation of the $\alpha$–stable PDF when compared with a state–of–the–art, standalone compiled application and a 100–fold improvement when compared with a standard R implementation. These increases in performance facilitate the application of this versatile family of probability functions to the analysis and modeling of any kind of data. The developed tools are provided in the form of a C/C++ library and front-ends for MATLAB and R. These tools have been registered in the Spanish copyright protection office. **Chapter 8** gathers our main contribution in the application of the $\alpha$-stable distributions as a statistical model. This constitutes the third core paper of the thesis.

## 1.5 Thesis overview

A graphical outline of the Thesis context is shown in Figure 1.2. The following list of publications summarizes the scientific production of the Thesis. We include references to other papers in which the PhD candidate has been involved during the completion of this degree. The main contributions, limitations of the described approaches and future research lines are presented in Chapter 9.

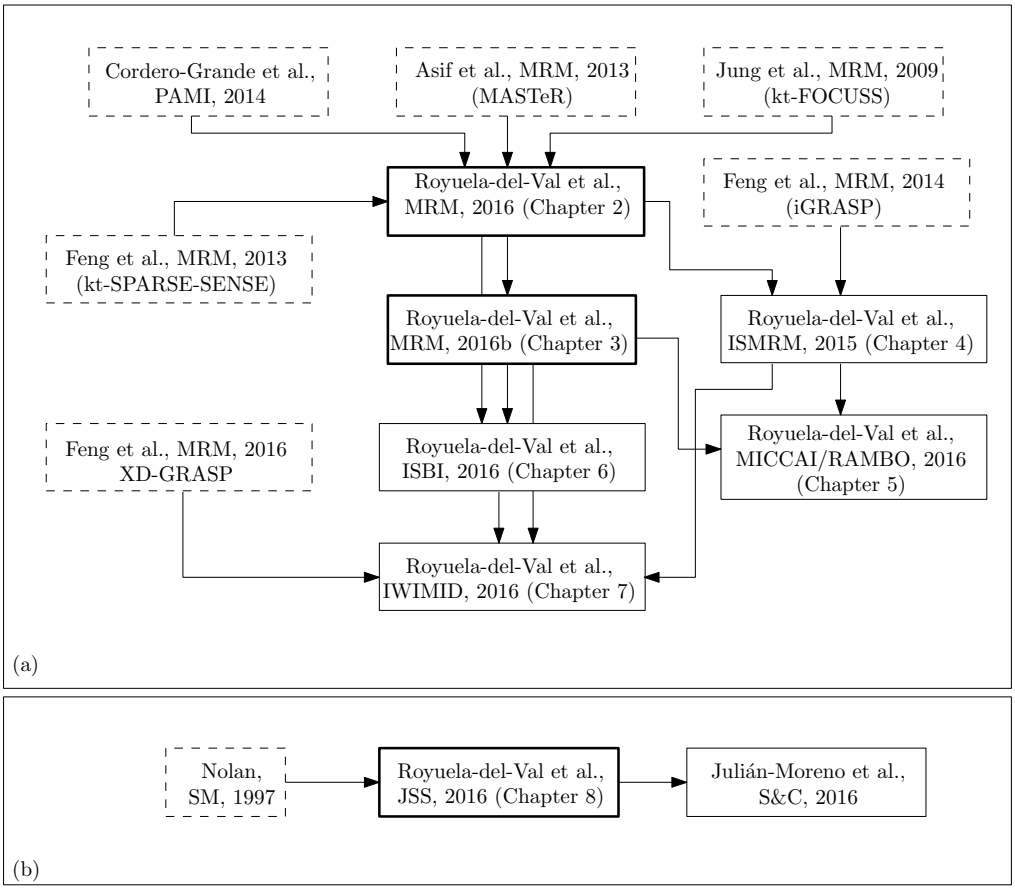


Figure 1.2: Graphical outline of the Thesis context in the fields of (a) MRI reconstruction and (b) $\alpha$–stable distributions. Core papers are represented in darker boxes. Some relevant contributions from other authors that inspired or served as an important basis for this work are included and represented with dashed lines.

### 1.5.1 List of publications

**Core papers**

- **Chapter 2:** Royuela-del Val, J., Cordero-Grande, L., Simmross-Wattenberg, F., Martín-Fernández, M., and Alberola-López, C. (2016a). Nonrigid groupwise registration for motion estimation and compensation in compressed sensing reconstruction of breath-hold cardiac cine MRI. *Magnetic Resonance in Medicine*, 75(4):1525–1536.

- **Chapter 3:** Royuela-del Val, J., Cordero-Grande, L., Simmross-Wattenberg, F., Martín-Fernández, M., and Alberola-López, C. (2017a). Jacobian weighted temporal total variation for motion compensated compressed sensing reconstruction of dynamic mri. *Magnetic Resonance in Medicine*, 77(3):1208–1215.

- **Chapter 8:** Royuela-del Val, J., Simmross-Wattenberg, F., and Alberola-López, C. (2017b). Libstable: Fast, Parallel and High-Precision Computation of alpha-Stable Distributions in C, MATLAB and R. *Journal of Statistical Software*. (In press).

**Conference/Workshop papers**

- **Chapter 4:** Royuela-del Val, J., Usman, M., Cordero-Grande, L., Simmross-Wattenberg, F., Martín-Fernández, M., Prieto, C., and Alberola-López, C. (2015). Single breath hold whole heart cine MRI with iterative groupwise cardiac motion compensation and sparse regularization (kt-WiSE). In *Proceedings of the 23rd Annual Meeting of the International Society of Magnetic Resonance in Medicine*, page 572, Toronto, CA.

- **Chapter 5:** Royuela-del Val, J., Usman, M., Cordero-Grande, L., Simmross-Wattenberg, F., Martín-Fernández, M., Prieto, C., and Alberola-López, C. (2016c). Multiresolution Reconstruction of Real-Time MRI with Motion Compensated Compressed Sensing: Application to 2D Free-Breathing Cardiac MRI. In *Proceedings of the 13th IEEE International Symposium on Biomedical Imaging: From Nano to Macro*.

- **Chapter 6:** Royuela-del Val, J., Usman, M., Cordero-Grande, L., Simmross-Wattenberg, F., Martín-Fernández, M., Prieto, C., and Alberola-López, C.

(2016d). Whole-heart single breath-hold cardiac cine: A robust motion-compensated compressed sensing reconstruction method. In *Proceedings of the 19th International Conference on Medical Image Computing & Computer Assisted Intervention. 1st International Workshop on Reconstruction and Analysis of Moving Body Organs (MICCAI/RAMBO 2016)*.

- **Chapter 7:** Royuela-del Val, J., Usman, M., Cordero-Grande, L., Simmross-Wattenberg, F., Martín-Fernández, M., Prieto, C., and Alberola-López, C. (2017c). Cardio-respiratory motion estimation for compresssed sensing reconstruction of free-breathing 2D cine MRI. In *Proceedings of the 25th annual meeting of the International Society of Magnetic Resonance in Medicine*, Honolulu, HW, USA. (Accepted).

### 1.5.2 Additional papers

Additional publications not included in this Thesis are listed:

- Cordero-Grande, L., del Val, J. R., Sanz-Estébanez, S., Martín-Fernández, M., and Alberola-López, C. (2016). Multi-oriented windowed harmonic phase reconstruction for robust cardiac strain imaging. *Medical Image Analysis*, 29:1–11.

- Julián-Moreno, G., López de Vergara, J. E., González, I., de Pedro, L., Royuela-del Val, J., and Simmross-Wattenberg, F. (2016). Fast parallel $\alpha$–stable distribution function evaluation and parameter estimation using OpenCL in GPGPUs. *Statistics and Computing*.

- Sanz-Estébanez, S., Royuela-del Val, J., Sevilla, T., Revilla-Orodea, A., Aja-Fernández, S., and Alberola-López, C. (2016). Harmonic auto – regularization for non rigid groupwise registration in cardiac magnetic resonance imaging. In *Proceedings of the XXXIV Annual Congress of the Spanish Society of Biomedical Engineering (CASEIB)*.

- Royuela-del Val, J., Martín-Fernández, M., Simmross-Wattenberg, F., and Alberola-López, C. (2016b). Cardio-respiratory motion estimation for compressed sensing reconstruction of free-breathing 2d cine mri. In *Proceedings of the International Workshop on Imaging with Modulated/Incomplete Data. Graz University of Technology*, Graz, Austria.

CHAPTER

# TWO

# NON-RIGID GROUPWISE REGISTRATION FOR MOTION ESTIMATION AND COMPENSATION IN COMPRESSED SENSING RECONSTRUCTION OF BREATH-HOLD CARDIAC CINE MRI

**Published as:**

Javier Royuela-del-Val[1], Lucilio Cordero-Grande[1,2], Federico Simmross-Wattenberg[1], Marcos Martín-Fernández[1] and Carlos Alberola-López[1] (2016), Nonrigid Groupwise Registration for Motion Estimation and Compensation in Compressed Sensing Reconstruction of Breath-Hold Cardiac Cine MRI. Magnetic Resonance in Medicine, 75:1525–1536.

[1] Laboratorio de Procesado de Imagen, Universidad de Valladolid, Valladolid, Spain

[2] Division of Imaging Sciences and Biomedical Engineering, Centre for the Developing Brain, King's College London, London, UK

**Abstract**

**Purpose:** Compressed sensing methods with motion estimation and compensation techniques have been proposed for the reconstruction of accelerated dynamic MRI. However, artifacts that naturally arise in compressed sensing reconstruction procedures hinder the estimation of motion from reconstructed images, especially at high acceleration factors. This work introduces a robust groupwise non-rigid motion estimation

technique applied to the compressed sensing reconstruction of dynamic cardiac cine MRI sequences.

**Theory and Methods:** A spatio-temporal regularized, groupwise, non-rigid registration method based on a B-splines deformation model and a least squares metric is used to estimate and to compensate the movement of the heart in breath-hold cine acquisitions and to obtain a quasi-static sequence with highly sparse representation in temporally transformed domains.

**Results:** Short axis in vivo datasets are used for validation, both original multi-coil as well as DICOM data. Fully sampled data were retrospectively undersampled with various acceleration factors and reconstructions were compared with the two well-known methods k-t FOCUSS and MASTeR. The proposed method achieves higher signal to error ratio and structure similarity index for medium to high acceleration factors.

**Conclusions:** Reconstruction methods based on groupwise registration show higher quality reconstructions for cardiac cine images than the pairwise counterparts tested.

**Keywords:** dynamic MRI reconstruction, compressive sensing, groupwise registration

## 2.1 Introduction

Breath–hold (BH) cardiac cine MRI has become the gold standard for myocardial function imaging (Feng et al., 2013). In patients with diminished BH capacity this approach results in substantially compromised image quality (Chandarana et al., 2011). A respiratory-navigated, free-breathing examination can be performed as an alternative that, however, can result in unpredictably long acquisition times. Shortening the needed acquisition time can enable some of these patients to get a regular BH scan and, generally speaking: 1) improves patient comfort and reduces stress, 2) significantly reduces exam duration and the associated economical costs. Therefore, the development of faster acquisition methods is of great importance.

Reduced-data imaging methods take advantage of redundancy in the images to recover the whole image from only a fraction of the k-space data, shortening

acquisition time consequently. In classical approaches, such as k-t BLAST/SENSE (Tsao et al., 2003) and k-t GRAPPA (Huang et al., 2005), data are acquired following a regular pattern and the spatio-temporal correlation is exploited to recover the original image. A detailed review on these classical approaches has been published by Tsao and Kozerke (2012). More recently, compressed sensing (CS) theory (Candès et al., 2006; Donoho, 2006) has been successfully applied to MRI reconstruction (Lustig et al., 2007; Otazo et al., 2010; Usman et al., 2013; Chen et al., 2014; Feng et al., 2013; Lingala et al., 2015; Yoon et al., 2014) showing that when an image has an sparse representation in certain domain it can be recovered from a small number of incoherent measurements.

In cardiac cine imaging intensity variations are mainly due to the movement of cardiac structures. Moving regions of the image lead to abrupt intensity changes through time that reduces the sparsity of the signal in the transformed temporal domain (Irarrazaval et al., 2005; Jung et al., 2009; Jung and Ye, 2010; Asif et al., 2013). As stated by Prieto et al. (2007), if the motion of elements in an image can be described with fewer parameters than the intensity changes derived from that motion, the sparsity is expected to increase by using motion modeling. In Figure 2.1 this approach is illustrated.

When applied to dynamic MRI reconstruction, motion estimation (ME) and motion compensation (MC) techniques lack the true dynamic image to estimate the motion information from. A common approach is to perform the ME step from an initial reconstruction of the images themselves that, however, will be affected by the artifacts introduced by the undersampling pattern that the initial reconstruction could not correct, what hinders the estimation of the true motion information. This effect becomes more relevant as the acceleration factor increases.

In k-t FOCUSS with ME/MC, Jung and Ye (2010) use a high quality reference frame to perform ME by means of a block matching algorithm applied independently to each frame. The reference frame may not be available and the final reconstruction result depends heavily on its quality. In MASTeR, Asif et al. (2013) estimate the motion sequentially between each pair of consecutive frames. In both approaches only two frames of the sequence are available for the ME algorithm at each execution, therefore the ME algorithm cannot benefit from the additional information present in the rest of the frames making it more sensitive to artifacts in the sequence.

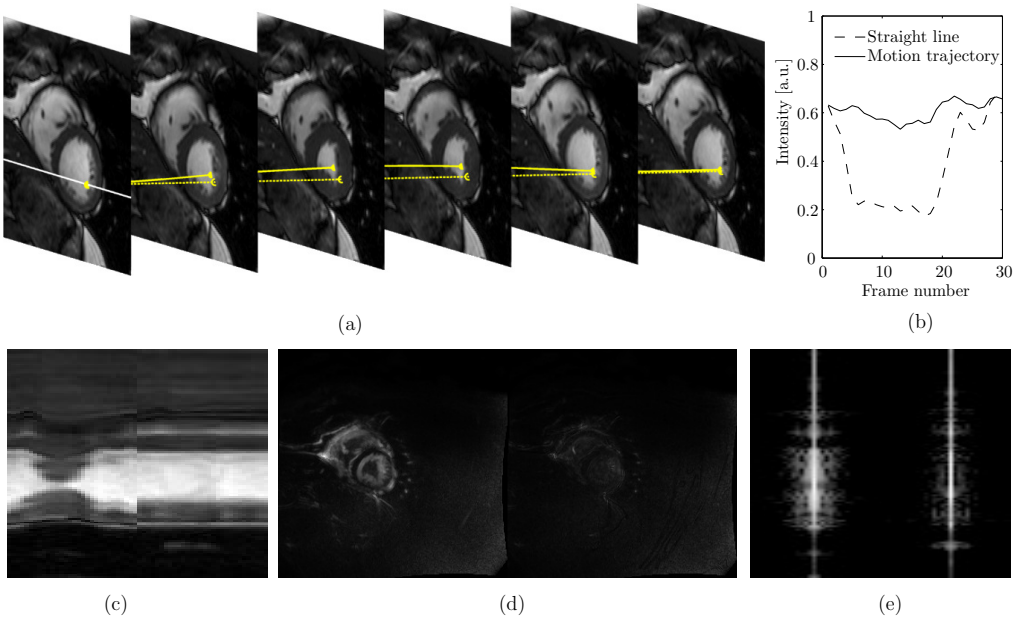


Figure 2.1: (a) Selected frames from a cine MRI sequence with estimated material point trajectory along time (continuous line) vs. fixed spatial position (dashed line). (b) Pixel intensity along time and along estimated motion trajectory. Lower and smoother intensity transitions are present in the second case. (c) Temporal evolution of a single slice in original sequence (left) and after compensate the estimated motion. Temporal total variation (TV) (d) and temporal log-Fourier transform (e) of the original and motion compensated sequences. In (d), a noticeable reduction in the TV values can be observed. In (e), the Fourier coefficients get more concentrated around the DC and low frequency components. The MC procedure contributes to obtain a sparser representation in the $x$-$f$ space.

In this paper, and borrowing some ideas proposed by Cordero-Grande et al. (2013), the shortcomings of ME referred to above have been alleviated by adopting a GW approach in which the whole-sequence is registered at once to compensate for the naturally induced motion of the heart. This results in a pseudo-static sequence which, in combination with a spatio-temporal sparsifying transform, turns out to be highly sparse. We hypothesize that, given the more available information, our ME algorithm will be more robust than pairwise (PW) approaches. We call this method groupwise compressed sensing (GW-CS). Figure 1c and Supporting Video 1 illustrate the application of the GW ME/MC method. Departing from an initial reconstruction, refined reconstructed images and estimated motion information are obtained iteratively. This scheme can be easily adapted to other imaging modalities by selecting proper ME metrics and sparsifying transforms.

## 2.2 Theory

### CS reconstruction of undersampled dynamic MRI with ME

The CS reconstruction of undersampled MRI data is generally formulated as a constrained optimization problem given by

$$\underset{\mathbf{m}}{\text{minimize}} \|\mathbf{\Phi m}\|_{\ell 1} \quad s.t. \quad \|\mathbf{y}-\mathbf{Em}\|_{\ell 2}^2 < \epsilon \tag{2.1}$$

where $\mathbf{\Phi}$ is the sparsifying transform, $\mathbf{m}$ and $\mathbf{y}$ are the dynamic MRI image to be reconstructed and the undersampled k-t data, respectively, defined as single column vectors. The encoding operator $\mathbf{E}$ performs a frame-by-frame undersampled spatial Fourier transform. In multicoil acquisitions, $\mathbf{E}$ includes the multiplication by coil sensitivities as described by Pruessmann et al. (1999). The threshold $\epsilon$ denotes the noise level in the acquisition. The constrained optimization problem in Eq. (2.1) can be converted into an unconstrained problem using a Lagrangian multiplier as follows:

$$\underset{\mathbf{m}}{\text{minimize}} \frac{1}{2} \parallel \mathbf{y}-\mathbf{Em} \parallel_{\ell_2}^2 + \lambda \parallel \mathbf{\Phi m} \parallel_{\ell_1} \tag{2.2}$$

where the parameter $\lambda$ establishes a trade off between data consistency and the sparsity of the solution. In CS with ME/MC, the operator $\mathbf{\Phi}$ is modified to account for the specific motion information that is present in the dynamic image at hand. In k-t FOCUSS with ME/MC (Jung et al., 2009) the unknown image

$\mathbf{m}$ is decomposed into a predicted, $\mathbf{m}_{\text{pred}}$, and a residual image, $\Delta\mathbf{m}$, which is assumed to be sparse:

$$\mathbf{m} = \mathbf{m}_{\text{pred}} + \Delta\mathbf{m} \tag{2.3}$$

To further increase the sparsity of the residual signal, the FT is applied along the temporal dimension of $\Delta\mathbf{m}$, denoted by the $\mathbf{F}_{\text{t}}$ operator. The optimization problem in Eq. (2.2) becomes

$$\underset{\mathbf{m}}{\text{minimize}}\ \frac{1}{2} \parallel \mathbf{y} - \mathbf{E}\mathbf{m} \parallel_{\ell_2}^2 + \lambda \|\mathbf{F}_{\text{t}}\Delta\mathbf{m}\|_{\ell_1} \tag{2.4}$$

The predicted signal $\mathbf{m}_{\text{pred}}$ is obtained by applying a block matching algorithm between each frame of $\mathbf{m}$ and a reference frame $\mathbf{m}_{\text{ref}}$. Since neither $\mathbf{m}_{\text{ref}}$ nor the true dynamic image are available for ME, a previous reconstruction step is performed with the original k-t FOCUSS algorithm without ME/MC proposed by Jung et al. (2007).

On the other side, the MASTeR procedure does not rely on a reference frame, but motion is estimated sequentially between each pair of consecutive frames to define a set of operators that predict each frame $\mathbf{m}_i$ out of its leading and trailing frames:

$$\begin{aligned} \mathbf{m}_i &= \mathcal{F}_{i-1}\mathbf{m}_{i-1} + \mathbf{f}_i \\ \mathbf{m}_i &= \mathcal{B}_{i+1}\mathbf{m}_{i+1} + \mathbf{b}_i \end{aligned} \tag{2.5}$$

where $\mathcal{F}_{i-1}$ and $\mathcal{B}_{i+1}$ denote the forward and backward MC operators. Residuals $\mathbf{f}_i$ and $\mathbf{b}_i$ are assumed to be sparse and are used as sparsity term in Eq. (2.2):

$$\underset{\mathbf{m}}{\text{minimize}}\ \frac{1}{2} \parallel \mathbf{y} - \mathbf{E}\mathbf{m} \parallel_{\ell_2}^2 + \parallel \mathcal{M}\mathbf{m} \parallel_{\ell_1} \tag{2.6}$$

where $\mathcal{M}\mathbf{m} = [\, \alpha\, \mathbf{f}_i^{\text{T}} \mid \beta\, \mathbf{b}_i^{\text{T}} \,]^{\text{T}}$ is the weighted column-wise concatenation of both backward and forward residual terms given by Eq. (2.5). For the initialization, Eq. (2.2) is solved using 2-D dual tree (DT) complex wavelet transform (CWT) (Selesnick et al., 2005) as spatial sparsifying transform. A method also based on CWT is used for estimating inter-frame motion (Magarey and Kingsbury, 1998).

As explained in the introduction, ME methods described above suffer some shortcomings derived from the limited information available to the pair-wise ME algorithms. In GW-CS, we propose to jointly estimate and compensate the motion in the whole dynamic image domain. Under this approach, the optimization problem in Eq. (2.2) becomes

$$\underset{\mathbf{m}}{\text{minimize}}\ \frac{1}{2} \parallel \mathbf{y} - \mathbf{E}\mathbf{m} \parallel_{\ell_2}^2 + \lambda \parallel \mathbf{\Phi}\mathcal{T}_{\Theta}\mathbf{m} \parallel_{\ell_1} . \tag{2.7}$$

where $\mathbf{\Phi}$ is a freely chosen spatio-temporal sparsifying transform and $\mathcal{T}_\Theta$ is a groupwise MC operator that will be introduced below. We should point out that in the MASTeR case the sparse representation based on the registration residuals is determined by the ME scheme itself, for which an additional transformation may not be clearly beneficial in terms of increasing sparsity. The proposed ME algorithm is detailed in the next section.

### Temporal groupwise registration for ME/MC

To introduce the registration method it is convenient to redefine the dynamic MRI sequence $\mathbf{m}$ as a set of spatially continuous images:

$$m = \{m_1(\mathbf{x}), m_2(\mathbf{x}), \ldots, m_N(\mathbf{x})\}$$

with $1 \leq n \leq N$ a temporal index and $m_n(\mathbf{x})$ defined over the space $\mathbf{x} \in \mathcal{X} \subset \mathbb{E}^2$. The registration procedure consists in finding a set of spatial transformations $T = \{T_n : \mathbf{x}'_n = T_n(\mathbf{x}) \in \mathcal{X}\}$ such that the cost function given by

$$H(T; m) = \int_{\mathcal{X}} V(m_1(T_1(\mathbf{x})), \ldots, m_N(T_N(\mathbf{x})))\mathrm{d}\mathbf{x} \tag{2.8}$$

is minimized (Cordero-Grande et al., 2013). The solution is constrained to those sets of transformations with the average deformation of each position equal to the identity transformation (Bhatia et al., 2004):

$$\frac{1}{N}\sum_{n=1}^{N} T_n(\mathbf{x}) = \mathbf{x} \tag{2.9}$$

In Eq. (2.8), the integrand $V(m_1(T_1(\mathbf{x})), \ldots, m_N(T_N(\mathbf{x}))) = V(\mathbf{x})$ is the similarity metric used to measure the point by point similarity between the set of images. In cardiac cine MRI, the intensity change of the image along time is mainly due to the movement of the heart, so a least squares metric based on the variance of the intensity (VI) along time may suffice (Metz et al., 2011):

$$V(\mathbf{x}) = \frac{1}{N}\sum_{n=1}^{N}\left(m_n(T_n(\mathbf{x})) - \frac{1}{N}\sum_{k=1}^{N} m_k(T_k(\mathbf{x}))\right)^2. \tag{2.10}$$

There is also a need for an adequate deformation model. The proposed algorithm employs a 2D free form deformation (FFD) model based on B-splines (Rueckert et al., 1999), which has been widely used in practice. The FFDs

are based on a parametric model that deforms an object by manipulating an underlying mesh of $M$ control points $\Theta = \{\theta_{k,n}\}$, with $1 \leq k \leq M, 1 \leq n \leq N$, uniformly spaced in $\mathcal{X}$. Then the set of deformations $T$ is parametrized by $\Theta$, a fact that we denote by $T = T_\Theta$.

To constrain the estimated deformation to be smooth, in concordance with the expected deformation of anatomical structures (Rueckert et al., 1999), a penalty regularization term is introduced in Eq. (2.8) given by:

$$C(T_\Theta) = \frac{1}{|\mathcal{X}|N} \sum_{n=1}^{N} \int_{\mathcal{X}} \alpha \left( \left| \frac{\partial^2 T_n(\mathbf{x})}{\partial x^2} \right|^2 + \left| \frac{\partial^2 T_n(\mathbf{x})}{\partial y^2} \right|^2 + 2 \left| \frac{\partial^2 T_n(\mathbf{x})}{\partial x \partial y} \right|^2 \right) + \beta \left| \frac{\partial^2 T_n(\mathbf{x})}{\partial n^2} \right|^2 \mathrm{d}\mathbf{x} \tag{2.11}$$

where $(x, y)^{\mathrm{T}} = \mathbf{x}$. We add a temporal regularization term in order to favor smoothness in the temporal trajectory based on temporal derivatives approximated by finite differences. Given the quasi-periodic motion of the heart the last frame in the sequence is considered to be followed by the first one. $\alpha$ and $\beta$ parameters used to weight the spatial and temporal regularization terms, respectively. The resulting regularized non-rigid GW registration is then formulated as

$$\underset{\Theta}{\text{minimize}}\ H(T_\Theta; m) + C(T_\Theta) \tag{2.12}$$

and the groupwise MC operator $\mathcal{T}_\Theta$ in Eq. (2.7) is defined as the discretized version of $T_\Theta$.

### Reconstruction algorithm

Since at the very beginning of the algorithm we do not have any data from which motion information can be estimated, we have resorted to the common approach (Prieto et al., 2007; Jung et al., 2009; Asif et al., 2013) of making use of a regular CS reconstruction prior step; then an iterative procedure consisting in a ME/MC step followed by a MC-CS reconstruction step, is adopted. In our implementation a predefined number of iterations has been set; it is very simple to use some alternative convergence criterion instead. A pseudocode description of the algorithm follows:

Groupwise registration based CS reconstruction of Undersampled Dynamic MRI.

**input:**

$\mathbf{y}$: undersampled k-t data

$\mathbf{E}$: encoding operator

$\mathbf{\Phi}$: sparsifying transform

$\lambda, \lambda_{s/t}$: sparsity regularization parameters

$\alpha, \beta$: ME/MC regularization parameters

**initialization:**

$k \leftarrow 0$

% Solve regular CS reconstruction problem in Eq. (2.2):

$\mathbf{m}_0 \leftarrow \arg\min_{\mathbf{m}} \|\mathbf{y} - \mathbf{E}\mathbf{m}\|_{\ell_2}^2 + \lambda\|\mathbf{\Phi}\mathbf{m}\|_{\ell_1}$

**while** $k <$ max. number of iterations **do**

% Temporal registration: Solve Eq. (2.12)

$\Theta_{k+1} \leftarrow \arg\min_{\Theta} H(T_\Theta; \mathbf{m}_k) + C(T_\Theta)$

% MC-CS reconstruction: Solve Eq. (2.15) (as opposed to (2.7), see Implementation section) with estimated motion parameters.

$$\underset{\mathbf{m}}{\text{minimize}} \frac{1}{2} \| \mathbf{y} - \mathbf{E}\mathbf{m} \|_{\ell_2}^2 + \lambda \Big\| \Big[ (\mathbf{\Phi}_{\mathrm{t}} \mathcal{T}_\Theta)^{\mathrm{T}} \mid \lambda_{\mathrm{s/t}} \mathbf{\Phi}_{\mathrm{s}}^{\mathrm{T}} \Big]^{\mathrm{T}} \mathbf{m} \Big\|_{\ell_1} .$$

$k \leftarrow k + 1$

**end**

**output:** $\mathbf{m}_k$

## 2.3 Methods

In this section the procedures followed to implement and to validate the proposed algorithm are described. First, our hypothesis on the superiority of the GW approach *vs.* the PW counterpart is tested. Details of the method implementation and parameter selection are also provided. The quality of the reconstructions have been tested both with quantitative metrics and the subjective judgment of expert clinicians.

### Groupwise and pairwise registration comparison

In order to validate the hypothesis that the proposed GW registration algorithm performs better than an equivalent PW approach, the following experiment was carried out:

1. A sum of squared differences registration metric equivalent to the PW version of the metric in Eq. (2.10) was defined as

$$V(\mathbf{x}) = \frac{1}{N}\sum_{n=1}^{N}\left(m_n(T_n(\mathbf{x})) - m_{ref}(\mathbf{x})\right)^2. \tag{2.13}$$

   where $m_{ref}$ denotes the frame selected as a reference. We choose a diastolic frame, where lower cardiac motion is present.

2. The ME algorithm was applied to an initial regular CS reconstruction of a sequence from a healthy volunteer, for undersampling factors of the k-space data ($r$) ranging from one (no undersampling) to 16. The deformation fields obtained for the GW and PW metrics are denoted as $T^r_{GW}(\mathbf{x})$ and $T^r_{PW}(\mathbf{x})$, respectively. We define the registration error (RE) committed due to the presence of undersampling artifacts as —for the GW metric—:

$$RE_{GW}(r) = \int_{\mathcal{X}} \|T^1_{GW}(\mathbf{x}) - T^r_{GW}(\mathbf{x})\|^2 \mathrm{d}\mathbf{x}. \tag{2.14}$$

   The definition for the PW method is analogous. The behavior of $RE(r)$ denotes how fast the registration degrades due to the increasing presence of undersampling artifacts.

### Algorithm implementation

The GW-CS reconstruction was performed in MATLAB (MathWorks, Natick, MA). The optimization problems in Eqs. (2.2) and (2.7) related to the reconstruction steps have been solved using the Nesterov's algorithm (NESTA) (Becker et al., 2011). For the initialization of the algorithm, spatial DT-CWT of each frame was used as sparsifying transform $\mathbf{\Phi}$, in order to get the same initial reconstruction than MASTeR. A nonlinear conjugate gradient algorithm with backtracking line search (Nocedal and Wright, 1999) has been used to solve the registration problem in Eq. (2.12). Additional fixed control points were placed

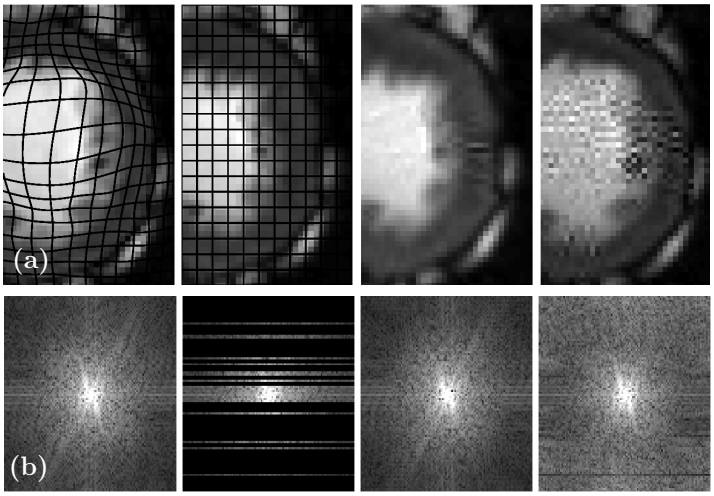


Figure 2.2: Effect of the interpolation in the reconstructed signals. (a) from left to right: detail of the original sequence to be reconstructed with estimated motion deformation superposed for better visualization, same region after MC, reconstructed sequence with spatial sparsity constrain applied to the motion compensated sequence and reconstructed image after MC. In the last case, the high frequency artifact present in the reconstructed signal has been removed by the deformation/interpolation operator. (b) from left to right: original fully sampled k-space data, undersampled data, k-space data of the reconstructed sequence and k-space data of the MC reconstructed sequence.

outside the image domain in order to guarantee that the spatial transformation is properly defined inside the domain.

In the following reconstruction steps, the sparsifying transform $\mathbf{\Phi}$ in Eq. (2.7) may comprise both spatial and temporal dimensions transforms. However, we should make some considerations: given the discrete nature of the reconstructed images, the application of the MC operator involves an interpolation step that implies unavoidable errors. As we could verify, the interpolation process may distort the reconstruction result, as illustrated in Figure 2.2. Since the MC operator introduces a spatial low pass filtering as a side effect, high spatial frequency components in the reconstructed image are not present in the image used in the $\ell_1$ regularization term in Eq. (2.7). Furthermore, since only only a small fraction of the high frequency coefficients is acquired, data mismatch in high frequency components is not properly penalized by the data fidelity term.

To overcome this limitation, we split the spatio-temporal sparsifying transform in Eq. (2.7) into a temporal transform applied to the motion compensated sequence and a spatial transform applied to the original sequence without MC. That is, we actually solve the optimization problem given by

$$\underset{\mathbf{m}}{\text{minimize}}\ \frac{1}{2}\parallel \mathbf{y}-\mathbf{E}\mathbf{m}\parallel_{\ell_2}^2 +\lambda\Big\| \Big[\ (\mathbf{\Phi}_{\mathrm{t}}\mathcal{T}_{\Theta})^{\mathrm{T}} \mid \lambda_{\mathrm{s/t}}\mathbf{\Phi}_{\mathrm{s}}^{\mathrm{T}}\ \Big]^{\mathrm{T}}\mathbf{m}\Big\|_{\ell_1}\ . \tag{2.15}$$

where $\lambda_{\mathrm{s/t}}$ weights the spatial sparsity vs. temporal sparsity.

Undersampled data was also reconstructed using k-t FOCUSS with ME/MC and MASTeR. To this end, the code from the authors of (Asif et al., 2013) with minor adaptations was used. This code is available at

http://users.ece.gatech.edu/∼sasif/dynamicMRI.

For the k-t FOCUSS reconstruction, a set of diastole cardiac phase frames from each dataset was manually selected and its temporal average used as a reference frame to obtain the predicted signal $\mathbf{m}_{\mathrm{pred}}$ in Eq. (2.3). The number of ME-reconstruction iterations of MASTeR and GW-CS was set to four.

## Data acquisition

Three different datasets have been employed, two with healthy volunteers and one with patients diagnosed with hypertrophic cardiomyopathy (HCM). In all the cases a regular, fully sampled, multislice 2D BH cardiac cine MRI study was acquired. The fully sampled data was retrospectively undersampled using a Gaussian variable-density random undersampling pattern along the phase encoding direction. Eight central lines of the k-space were always selected and sensitivity maps were obtained from separate scans. All the scans were performed in accordance with the Research Ethics Board of our institutions and each subject provided informed consent. Each of the datasets are described at continuation.

### Multi-Coil data of healthy volunteers

One healthy volunteer was scanned on a 1.5T Philips scanner (Philips Healthcare, The Netherlands) with a 32-element cardiac coil employing a bSSFP sequence. Relevant scan parameters include: TR/TE/flip angle = 2.8ms/1.39ms/60°, field of view (FOV) = 320 × 320mm$^2$, spatial resolution = 2 × 2 mm$^2$, slice thickness = 8mm with no gap between slices. 16 cardiac phases were reconstructed.

A short axis MRI scan made available by the authors of (Asif et al., 2013) was also used for reconstruction of multi-coil data. The dataset was acquired using

a General Electric 1.5T TwinSpeed scanner with a 5-element cardiac coil and a FIESTA/FastCARD cine steady-state free precession sequence, with following parameters: TE/TR/flip angle = 2.0ms/4.1ms/45°, FOV = 350 × 350 mm$^2$, 224 × 256 matrix reconstruction and 16 temporal frames.

**Single-Coil data of healthy volunteers and HCM patients**

Three healthy volunteers were scanned on a 3T Philips scanner with a 32-element cardiac coil. Other relevant scan parameters include: b-SSFP sequence, TR/TE/flip angle = 3.3ms/1.57ms/45°, FOV = 320×320mm$^2$, 30 cardiac phases, and slice thickness = 8 mm. Three patients diagnosed with HCM were scanned with a 16-element antenna and the same parameters, excluding: TR/TE/flip angle = 6ms/3ms/25° and FOV = 425 × 425 mm$^2$. Since no raw data were available, reconstructed DICOM sequences were converted back into k-t space and considered as single coil acquisitions.

### Quantitative metrics comparison

Two quantitative error metrics were used for comparison of the reconstructions. Firstly, the signal to error ratio (SER), defined as

$$\mathrm{SER(dB)} = 20\log_{10}\frac{\|\mathbf{m}\|_{\ell_2}}{\|\mathbf{m}-\hat{\mathbf{m}}\|_{\ell_2}},$$

where $\mathbf{m}$ denotes the fully sampled image and $\hat{\mathbf{m}}$ the image reconstructed from the undersampled data. Second, the structural similarity (SSIM) index introduced by (Wang et al., 2004) was also used as a quantitative metric that better represents image quality.

### Subjective image quality review from clinicians

For a set of three healthy volunteers and three patients affected by HCM the reconstructions obtained with k-t FOCUSS, MASTeR and the proposed method for acceleration factors 4, 6 and 8 were blindly reviewed and rated by three experts*. For each dataset and acceleration factor, the reconstructions obtained with each method were simultaneously presented on the screen sorted randomly to the experts, who were asked to rate them attending to their general quality. The results were collected via a web form. Each expert rated two controls and two cases, so each individual has been rated by two experts.

*Namely, the two cardiologists Dr. A. Revilla, and Dr. T. Sevilla and the radiologist Dr. J. Calabia, all of them from the Hospital Clínico Universitario of Valladolid, Spain

### Parameter selection

To select those registration parameters $\alpha$ and $\beta$ that make the registration algorithm most robust against the undersampling artifacts without compromising the estimation of the true cardiac motion, the ME algorithm was applied to an initial CS reconstruction of a healthy volunteer sequence undersampled by a factor of 6. $\alpha$ and $\beta$ were chosen to minimize the residual motion —measured as the temporal TV of the resulting sequence— when the motion fields thus obtained were applied to the original, fully sampled image. The optimal values of $\alpha$ and $\beta$ did not show significant variation for other acceleration factors considered. Moreover, the final reconstruction results have shown to be robust to the choice of $\alpha$ and $\beta$ in a wide range of values for all the datasets used since the heart dimensions and the field of views do not differ considerably in all the datasets used.

The reconstruction parameters $\lambda$ and $\lambda_{s/t}$ and their equivalent counterparts in the compared methods (see the works from Jung et al. (2007) and Asif et al. (2013)) were fitted to get the highest SER in the reconstruction of the 1.5T (5 coils) dataset, one of the 3T datasets (DICOM data) and the 32-coil dataset. An example of the sensitivity of both SER and SSIM (see Results section) is shown in the Supporting Figure 1 for the latter dataset. Notice that the axis are in logarithmic scale. These parameters have been used for the experiments described below with the only exception of the subjective judgment on the three HCM patients; in that experiment, since the acquisition signal to noise ratio was considerably smaller —a different cardiac antenna was used—, the SER did not turn out to be a satisfactory metric; on these data, the parameters for the subjective judgment experiment have been set, for the three methods, by maximizing the visual judgment of a different observer than the experts on a single patient.

Final reconstructions were obtained for an acceleration factor of 4 with three different sparse transforms applied in the initialization of the algorithm, namely, temporal FFT, temporal TV and spatial DT-CWT. Results are fairly similar for the three reconstruction procedures since no structural differences are appraised; some subtle high frequency artifacts are present with TV and DT-CWT, but all of them fall outside the cardiac area. Since we mean to compare our algorithm with MASTeR, we have chosen DT-CWT for initialization.

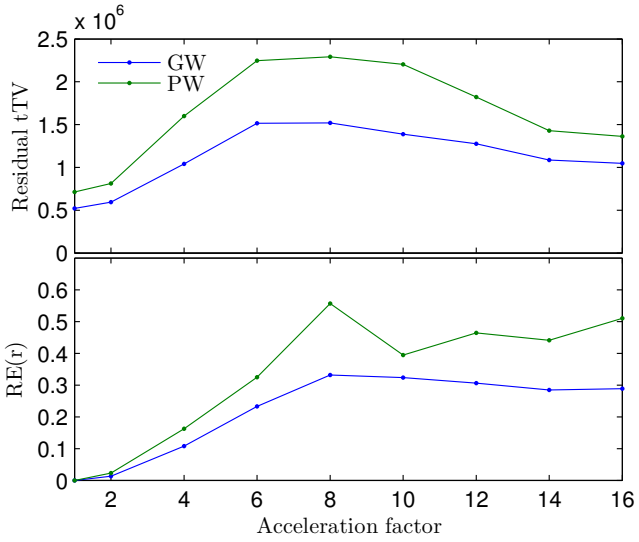


Figure 2.3: (top) Residual temporal Total Variation of the image after registration and (bottom) registration error (see Eq. 2.14) both for GW and PW approaches as a function of the acceleration factor.

## 2.4 Results

### Groupwise and pairwise methods comparison

Figure 2.3 shows on top the RE values defined for the GW case in Equation 2.14 for different values of the acceleration factor. We also show the corresponding RE values for the PW case. The figure on the bottom shows the total variation of the residual image obtained after registration. Both cases (GW and PW) are shown.

Figure 2.4 illustrates the effect of a corrupted ME in a MASTeR reconstruction of a retrospectively 10-fold undersampled short axis cardiac cine sequence. As remarked in Figure 2.4b, in the final reconstruction false motion is introduced in the original sequence. In Figure 2.4c temporal evolution of a single pixel is plotted. The reconstructed pixel intensity fluctuates along time, an effect that is perceived by a human observer as a spatial vibration when observing the dynamic sequence. The temporal TV values in Figure 2.4d illustrates the false motion introduced (in Supporting Video 2 the effect is clearly appreciable). For comparison, in the sequence reconstructed with GW-CS with spatial TV sparsification the effect is not present.

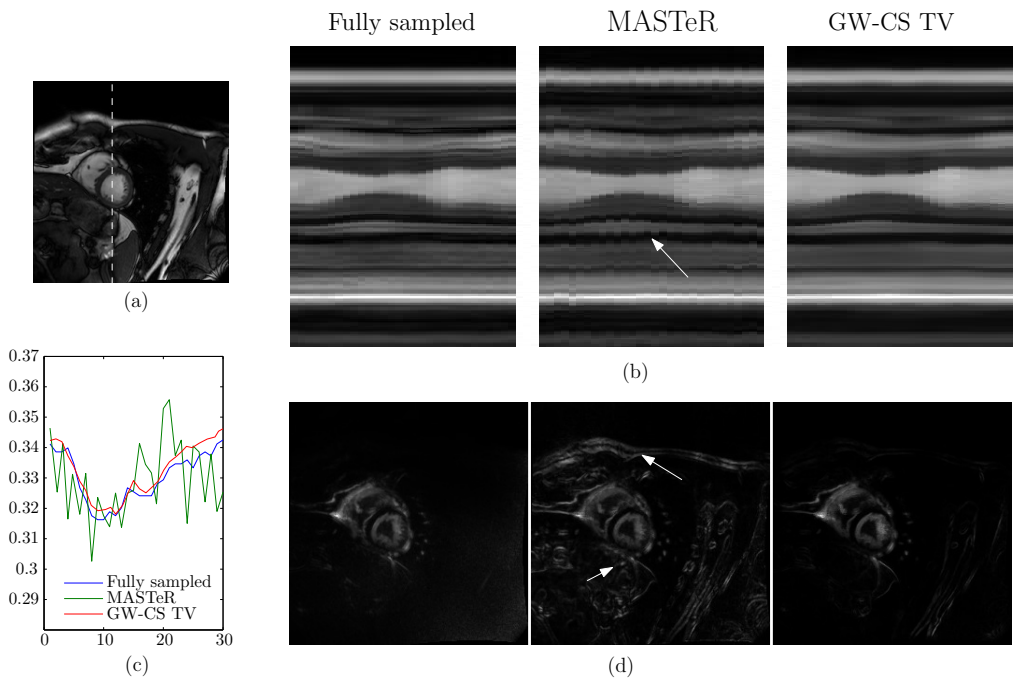


Figure 2.4: Effect of the corrupted ME on a short axis 10-fold undersampled cardiac cine sequence. (a) First frame of the original sequence. (b) Temporal evolution of the intensity profile at the location indicated in (a) by the dashed line. (c) Plot of intensity value along time of the pixel indicated by the arrow in (b), from the fully sampled and reconstructed sequences. (d) Temporal TV of original and final reconstructions.

Figure 2.5 and Supporting Video 3 show the reconstruction results of k-t FOCUSS, MASTeR, and the proposed GW-CS with two spatial sparsifying transforms, TV and CWT, at a high acceleration factor of 12, for the 1.5T dataset. Supporting Video 4 shows the same results for one of the acquired 3T short axis datasets. Results indicate that GW-CS with TV or CWT provides lower error than the rest of the methods. The temporal evolution of a slice is also represented. In Figure 2.6 the proposed algorithm is applied to the dataset from a patient with abnormal cardiac motion. A similar performance of the algorithm can be observed as the temporal behavior of the cardiac structures is preserved; this is illustrated in the last row of the figure for a vertical line taken at the center of the image, and can be more clearly appreciated in the Supporting Video 5.

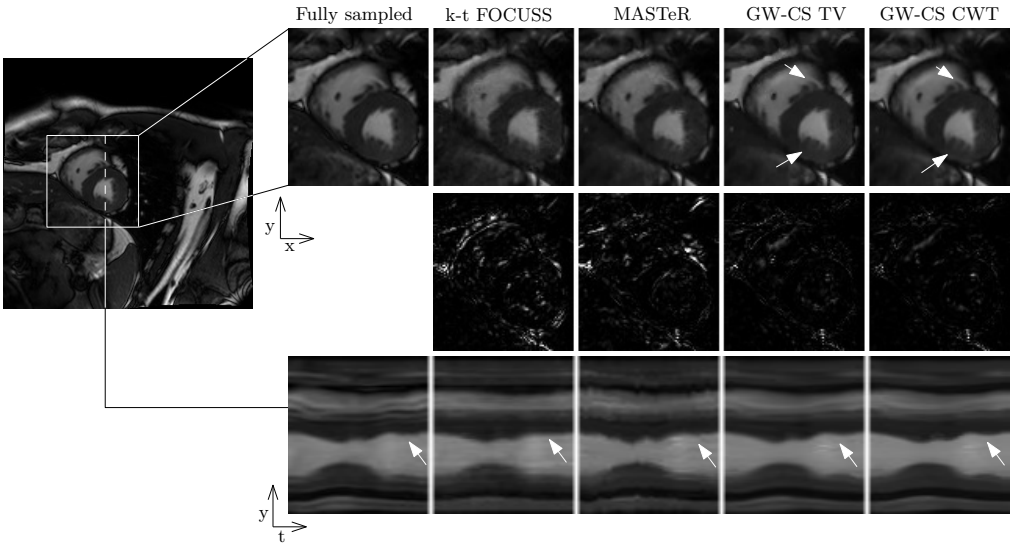


Figure 2.5: Short axis CINE reconstructions with the fully sampled data and k-t FOCUSS, MASTeR and the proposed GW-CS with TV and CWT as spatial sparsifying transforms with retrospective 12-fold undersampling. Single frame (top) and temporal evolution at the location indicated by dashed line (bottom). Middle row shows the absolute error of each image. Arrows in the bottom row indicate regions where fine motion detail has been lost in k-t FOCUSS.

### Quantitative metrics results

In order to evaluate the performance of the different methods along the cardiac cycle, Figure 2.7 shows quantitative quality measures calculated for each reconstructed frame of the same dataset as before in terms of the SER and the SSIM introduced in the previous section, where the fully sampled image is used as reference. In Figure 2.8 the performance of the compared methods for different acceleration factors is analyzed. SER and SSIM index are calculated over a ROI around the heart and plotted vs. the acceleration factor. Figure 2.9 shows the reconstruction of a SA slice from the 32-multicoil 1.5T equipment in the different time instants of the cardiac cycle; the figure also shows plots of the resulting SER and SSIM. In the Supporting Video 6, results for acceleration factors of 1, 2, 4, 8, 12 are available.

### Subjective qualification results

The reviews reported by the clinicians are summarized in table 2.1. The values in the table indicate the number of times the reconstruction obtained with each method was selected as the best one for each acceleration factor.

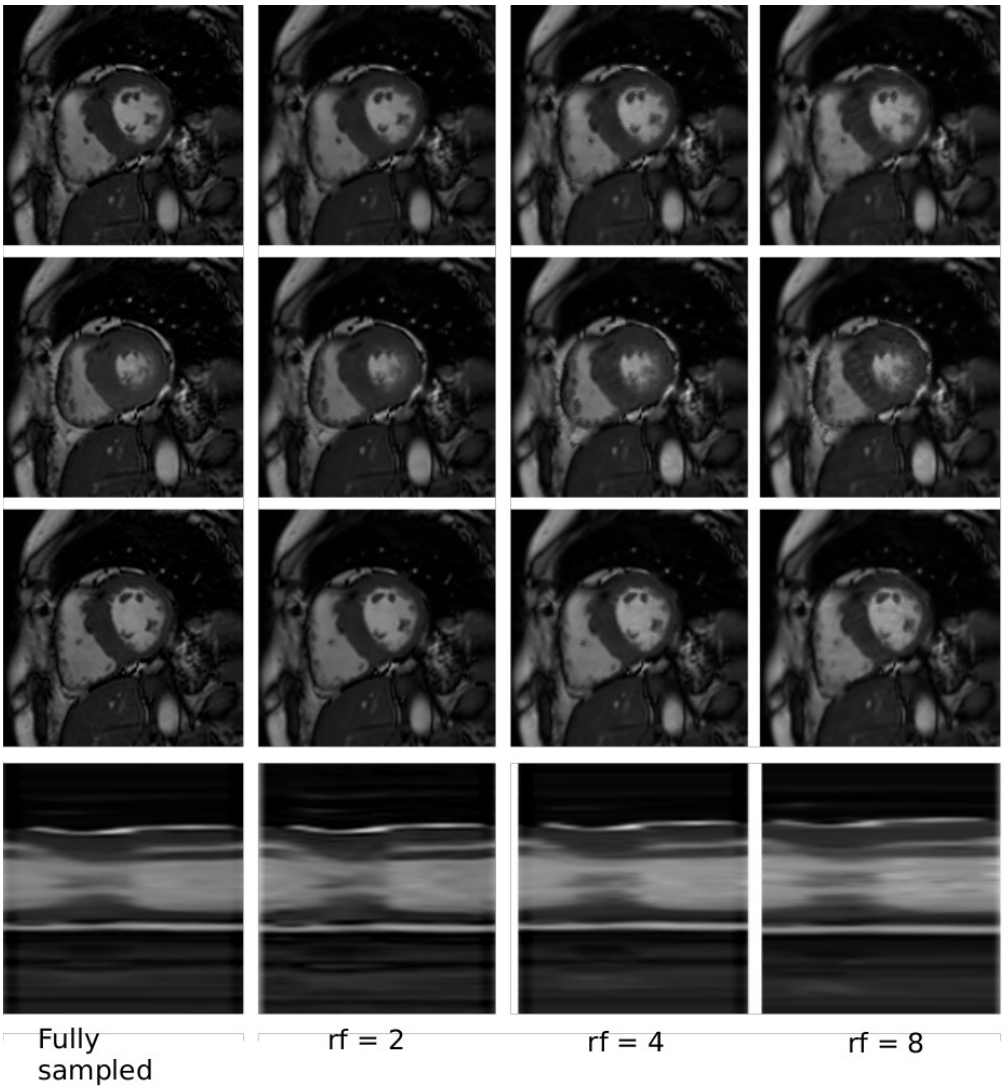


Figure 2.6: Reconstructions of the data from a patient with a diagnosed HCM for different values of the subsampling factor. As it can be observed, the most relevant information, is preserved in the final sequence. The last row in the figure represents the intensity profile of a vertical line taken at the center of the image. The intensity variation highlights that motion is preserved.

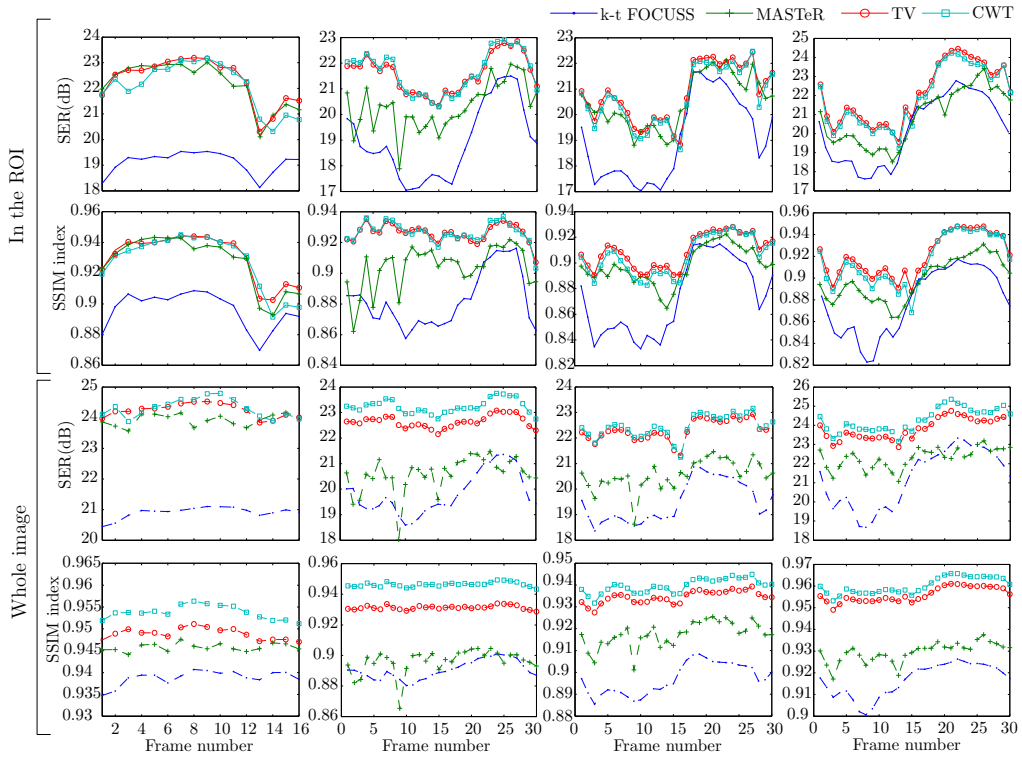


Figure 2.7: Quantitative quality measures for each frame on a 12-fold accelerated reconstruction of each dataset used. SER and SSIM index calculated over a ROI containing the heart and over the whole image. First column corresponds to the 1.5T data and the remaining three columns to the 3T data.

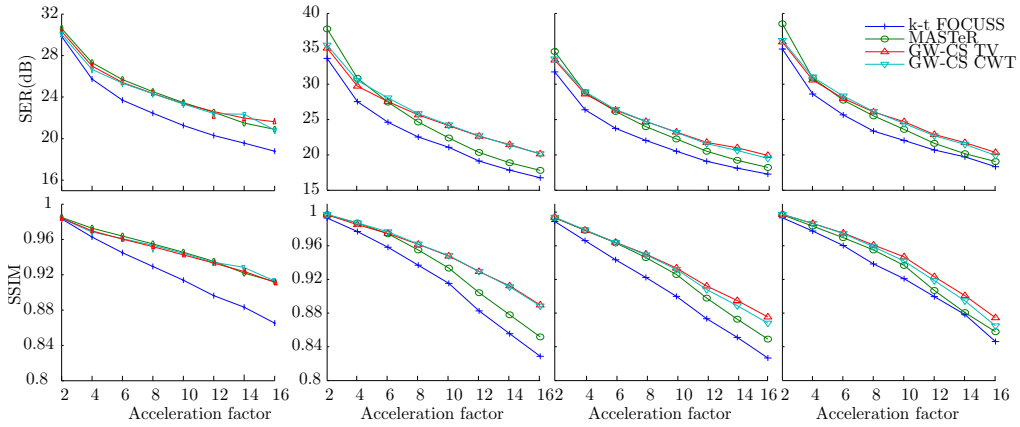


Figure 2.8: SER (top row) and SSIM index (bottom row) calculated over a ROI around the heart for the four reconstructed sequences. First column corresponds to 1.5T data and the remaining three columns to the 3T data.

## 2.5 Discussion

As illustrated in Figures 2.4 and 2.5, GW-CS gets better results than k-t FOCUSS or MASTeR. Less noisy images and smoother interior cavities are recovered while preserving sharp edges at the myocardium wall and small structures. GW-CS with CWT spatial sparsification preserves fine texture details in the image better than TV. Most significant differences can be appreciated in the temporal evolution of a single slice for each reconstruction. With k-t FOCUSS, fine motion details are lost, as can be observed in the interior wall of the myocardium at mid-diastole phase, indicated by arrows in the figure. With MASTeR, the temporal evolution gets noticeably corrupted by an erratic motion that can be most clearly observed in the right ventricle wall. The erratic motion becomes evident when observing the dynamic reconstructions as a video sequence (see Supporting Video 2). A key aspect of cardiac cine MRI for clinical application is the information it provides about myocardium dynamics, so images corrupted by erratic motion may be an issue. This statement seems to be further supported by the subjective judgments of the experts shown in Table 2.1. When applied to cases of abnormal cardiac motion —an HCM patient— the algorithm has shown to perform in a similar way than in the healthy volunteers case (see Figure 2.6).

From the quantitative evaluation plotted in Figure 2.7, we can determine that GW-CS obtains better scores than k-t FOCUSS or MASTeR along the vast majority of cycles in the cardiac cycle, both in phases with faster motion of

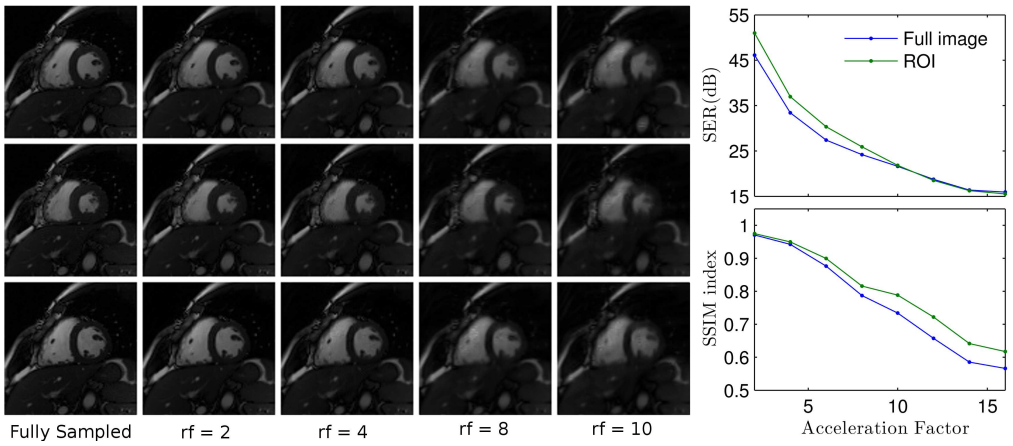


Figure 2.9: (left) Reconstruction of 32-coil acquisitions for different values of the acceleration factor; three instants of the cardiac cycle are shown from top to bottom; (right) SER and SSIM (in the whole image —blue— and within a ROI around the myocardium —green— as function of the acceleration factor for the images shown.

the heart (systole) as well as in slower phases. SER differences in the ROI are within the range of 1–2 dB. During the diastole phase, k-t FOCUS results get close to MASTeR and GW-CS. These are the frames used as reference for the k-t FOCUSS ME step, with small heart motion. Results over the whole image show wider differences, of about 3dB, between GW-CS with CWT and MASTeR. In this case, the difference may be due to the erratic motion introduced by the MASTeR ME method. Results over the whole image also indicate that GW-CS with CWT spatial transform gets better results than spatial TV in the static areas outside the ROI.

Results obtained by GW-CS with CWT or TV for the reconstruction of the 1.5T dataset, illustrated in Figure 2.8, are very close to those obtained by MASTeR. Indeed, for low acceleration factors our method gets slightly worse quantitative metrics than MASTeR. However, in the 3T data experiments, GW-CS outperforms the others for acceleration factors equal or higher than 6. The difference in the results can be explained by two aspects: firstly, the fully sampled 1.5T dataset has an appreciable noise level; during the CS reconstructions part of the noise is washed out by our spatio-temporal sparsity terms. In these situation, the noise removal effect degrades the calculated SER value. 3T data have higher apparent SNR, so this effect is not so relevant. Secondly, the 1.5T data consists of 16 reconstructed cardiac phases, vs. the 30 available in the 3T data. Therefore, much more information is available to the GW-ME method

Table 2.1: Clinical experts qualification results. The values indicate the number of times that each reconstruction was in first place in the reported qualifications

| | Accel. factor | GW-CS | MASTeR | k-t FOCUSS |
|---|---|---|---|---|
| Healthy volunteers | 4 | 4 | 1 | 1 |
| | 6 | 5 | 0 | 1 |
| | 8 | 6 | 0 | 0 |
| HCM patients | 4 | 4 | 1 | 1 |
| | 6 | 5 | 0 | 1 |
| | 8 | 4 | 0 | 2 |

than in the 1.5T dataset. The MASTeR ME method cannot take advantage of the more information available since motion is only estimated between pairs of adjacent frames. Finally, for 32 coil data (recall Figure 2.9) if the plots in this figure are compared with those in Figure 2.8 one can appraise a similar behavior. Therefore, conclusions from 32-elements seem parallel to those previously described.

All in all, in these reconstructions still some high frequency artifacts are appraised, which constitutes a current limitation of our method. Nevertheless, the reviews reported by the clinicians (Table 2.1) indicate that the proposed method outperforms the other other two in terms of subjective perception as well; these differences, in addition, seem to have an increasing trend with the acceleration factor in accordance with the quantitative results obtained in the previous comparison.

In the experimental section we have pursued to compare the performance of the different ME/MC procedures; consequently, all experimental conditions have remained the same, i.e., same undersampling patterns, initialization reconstructions, optimization method and sparsifying transforms have been used. Therefore, we understand that the main source of improvement in our results are due to the superior ME/MC scheme. The B-spline deformation model used is able to accurately describe the motion of the heart and enables us to easily introduce the regularization term in Eq. (2.11) that makes it more robust against artifacts in the image. As can be seen in the results section, the quantitative differences between MASTeR and GW-CS increase with the reduction factor. This indicates that the GW approach is able to maintain accurate motion estimation even from highly undersampled data. This statement is supported by means of Figure 2.3; the figure shows that both in terms of RE and in terms of TV of the

residual image after registration, the GW approach shows a better performance than the PW counterpart and the parameter RE seems to highlight differences between the two paradigms as the acceleration factor increases.

We would like to point out the effect of ME errors in the reconstructed signal. Fine motion details that the motion model was not able to incorporate were lost in the reconstructed signal. Therefore, to have a robust and versatile motion model is a key aspect in ME/MC based reconstruction methods; Figure 2.6 shows that our method is able to track abnormal motion as well.

In our experiments, the reconstruction parameters used with the volunteers data were set using only one of the three 3T available acquisitions. However, as previously stated, due to the lower signal to noise ratio (SNR) in the patients acquisitions these parameters had to be modified. This indicates, as the compressed sensing theory establishes (Candès et al., 2006; Donoho, 2006), that $\lambda$ and $\lambda_{s/t}$ optimal values strongly depend on the SNR of the acquisitions. This is a common limitation in several CS based reconstruction algorithms that should be addressed. In any case, the parameters were set using only one patient, and they carried over satisfactorily to the other two. On the contrary, the registration parameters $\alpha$ and $\beta$ have been fitted only once for all the experiments. Although their optimal values could change for image modalities with very different contrast or spatio-temporal resolution, these circumstances can be known beforehand. This suggest that in real practice a calibration procedure can be designed.

The GW registration method proposed is more computationally demanding than their PW counterparts, since an optimization problem of higher dimensionality is addressed. However, in our experiments, the computational cost associated to the registration procedure is much lower than the cost of the reconstruction step. Therefore, the relative increase in computational cost due to the registration step has not a considerable effect in the overall algorithm cost.

## 2.6 Conclusions

In this paper we have presented a new CS reconstruction algorithm (GW-CS) based on a regularized, temporal, groupwise registration method. In the proposed algorithm, the whole sequence information is available to the ME method at each registration step instead of just a reference and current frame —as in

k-t FOCUSS— or pairs of adjacent frames —as in MASTeR—. This makes the registration method robust to the incoherent aliasing that appears in highly undersampled data enabling robust estimation of the motion information in the dynamic sequence and achieving further acceleration factors for the same image quality after reconstruction. The non-rigid nature of the B-spline deformation model employed has shown capable of describing the motion of the heart and to recover finer motion details than the block matching method used in k-t FOCUSS.

We understand that our ME/MC scheme is quite flexible: first, the ME method can be easily extended to other image modalities by proper election of the similarity metric. Second, the quasi-static sequence obtained after MC can be highly sparsified by any appropriate transform which may depend on the image modality. Third, the scheme seems compatible with other acquisition strategies rather than Cartesian trajectories (Usman et al., 2013). Finally, given the high acceleration factors achieved, the proposed approach could be naturally extended to real-time imaging of the heart or other moving parts of the body (Uecker et al., 2012). These possibilities will be explored in future work.

## Acknowledgments

The authors would like to thank Claudia Prieto and Muhammad Usman collaboration in the acquisition of the 1.5T raw data at King's College London. This work was partially supported by the Junta de Castilla y León under grant VA136U13, Instituto de Salud Carlos III PI11-01492, Ministerio de Economía y Competitividad under grant TEC2013-44194-P and by the University of Valladolid and Banco Santander FPI-UVa Fellowship Program.

## Supporting material

This section indexes the supplementary material that can be found in the electronic version of the publication. The code implementing the methods described in this publication and the supplementary material are available as well with the electronic version of this Thesis and at the website of the author at

`http://www.lpi.tel.uva.es/~jroyval`

**Supporting Figure 1:** Reconstruction parameters selection. One of the multicoil datasets has been reconstructed for a fixed acceleration factor of 6 with several possible values of the parameters $\lambda_t$ and $\lambda_{s/t}$. The final parameters are chosen so that the quality metrics SER and SSIM get maximun values. The optimal values of the parameters could vary for different signals and acceleration factors; however, no significant differences have been observed. Therefore, $\lambda_t$ and $\lambda_{s/t}$ remained the same in the rest of the experiments.

**Video 1:** Video showing the effect of the groupwise motion compensation operator. The fully sampled 1.5T sequence is played on the left half of the video and the motion compensated one on the right half. The whole sequence is displayed followed by a zoom of a region of interest (ROI) around the heart. The estimated spatial deformation is superposed for visualization.

**Video 2:** Video showing the effect of corrupted motion estimation on the final reconstruction. A fully sampled acquired 3T sequence is played on the left part. In the center and right parts a MASTeR and a GW-CS with TV reconstructions of the 10-fold undersampled sequence is shown. MASTeR reconstruction presents a motion artifact due to error induced by non-coherent aliasing during motion estimation.

**Video 3:** Video showing the reconstructions of the 1.5T dataset with a 12-fold acceleration factor. From left to right: fully sampled sequence, k-t FOCUSS with ME/MC, MASTeR, GW-CS with TV and GW-CS with CWT are shown.

**Video 4:** Video showing the reconstructions of one of the 3T acquired datasets with a 12-fold acceleration factor. From left to right: fully sampled sequence, k-t FOCUSS with ME/MC, MASTeR, GW-CS with TV and GW-CS with CWT are shown.

**Video 5:** Video showing the reconstructions of a sequence with abnormal cardiac motion. From left to right: fully sampled sequence and acceleration factors of 2, 4 and 8.

**Video 6:** Video showing the reconstructions of a 32-coil, healthy volunteer dataset. From left to right, fully sampled sequence and acceleration factors of 2, 4, 8 and 12. In the last two cases, high frequency artifacts and loss of quality become relevant.

CHAPTER

# THREE

# JACOBIAN WEIGHTED TEMPORAL TOTAL VARIATION FOR MOTION COMPENSATED COMPRESSED SENSING RECONSTRUCTION OF DYNAMIC MRI

**Published as:**

Javier Royuela-del-Val[1], Lucilio Cordero-Grande[2], Federico Simmross-Wattenberg[1], Marcos Martín-Fernández[1] and Carlos Alberola-López[1] (2017), Jacobian Weighted Temporal Total Variation for Motion Compensated Compressed Sensing Reconstruction of Dynamic MRI. Magnetic Resonance in Medicine, 77(3):1522-2594

[1]Laboratorio de Procesado de Imagen, Universidad de Valladolid, Valladolid, Spain.

[2]Centre for the Developing Brain, Division of Imaging Sciences and Biomedical Engineering, King's College London, London, UK.

Royuela2016a

**Abstract**

**Purpose:** To eliminate the need of spatial intra-frame regularization in a recently reported dynamic MRI compressed-sensing based reconstruction method with motion compensation and to increase its performance.

**Theory and Methods:** We propose a new regularization metric based on the introduction of a spatial weighting measure given by the Jacobian

of the estimated deformations. It shows convenient discretization properties and, as a byproduct, it also provides a theoretical support to a result reported by others based on an intuitive design. The method has been applied to the reconstruction of both short and long axis views of the heart of four healthy volunteers. Quantitative image quality metrics as well as straightforward visual assessment are reported.

**Results:** Short and long axis reconstructions of cardiac cine MRI sequences have shown superior results than previously reported methods both in terms of quantitative metrics and of visual assessment. Fine details are better preserved due to the lack of additional intra-frame regularization, with no significant image artifacts even for an acceleration factor of 12.

**Conclusions:** The proposed Jacobian Weighted temporal Total Variation results in better reconstructions of highly undersampled cardiac cine MRI than previously proposed methods and sets a theoretical ground for forward and backward predictors used elsewhere.

**Keywords:** Dynamic MRI reconstruction; compressed sensing; groupwise registration; motion estimation

## 3.1 Introduction

Temporal TV (tTV) has provided good results in dynamic MRI reconstruction methods (Adluru et al., 2009; Feng et al., 2013, 2014) based on the compressed sensing (CS) theory (Donoho, 2006; Candès et al., 2006). However, these methods remain sensitive to large inter frame motion usually present in dynamic MRI due to breathing, phase misalignments in, e.g., cardiac perfusion, or the natural motion of the heart in cine MRI. Since this motion reduces the sparsity of the signal, the achievable acceleration factor shrinks as well.

Several methods in the literature introduce some knowledge about motion to promote signal sparsity prior to the computation of the tTV; the underlying assumption is that motion can be described with fewer parameters than the changes it introduces in the dynamic sequence (Prieto et al., 2007). In MASTeR (Asif et al., 2013), motion between each pair of consecutive frames in cardiac cine MRI is estimated from an initial reconstruction and used to predict adjacent frames. Residuals between the actual and predicted frames are assumed

sparse. In order to prevent bias, motion is estimated both forwards (FW) and backwards (BW). In the deformation corrected (DC)–CS framework proposed by Lingala et al. (2015) the dynamic sequence and the inter frame motion are jointly estimated and the overall procedure is applied to compensate for respiratory motion in cardiac perfusion imaging. In addition, the sparse domain can be chosen independently of the motion estimation procedure. In our previous works, GW-CS (Royuela-del Val et al., 2016a), a related approach is presented. The ME step is based on a B-spline deformation model and on a GW temporal registration algorithm; the procedure turns out to be robust to the artifacts introduced by the undersampled acquisition. However, the motion compensation operator led to image artifacts in the reconstructed image. Therefore, a spatial regularization term was introduced to eliminate these artifacts at the cost of increasing, consequently, the complexity of the method.

In this paper, we propose a new sparse regularization term given by the inclusion of the Jacobian of the estimated non-rigid deformation in the DC-tTV. This regularization term, hereafter referred to as Jacobian Weighted tTV (JW-tTV), has a three fold advantage, namely: 1) avoids the presence of the reconstruction artifacts, eliminating the need of additional spatial regularization, 2) has convenient discretization properties that facilitate its implementation and 3) provides theoretical support for the FW and BW motion operators introduced empirically in MASTeR. The modified tTV has been applied to the reconstruction of cine sequences following the scheme in GW-CS.

## 3.2 Theory

### Dynamic MRI Compressed Sensing Reconstruction

We represent the MRI sequence to be reconstructed $m$ as a stack of $N$ continuous 2D images $m_n(\boldsymbol{x})$, with spatial location $\boldsymbol{x} \in \mathcal{X} \subset \mathbb{R}^2$ and temporal index $n = 1, 2, \ldots, N$. Once noise decorrelation is applied, the acquired MRI data can be modeled as (Pruessmann et al., 1999)

$$\mathbf{y}_{n,c} = \int_{\boldsymbol{x}\in\mathcal{X}} m_n(\boldsymbol{x}) S_c(\boldsymbol{x}) \exp\left(-i\mathbf{k}_n^T \boldsymbol{x}\right) \mathrm{d}\boldsymbol{x} + \mathbf{n}_{n,c} \tag{3.1}$$

where $\mathbf{k}_n$ represents the set of k-space positions sampled at the indexed time $n$, $S_c(\boldsymbol{x})$ the sensitivity profile of each coil in parallel MRI and $\mathbf{n}_{n,c}$ a circularly

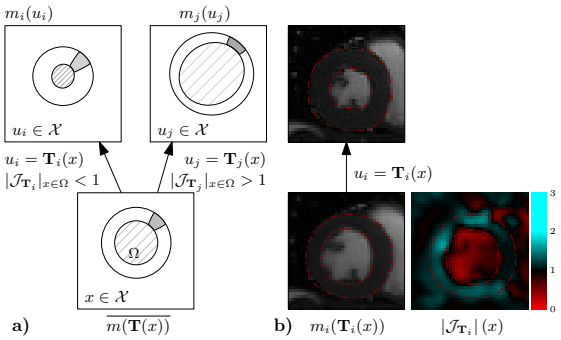


c)

| | Motion Estimation | Sparse Regularization |
|---|---|---|
| MASTER | Pairwise sequential, Forward/Backward | Sequential DC-tTV, Forward/Backward |
| GW-CS | Groupwise | Groupwise DC-tTV + Spatial regularization |
| Proposed | Groupwise | JW-tTV |

Figure 3.1: a) Diagram of a SA view of the heart and the spatial deformations that map the reference configuration in material point coordinate system (bottom) to the systolic (top left) cardiac phase. At systole, the blood pool (lined regions) contracts, so the Jacobian of the deformation takes values lower than the unit in that region. On the contrary, the cardiac muscle thickens (shadowed regions) in the 2D view, so the Jacobian is greater than one in the myocardium. At diastole (top right), the situation is reversed. b) Example on real data at systole (top) and in the reference configuration (bottom left). Dashed circles delineate the myocardium. At bottom right, the spatial distribution of the Jacobian (bottom right) agrees with a). c) Table summarizing the main differences between MASTER, GW-CS and the proposed method. Analytically our sparse regularization term turns out to coincide with the one used by MASTER; however, we prefer to use the name JW-tTV to emphasize its origin.

symmetric white Gaussian noise. In vector form, Eq. (3.1) can be rewritten as

$$\mathbf{y} = \mathbf{E}(m) + \mathbf{n} \tag{3.2}$$

where the operator $\mathbf{E}$ comprises the multiplication by coil sensitivities and the evaluation of the Fourier transform (FT) at the k-space positions $\mathbf{k}_n$ for $n = 1, 2, \ldots, N$.

Under the CS theory, the sequence $m$ can be recovered from the undersampled data $\mathbf{y}$ by solving the following minimization problem (Feng et al., 2014)

$$\hat{m} = \arg\min_{m} \ \frac{1}{2}\|\mathbf{y} - \mathbf{E}(m)\|_{\ell_2}^2 + \lambda\|\Psi(m)\|_{\ell_1} \tag{3.3}$$

where $\ell_1$ regularization term promotes sparsity of the solution in the transformed domain given by $\Psi$. For cardiac cine MRI, tTV has been successfully applied and can be defined

$$\|\nabla_t(m)\|_{\ell_1} = \frac{1}{|\mathcal{X}|N} \int_{\boldsymbol{x}\in\mathcal{X}} \sum_{n=1}^{N} |m_{n+1}(\boldsymbol{x}) - m_n(\boldsymbol{x})| \ \mathrm{d}\boldsymbol{x} \tag{3.4}$$

where cyclical motion has been considered by setting $m_{N+1}(\boldsymbol{x}) = m_1(\boldsymbol{x})$.

### Jacobian Weighted tTV with Motion Compensation

In order to compensate for the inter frame motion, we introduce a motion compensation operator $\mathcal{T}_{\boldsymbol{\Theta}}$ that deforms each of the cardiac phases to a common, average, motion state. The transform is governed by the set of parameters $\Theta$. The resulting reference configuration can be regarded as a material point coordinate system. However, as discussed by Royuela-del Val et al. (2016a), its direct application may lead to severe artifacts in the regions of the reconstructed images where large deformations are involved.

Moreover, when the tTV is computed after the application of $\mathcal{T}_{\boldsymbol{\Theta}}$, the accumulated differences are implicitly weighted according to their corresponding areas in the motion corrected sequence $\mathcal{T}_{\boldsymbol{\Theta}}(m)$, as opposed to those in the one to be reconstructed; this is illustrated in Figure 3.1a, where a diagram shows the change in area induced by the spatial deformation and how it relates to its Jacobian*. Intuitively, when the transformation gives rise to a contraction —Jacobian lower than 1—, it will be over-regularized during reconstruction, since it occupies a larger area in the reference configuration. Contrarily, enlarged areas —Jacobian higher than 1— will be under-regularized. Figure 3.1b shows an example of the spatial distribution of the Jacobian at systole on real data. In Supporting Video 1, the example is reproduced for the whole cardiac cycle.

Consequently, we propose to counteract this effect by locally weighting each temporal difference according to its corresponding area in the original sequence. We define a JW-tTV regularization term given by†:

$$\|m\|_{\mathcal{T}_\Theta} = \frac{1}{|\mathcal{X}|N} \int_{\boldsymbol{x}\in\mathcal{X}} \sum_{n=1}^{N} |m_{n+1}(\mathbf{T}_{n+1}(\boldsymbol{x})) - m_n(\mathbf{T}_n(\boldsymbol{x}))|\, \mathcal{J}_{\mathbf{T}_{n+1/2}}(\boldsymbol{x})\, \mathrm{d}\boldsymbol{x} \quad (3.5)$$

where $\boldsymbol{u}_n = \mathbf{T}_n(\boldsymbol{x})$ stands for the spatial deformation that maps each material point $\boldsymbol{x}$ in the motion compensated sequence to its corresponding spatial location $\boldsymbol{u}_n$ at instant $n$. Given the discrete nature of index $n$, the transformation Jacobian at $n + 1/2$ is approximated by

$$\mathcal{J}_{\mathbf{T}_{n+1/2}}(\boldsymbol{x}) \approx \frac{1}{2}\left[\mathcal{J}_{\mathbf{T}_n}(\boldsymbol{x}) + \mathcal{J}_{\mathbf{T}_{n+1}}(\boldsymbol{x})\right] \quad (3.6)$$

*Notice that although $\mathcal{T}_{\boldsymbol{\Theta}}(m)$ stands for the motion corrected sequence, transformations are actually defined in the opposite direction, i.e., from material coordinates to spatial coordinates.

†We consider that motion is entirely located within the image boundaries so integration domains do not effectively change with the change of variables.

what allows us, after permuting summation and integration orders, to split Eq. (3.5):

$$\|m\|_{\mathcal{T}_\Theta} \propto \sum_{n=1}^{N} \Big\{ \int_{\boldsymbol{x}\in\mathcal{X}} |m_{n+1}(\mathbf{T}_{n+1}(\boldsymbol{x})) - m_n(\mathbf{T}_n(\boldsymbol{x}))|\, \mathcal{J}_{\mathbf{T}_n}(\boldsymbol{x})\, \mathrm{d}\boldsymbol{x} + \int_{\boldsymbol{x}\in\mathcal{X}} |m_{n+1}(\mathbf{T}_{n+1}(\boldsymbol{x})) - m_n(\mathbf{T}_n(\boldsymbol{x}))|\, \mathcal{J}_{\mathbf{T}_{n+1}}(\boldsymbol{x})\, \mathrm{d}\boldsymbol{x} \Big\} \tag{3.7}$$

By means of the changes of variable $\mathbf{T}_n(\boldsymbol{x}) = \boldsymbol{u}_n \rightarrow \mathcal{J}_{\mathbf{T}_n}(\boldsymbol{x})\mathrm{d}\boldsymbol{x} = \mathrm{d}\boldsymbol{u}_n$ and $\mathbf{T}_{n+1}(\boldsymbol{x}) = \boldsymbol{u}_{n+1} \rightarrow \mathcal{J}_{\mathbf{T}_{n+1}}(\boldsymbol{x})\mathrm{d}\boldsymbol{x} = \mathrm{d}\boldsymbol{u}_{n+1}$ we write:

$$\|m\|_{\mathcal{T}_\Theta} \propto \sum_{n=1}^{N} \Big\{ \int_{\boldsymbol{u}_n\in\mathcal{X}} |m_{n+1}(\mathbf{T}_{n+1,n}(\boldsymbol{u}_n)) - m_n(\boldsymbol{u}_n)|\, \mathrm{d}\boldsymbol{u}_n + \int_{\boldsymbol{u}_{n+1}\in\mathcal{X}} |m_{n+1}(\boldsymbol{u}_{n+1}) - m_n(\mathbf{T}_{n,n+1}(\boldsymbol{u}_{n+1}))|\, \mathrm{d}\boldsymbol{u}_{n+1} \Big\} \tag{3.8}$$

where we have defined $\mathbf{T}_{i,j} = \mathbf{T}_i \circ \mathbf{T}_j^{-1}$ —details on how to obtain $\mathbf{T}_j^{-1}$ are provided in the Appendix—. That is, $\mathbf{T}_{i,j}$ deforms $m_i$ to $m_j$ (Metz et al., 2011). In Eq. (3.8) we return from the common material point coordinate system to the local spatial system of each frame while retaining the motion information from $\mathcal{T}_\Theta$. Defining $B_i(m_i) = m_i \circ \mathbf{T}_{i,i-1}$ and $F_i(m_i) = m_i \circ \mathbf{T}_{i,i+1}$,

$$\|m\|_{\mathcal{T}_\Theta} \propto \sum_{n=1}^{N} \int_{\boldsymbol{u}\in\mathcal{X}} \|B_{n+1}(m_{n+1}) - m_n\|_{\ell_1} + \|F_n(m_n) - m_{n+1}\|_{\ell_1} \mathrm{d}\boldsymbol{u} \tag{3.9}$$

where $B_i$ and $F_i$ are two motion operators that map each frame $i$ onto its previous (BW) and following (FW) frames, respectively. In Eq. (3.9) the dependence of the integrand with $\boldsymbol{u}$ is omitted for notational simplicity.

It is worth mentioning that Eq. (3.9) resembles the regularization term used in MASTeR (Asif et al., 2013). With our result we provide theoretical support for the use of both BW and FW motion operators empirically introduced in that work. Moreover, while in MASTeR these operators arise directly from the sequential ME technique applied, in our proposal they are obtained from $\mathcal{T}_\Theta$ regardless of the ME technique used. This enables us to apply a GW temporal registration scheme which has shown more robustness to undersampling artifacts than sequential methods (Royuela-del Val et al., 2016a). Figure 3.1c summarizes the differences between the proposed method, the original GW-CS and MASTeR.

**input:**

**y**: undersampled k-t data

**E**: encoding operator

$\lambda$: sparsity regularization parameter

**initialization:**

$k \leftarrow 0$

$m^0 \leftarrow$ Eq. (3.3); initial CS reconstruction.

**while** $k < k_{max}$. number of iterations **do**

$\Theta^{k+1} \leftarrow$ GW temporal registration. See Royuela-del Val et al. (2016a) for details.

$m^{k+1} \leftarrow$ CS reconstruction. Solve Eq. (3.11) for $\Theta^{k+1}$. (For comparison, at this step the original GW-CS algorithm solves Eq. (3.10)).

$k \leftarrow k + 1$

**end**

**output:** $\hat{m} = m^{k_{max}}$

Table 3.1: Implementation of JW-tTV based reconstruction of undersampled dynamic MRI.

## 3.3 Methods

The objective function on which GW-CS is grounded is:

$$\hat{m} = \arg\min_m \frac{1}{2}\|\mathbf{y} - \mathbf{E}(m)\|_{\ell_2}^2 + \lambda_t \|\nabla_t(\mathcal{T}_\Theta(m))\|_{\ell_1} + \lambda_s \|\Psi(m)\|_{\ell_1} \tag{3.10}$$

with $\Psi$ a spatial wavelet transform. In this paper, the $\ell_1$ terms are substituted by the JW-tTV term (Eq. 3.8); the last term, which is the spatial regularization term, is dropped. The JW-tTV reconstruction is then formulated as

$$\hat{m} = \arg\min_m \frac{1}{2}\|\mathbf{y} - \mathbf{E}(m)\|_{\ell_2}^2 + \lambda \|m\|_{\mathcal{T}_\Theta} . \tag{3.11}$$

A scheme of the proposed algorithm follows is presented in Table 3.1

In the implementation $m$ is discretized in a regular Cartesian grid and interpolation is used to compute $\mathcal{T}_\Theta(m)$. In our experiments, a bicubic interpolation provided better reconstructions than the bilinear scheme used in Royuela-del Val et al. (2016a) without a noticeable increment in computational cost. The whole reconstruction algorithm was implemented in MATLAB (MathWorks, Natick,

MA) and the optimization problems in Equations (3.3) and (3.9) were solved with the NESTA algorithm (Becker et al., 2011) on a PC with two Intel XEON E5-2695 v3 @ 2.30GHz with 14 cores and 64 GB of RAM.

The parameter $\lambda$ was fitted to achieve the highest SER —defined later— in a region around the heart for one of the datasets for an acceleration factor of 8 and kept constant for the rest. The same approach was followed to fit $\lambda_t$ and $\lambda_s$ in GW-CS. The obtained values are $\lambda = 0.01$, $\lambda_t = 0.003$ and $\lambda_s = 0.0003$. For the experiments in Figure 3.4a (see below), in which the proposed method is complemented with a spatial regularization term at the only purpose of comparison, its weight is set to 0.001 (with the original $\lambda$ kept constant).

Two quantitative error metrics were used for reconstruction comparison. Firstly, the signal–to–error ratio (SER), defined as

$$\text{SER(dB)} = 20 \log_{10} \frac{\|m\|_{\ell_2}}{\|m - \hat{m}\|_{\ell_2}},$$

where $m$ denotes the fully sampled image and $\hat{m}$ the image reconstructed from undersampled data. Second, the structural similarity index —SSIM— (Wang et al., 2004) was also used as a complementary quantitative metric.

### In vivo experiments

SA and long axis (LA) views of the heart were obtained from four healthy volunteers on a 3T Philips Achieva equipment with a 32-element cardiac coil. Other relevant scan parameters include: b-SSFP sequence, TR/TE/flip angle = 3.3 ms/1.57 ms/45°, FOV = 320×320 mm$^2$ and slice thickness = 8 mm. 30 cardiac phases were reconstructed with retrospective ECG synchronization. Fully sampled images were converted back to k-t space and considered as single coil acquisitions. Data was retrospectively undersampled with an inhomogeneous sampling pattern following a Gaussian distribution along the phase encoding direction simulating different acceleration factors ranging from 2 to 12.

## 3.4 Results

Figure 3.2 shows the reconstruction of a midventricular SA slice with the four methods compared —regular CS reconstruction with tTV, MASTeR, original

GW-CS and JW-tTV—. Temporal profiles, corresponding frames at systole and error images are shown. Figure 3.3 shows the equivalent results obtained for a left two-chambers view of the same dataset.

Methods with motion compensation outperform regular CS for high acceleration factors. However, MASTeR shows a faster degradation of the image quality that is more evident in the temporal profiles in Figures 3.2b and 3.3b, where the edges of the myocardial are severely distorted and some erratic motion can be observed —white arrows—. This effect, clearly appreciable in Supporting Videos 2 and 3, is due to the sequential ME technique applied, which turns out to be affected by the strong undersampling artifacts present in the initial reconstruction. As for GW-CS, we can see how dynamic behavior is better preserved given the more robust ME technique. However, in Figures 3.2c and 3.3c, structure edges become more blurred for high acceleration factors due to the spatial regularization introduced. Still; however, some residual high frequency artifacts remain for the highest acceleration factor. With JW-tTV there is no need of such a spatial regularization and myocardium edges as well as papillary muscles are better preserved. In the LA views, the mitral valve can be appraised both in MASTeR and the JW-tTV reconstructions for an acceleration factor of 8; however, in GW-CS the spatial regularization hinders the retrieval of such a small structure from the undersampled data —white arrows—.

In order to analyze the effects of the proposed JW-tTV and the spatial regularization separately, in Figure 3.4a one SA view has been reconstructed with both the original GW-CS method and with JW-tTV with and without a spatial regularization term based on the complex wavelet transform (CWT). The GW-CS reconstruction without spatial regularization shows high frequency artifacts, specially at end-diastole and systole, which are removed with spatial regularization; however, edge sharpness is strongly affected and thin details are lost. In the proposed method, the additional spatial regularization does not involve an appreciable improvement in image quality but affects complexity and computational cost of the algorithm. The sensitivity of the algorithm to different initializations is analyzed in Figure 3.4b. Three different sequences where used as initial guesses; namely, the ground truth images from the fully sampled data, an initial CS reconstruction with tTV and an initial CS reconstruction spatially over-regularized with CWT. Both the visual appearance and quantitative metrics shown are very similar in the three cases, with slight superior scores for the fully sampled initialization. These results suggest that the method is robust against

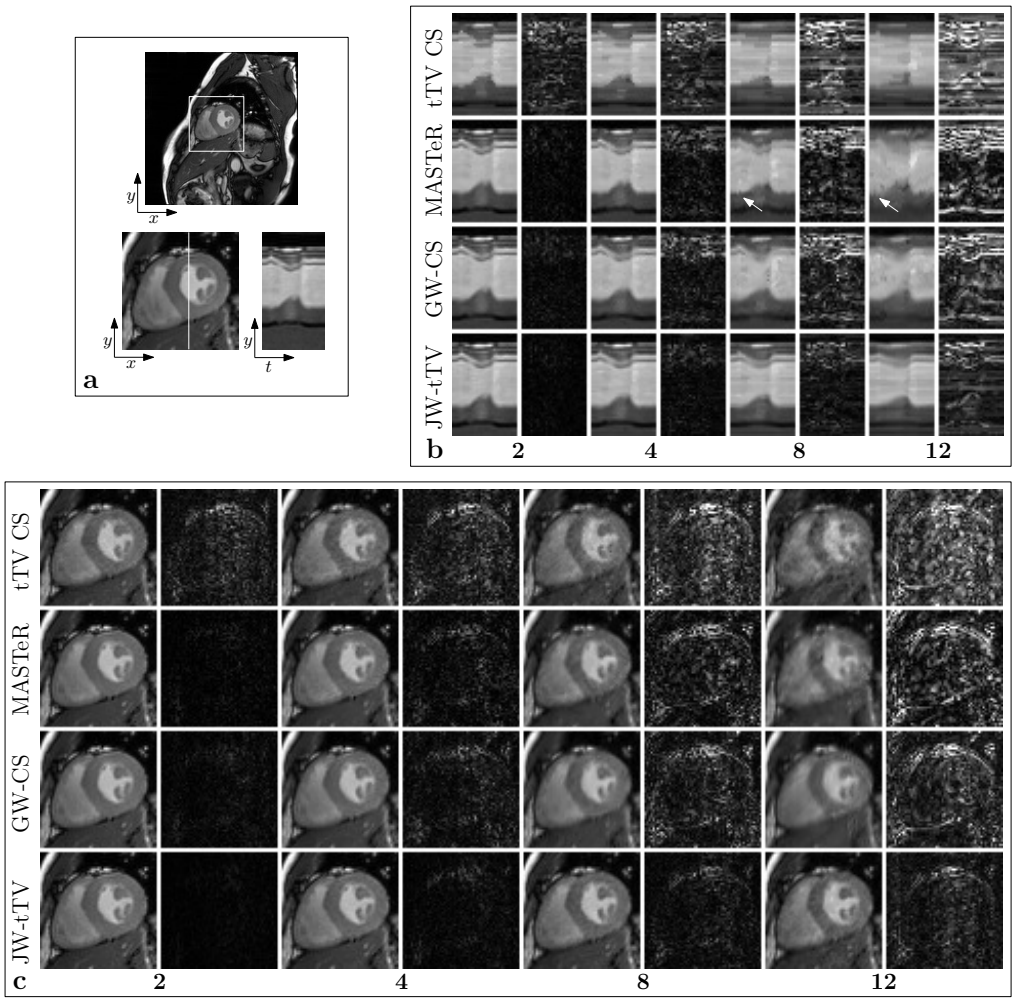


Figure 3.2: Reconstructions of a short axis view of the heart. (a) Fully sampled systole phase with square ROI around the heart (top), detail of the ROI (bottom left) and temporal profile of a single slice along the indicated vertical line (bottom right). (b) Temporal profiles of the reconstructions with regular tTV regularization without motion compensation, MASTeR, the original GW-CS and the proposed method for the indicated acceleration factors ranging from 2 to 12. Difference images with respect to the fully sampled image appear next to each profile, multiplied by a scale factor of 5. (c) Reconstructed short axis views as in (b). White arrows indicate some erratic motion present in MASTeR reconstructions for high acceleration factors.

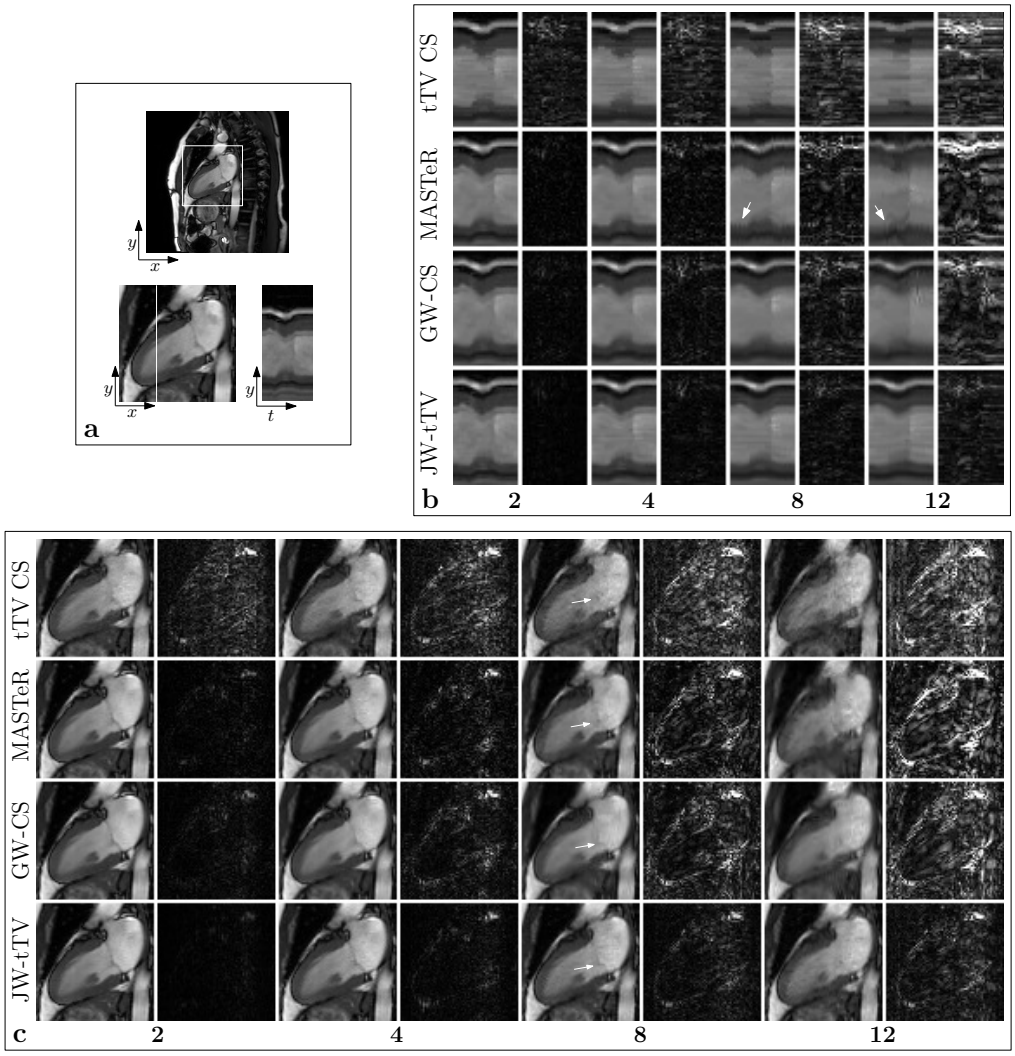


Figure 3.3: Reconstructions of a left two chambers view of the heart, presented following the same scheme as that in Figure 3.2. (a) Fully sampled systole phase with square ROI, detail of the ROI (bottom left) and temporal profile of a single slice (bottom right). (b) Temporal profiles and error images (scale factor of 5) of the reconstructions with the four compared methods for the indicated acceleration factors. (c) Reconstructed LA views as in (b). White arrows indicate the position of the mitral valve.

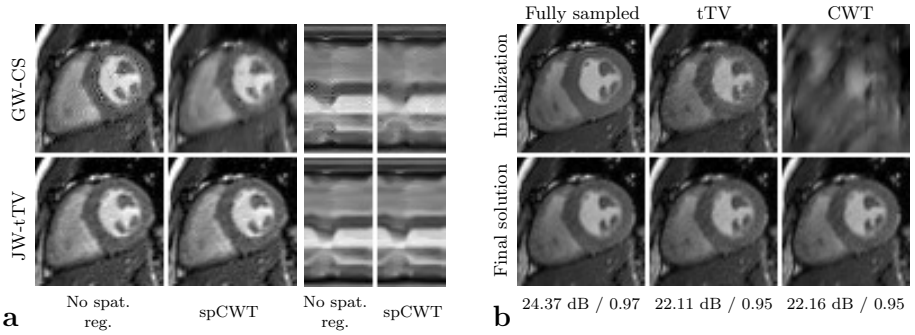


Figure 3.4: (a) Effects of the spatial regularization in a short axis view reconstruction. Systolic phase and temporal evolution of a horizontal line across left and right ventricles are shown. (b) Effect of different initializations (fully sampled, tTV and CWT) on the proposed algorithm. SER (dB) and SSIM index in the region of interest are shown below each final reconstruction. An acceleration factor of 10 was used.

large differences in the initialization and, as it iterates, it is able to recover from poor initial guesses.

In Figure 3.5 plots of the SER and SSIM obtained for the reconstructions of the four SA datasets are represented. Both GW-CS and JW-tTV outperform MASTeR reconstructions in terms of SER and SSIM and differences increase with the acceleration factor. However, there is no appreciable difference between the GW-CS and JW-tTV in terms of these quantitative metrics. We understand that achieving comparable performance with one less control parameter and with better edge definition is worth taking.

## 3.5 Discussion and Conclusions

In this work we have proposed a modification of the tTV metric commonly used in the CS reconstruction of dynamic MRI sequences by means of a weighting factor given by the Jacobian of the transformation $\mathcal{T}_\Theta$ that maps the position of each point in the motion compensated sequence to its corresponding position in the original sequence. At first sight, this could be regarded as an adaptive TV related to the one proposed in (Kamesh Iyer et al., 2012), where spatial TV regularization is leveraged in the presence of spatial edges to preserve sharpness. However, in our proposal we intend to account for the effect of the relative size of each region in the image, regardless of the underlying structures.

With this modification, the resulting tTV metric resembles the regularization term proposed in MASTeR (Asif et al., 2013). However, in this case the-

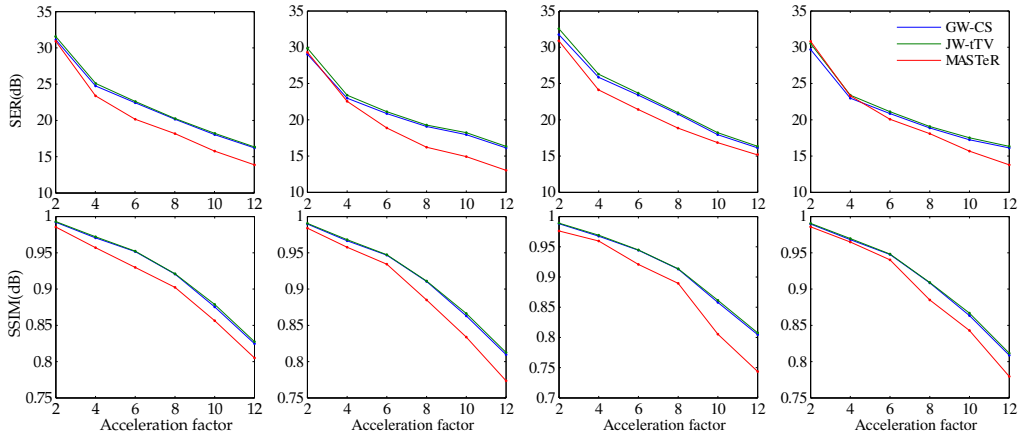


Figure 3.5: SER(dB) and SSIM index calculated over a ROI around the heart in the SA views for the four volunteers with the proposed metric, original GW-CS and MASTeR.

oretical support has been given to the inclusion of both FW and BW motion compensation terms and the definition of these terms has been made independent of the ME technique. This has allowed us to apply the robust GW temporal registration approach previously proposed in GW-CS so differences with respect to MASTeR are maintained; with the JW-tTV modification proposed in this paper, there is no need of the additional spatial regularization introduced in GW-CS —the term weighted by $\lambda_s$ in Eq. (3.10)—, a fact of great importance since now sharper edges and small details in the images, even for acceleration factors as high as 12, are maintained. The erratic motion observed in MASTeR reconstructions for high acceleration factors —see Supporting Video 2 for factor 8 and beyond— reveals how the final reconstruction may be corrupted by ME errors, which occasionally could be misinterpreted as false cardiac function abnormalities. This fact makes even clearer the need of a robust ME technique as we understand ours is. In any case, the impact of motion artifacts should be further studied to validate the clinical utility of these methods at such high acceleration factors.

As indicated in Eq. (3.8), the transform $\mathcal{T}_\Theta$ that results from the estimated motion should be invertible. Proper spacing of the B-splines control points and the introduction of a regularization term (see the Appendix) encourages its invertibility. Even though this property is not strictly guaranteed, the experiments realized so far have always led to invertible transforms.

The presented experiments have been performed simulating an undersampled acquisition in Cartesian trajectories. Execution times at the different accel-

eration factors and orientations considered and for the four volunteers datasets ranged 8–10 min for MASTeR reconstruction, 15–22 min for GW-CS and 11–18 min for JW-tTV. Generally speaking, higher acceleration factors led to faster reconstructions given the lesser data involved. The higher execution times of GW-CS and JW-tTV with respect to MASTeR are mainly due to the GW registration; an additional advantage of JW-tTV is the lower execution time due to the elimination of the spatial regularization term. Needless to say, these methods could benefit from more efficient implementations in compiled languages and its execution on GPU devices.

This registration method can be easily extended to other image modalities where the assumption of constant pixel intensity does not hold —as in contrast enhanced MRI— by proper election of the similarity metric (Cordero-Grande et al., 2013). Moreover, the advanced normalization tools (ANTs) package (Avants et al., 2011) provides versatile diffeomorphic registration methods in which the invertibility of the deformation is guaranteed. The adaptation of these methods to our application will be studied. As for the sparsity term, in this situation the introduction of the Jacobian weighting is not directly applicable to common sparse representations such as the temporal Fourier transform. However, higher order temporal differences could be used in Eq. (3.5) to enforce smooth evolution of single pixel intensities while preserving from staircase effects. This approach has shown to be very effective when applied in the spatial domain (Knoll et al., 2011) and will be further explored.

# Appendix

## Inversion of the deformation field

In order to define the operator $\mathbf{T}_{i,j}$, the inverse transformation $\mathbf{T}_j^{-1}$ is needed. Since the inverse of a B-spline cannot be analytically obtained, a numerical optimization approach is adopted. In general, $\mathbf{T}_j^{-1}$ will not be a B-spline transform. Therefore we directly look for the set of material points $\boldsymbol{x}_n$ that, when mapped by $\mathbf{T}_n$, result in the regular Cartesian grid of spatial locations in which the original images are discretized —see implementation description—. To this end, for each $n$ we solve

$$\boldsymbol{x}_n^* = \arg\min_{\boldsymbol{x}} \sum_{\boldsymbol{u}_n \in \mathcal{X}'} \|\mathbf{T}_n(\boldsymbol{x}) - \boldsymbol{u}_n\|_{\ell_2}^2 \tag{3.12}$$

with $\mathcal{X}'$ the set of discrete pixels in $\mathcal{X}$, using nonlinear conjugate gradient optimization. Solving Eq. (3.12) is equivalent to storing an approximation of the evaluation of $\mathbf{T}_n^{-1}$ for every $\boldsymbol{u}_n \in \mathcal{X}'$. We approximate $\mathbf{T}_{i,j}(\boldsymbol{u}_j) \mid_{\boldsymbol{u}_j \in \mathcal{X}'} = \mathbf{T}_i(\mathbf{T}_j^{-1}(\boldsymbol{u}_j)) \mid_{\boldsymbol{u}_j \in \mathcal{X}'} \approx \mathbf{T}_i(\boldsymbol{x}_j^*)$. The previous approach has the advantage that no deformation model assumption for $\mathbf{T}_n^{-1}$ is needed. On the other side, it is only valid for the set of points in $\mathcal{X}'$ for which Eq. (3.12) is solved, which is compatible with the reconstruction method at hand.

In the registration algorithm, even though the invertibility of $\mathbf{T}_n$ is not guaranteed, it is enforced by proper selection of the spacing between B-spline deformation control points and the regularization of the deformation fields with a term related to the elastic energy of the transformation (Rueckert et al., 1999) —see (Royuela-del Val et al., 2016a) for details—. In our experiments, control point spacing was 4 mm along both spatial dimensions. The weight given to the regularization term was tuned to minimize the residual motion —measured as the tTV— when the deformations estimated from an initial CS reconstruction at an acceleration factor of 8 were applied to the corresponding fully sampled sequence. This way, the registration method is made robust against residual undersampling artifacts and prevented from becoming non-invertible, while keeping it flexible enough to describe cardiac motion.

# Supporting material

This section indexes the supplementary material that can be found in the electronic version of the publication. The code implementing the methods described

in this publication and the supplementary material are available as well with the electronic version of this Thesis and at the website of the author at

`http://www.lpi.tel.uva.es/~jroyval`

**Supporting Video 1:** Motion estimation and compensation on a fully sampled short axis view of the heart. From left to right and top to bottom: original sequence, original sequence with the estimated deformation plotted in red, motion compensated sequence and spatial distribution of the Jacobian of the deformation along the cardiac cycle.

**Supporting Video 2:** Reconstruction of a short axis view of the heart with a regular CS reconstruction method with tTV, MASTeR, the original GW-CS method and the proposed JW-tTV for acceleration factors 2, 4, 8 and 12.

**Supporting Video 3:** Reconstruction of a long axis view of the heart with a regular CS reconstruction method with tTV, MASTeR, the original GW-CS method and the proposed JW-tTV for acceleration factors 2, 4, 8 and 12.

CHAPTER

# FOUR

# SINGLE BREATH HOLD WHOLE HEART CINE MRI WITH ITERATIVE GROUPWISE CARDIAC MOTION COMPENSATION AND SPARSE REGULARIZATION (KT-WISE)

**Published as:**

Javier Royuela-del-Val[1], Muhammad Usman[2], Lucilio Cordero-Grande[2], Federico Simmross-Wattenberg[1], Marcos Martín-Fernández[1], Claudia Prieto[2] and Carlos Alberola-López[1]. Single Breath Hold Whole Heart Cine MRI With Iterative Groupwise Cardiac Motion Compensation and Sparse Regularization (kt-WiSE). Proceedings of the 23th Anual Meeting of the International Society of Magnetic Resonance in Medicine (ISMRM 2015). Toronto, CA.

[1] Laboratorio de Procesado de Imagen, Universidad de Valladolid, Valladolid, Spain.

[2] Division of Imaging Sciences and Biomedical Engineering, Centre for the Developing Brain, King's College London, London, UK.

## 4.1 Purpose

Multi–slice 2D (M2D) cine MRI is a clinical gold standard for the assessment of ventricular volumes and cardiac function. However, this acquisition currently

needs to be performed during several BHs, leading to slice-misalignment and long scans duration. In this work we propose a novel undersampled reconstruction approach to perform M2D whole heart cine MRI in a single breath hold. The proposed method, which we call kt-WiSE, is based on CS and a groupwise temporal registration algorithm for the estimation and compensation of the motion of the heart. The proposed approach was tested on healthy volunteers with data acquired on a golden radial trajectory (Winkelmann et al., 2007), and compared against the gold standard M2D acquisition.

## 4.2 Theory

Compressed sensing has been shown to highly accelerate cine MRI by exploiting sparsity of the signal in the temporal domain (Otazo et al., 2010). MC has been incorporated into the CS reconstruction to achieve sparser temporal representations by reducing inter-frame cardiac motion, as previously proposed by Prieto et al. (2007) and Lingala et al. (2015). These MC-CS methods enable higher acceleration factors, however present remained artifacts due to motion estimation/compensation errors. To overcome these problems we propose a joint optimization approach for the image $\mathbf{m}$ and motion parameters. This MC-CS approach uses a spatio-temporal regularized groupwise registration algorithm based on a non-rigid B-splines deformation model and can be formulated as iteratively solving the following equations (4.1) and (4.2). First:

$$\underset{\mathbf{m}}{\text{minimize}} \|\mathbf{y} - \mathbf{E}\mathbf{m}\|_2^2 + \lambda \|\mathbf{\Psi}\mathcal{T}_\Theta \mathbf{m}\|_{\ell_1} \tag{4.1}$$

where $\mathbf{E}$ stands for the encoding operator (including gridding and coil maps), $\mathbf{\Psi}$ for sparsity transform and $\mathcal{T}_\Theta$ for the spatial deformation associated to the motion of the heart. $\mathcal{T}_\Theta$ is parameterized by a regular grid of control points $\Theta$. Since no motion is known in the first iteration, an initial CS reconstruction is performed with $\mathcal{T}_\Theta$ set to the identity and $\mathbf{\Psi}$ to a spatial wavelet transform (Figure 4.1.b). After the first iteration $\mathbf{\Psi}$ is the concatenation of temporal total variation ($TV_t$) and a spatial wavelet transform ($WT_s$), so $\mathbf{\Psi}\mathbf{m} = [\Big[TV_t\mathcal{T}_\Theta\mathbf{m}]^{\mathrm{T}}|[WT_S\mathbf{m}]^{\mathrm{T}}\Big]^{\mathrm{T}}$

Second, the spatial deformation $\mathcal{T}_\Theta$ is estimated by solving

$$\underset{\Theta}{\text{minimize}} \|\mathcal{T}_\Theta \mathbf{m} - \overline{\mathcal{T}_\Theta \mathbf{m}}\|_2^2 + C(\mathcal{T}_\Theta) \tag{4.2}$$

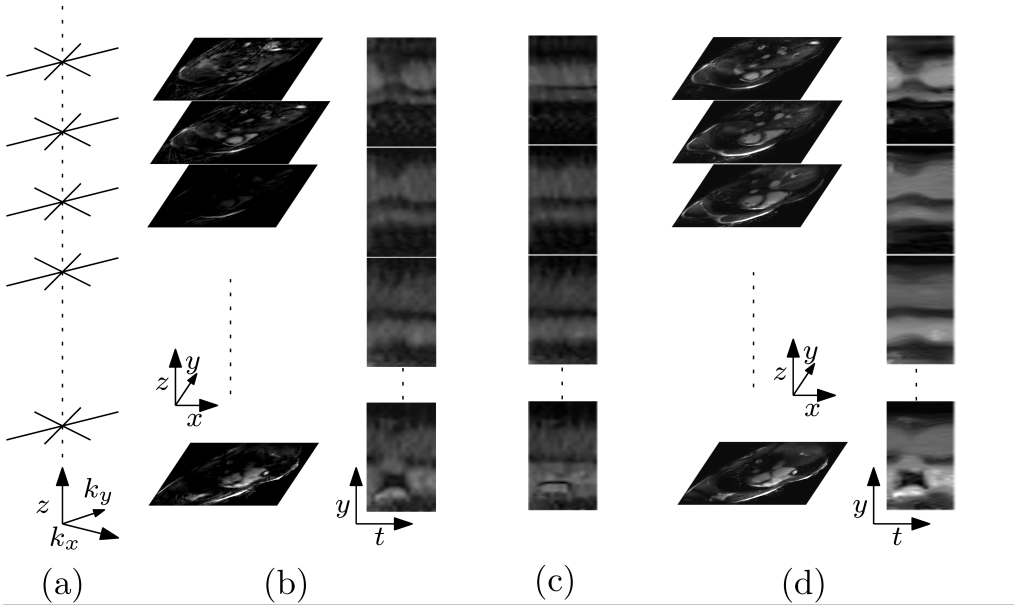


Figure 4.1: Proposed reconstruction algorithm. (a) M2D golden radial acquisition, (b) initial CS reconstruction, (c) groupwise registration and (d) MC-CS reconstruction.

where $\overline{\mathcal{T}_\Theta \mathbf{m}}$ represents the temporal average of the deformed sequence and $C(\mathcal{T}_\Theta)$ is a spatio–temporal regularization cost function (Metz et al., 2011). When $\mathcal{T}_\Theta$ is applied a quasi-static sequence with high temporal sparsity results, as can be observed in the temporal profiles in Figure 4.1.c.

## 4.3 Methods

A healthy male volunteer was scanned with a 32-element cardiac coil and a golden radial trajectory on a 1.5T Philips scanner. Other relevant scan parameters include: b-SSFP sequence, TR/TE/$\alpha$=2.9ms/1.44ms/60°, FOV = 320x320mm$^2$, spatial resolution = 2x2mm$^2$, slice thickness = 8mm with no gap between 12 slices. 256 radial profiles were acquired per slice during a single cardiac cycle with ECG triggering. 16 cardiac phases were retrospectively reconstructed (16 profiles per phase), leading to a temporal resolution of 46.4ms. A conventional fully sampled, Cartesian, multi BH scan was performed with similar acquisition parameters for comparison. Total data acquisition time was 11.1 s in the proposed single BH scan and 1 min 42 s in the Cartesian one (without considering resting intervals between breath holds). Sensitivity maps were estimated from a separate scan. For comparison, data was also reconstructed using k-t

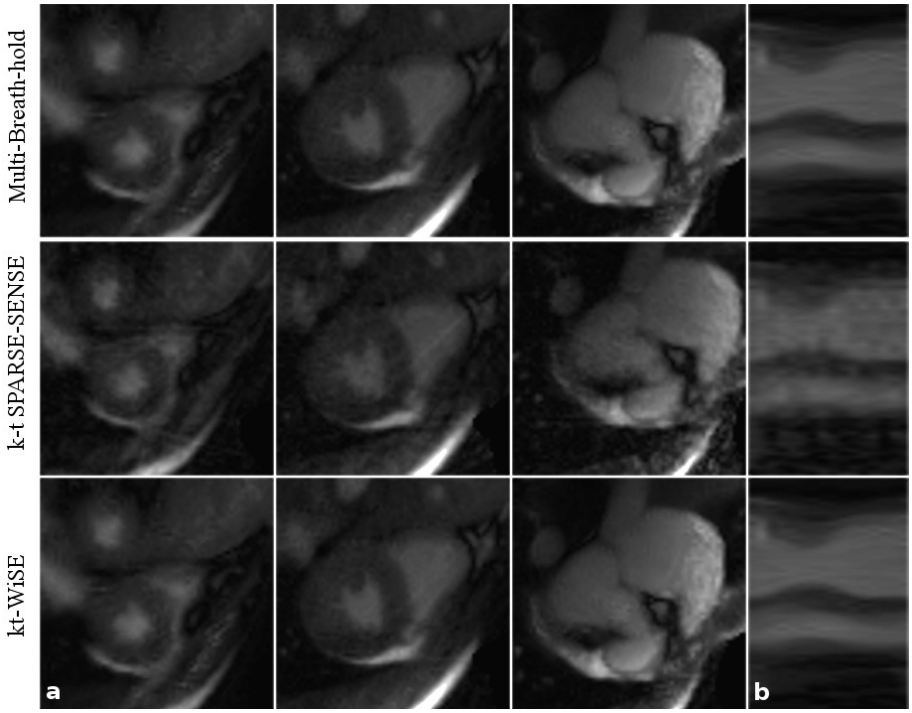


Figure 4.2: (a) Apical, med-ventricular and basal slices at systole for fully-sampled (top), k-t SPARSE-SENSE (middle), and kt-WiSE (bottom) reconstructions. (b) Temporal profiles of a mid-ventricular slice for the three reconstruction methods.

SPARSE-SENSE (Otazo et al., 2010) with temporal Fourier transform as sparse domain.

## 4.4 Results and conclusions

Apical, medial and basal slices at end systole obtained from the multi BH Cartesian data and from the single breath hold golden radial data reconstructed with k-t SPARSE-SENSE and kt-WiSE are shown in Figure 4.2.a. Sharper edges and better overall quality can be appreciated in the last case. Figure 4.2.b shows temporal profiles of the medial slice. Better temporal fidelity can be perceived for the kt-WiSE image.

CHAPTER

# FIVE

# WHOLE-HEART SINGLE BREATH-HOLD CARDIAC CINE: A ROBUST MOTION-COMPENSATED COMPRESSED SENSING RECONSTRUCTION METHOD

Javier Royuela-del-Val[1], Muhammad Usman[2], Lucilio Cordero-Grande[2], Federico Simmross-Wattenberg[1], Marcos Martín-Fernández[1], Claudia Prieto[2] and Carlos Alberola-López[1].
Whole-heart single breath-hold cardiac cine: A robust motion-compensated compressed sensing reconstruction method. Proceedings of the 19th International Conference on Medical Image Computing & Computer Assisted Intervention. 1st International Workshop on Reconstruction and Analysis of Moving Body Organs (MICCAI/RAMBO 2016), October 17th, Athens, Greece.

[1] Laboratorio de Procesado de Imagen, Universidad de Valladolid, Valladolid, Spain.

[2] Division of Imaging Sciences and Biomedical Engineering, Centre for the Developing Brain, King's College London, London, UK.

**Abstract**

In this paper we propose a methodology to achieve single breath-hold whole-heart cine MRI with a temporal resolution of ∼46ms and a spatial resolution of $2\times2mm^2$ out of a previously described method (JW-tTV) for single slice reconstruction.Its feasibility is tested by itself and in comparison with another state-of-the-art reconstruction method (MASTeR);

both methods are adapted to Golden Radial k-space trajectories. From a formal viewpoint, we make use of a realistic numerical phantom to have a ground truth of deformation fields so that the methods performances against noise can be quantified and the sparsity regularization parameter involved in the reconstructions can be fixed according to the signal to noise ratio. Phantom results show that the adapted JW-tTV method is more robust against noise and provides more precise motion estimations and better reconstructions than MASTeR. Both methods are then applied to the reconstruction of 12-14 short axis slices covering the whole heart on eight volunteers. Finer details are better preserved with JW-tTV. Ventricle volumes and ejection fractions were computed from the volunteers data and preliminary results show agreement with conventional multiple breath-hold Cartesian acquisitions.

## 5.1 Introduction

Cine MRI has become the preferred technique for the noninvasive study of the ventricular volumes and cardiac function (Bogaert et al., 2012), where a stack of short axis slices covering the ventricles are acquired during several breath-holds (BH), typically one per slice, to avoid respiratory motion artifacts. This approach leads to long scan durations, misalignments between the slices acquired at slightly different BH positions and requires patient cooperation, a need that may be hindered by the patient pathology degree. The development of a technique able to cover the whole heart in a single BH would significantly palliate these shortcomings. However, such a technique would involve the application of very high acceleration factors given the short time available for data acquisition.

Compressed sensing (CS) (Donoho, 2006) based reconstruction methods have been developed and successfully applied to multi-slice 2D SSFP sequences. In (Feng et al., 2013), a free-breathing approach is presented in which a pseudo-random, eight-fold undersampling acquisition pattern in the Cartesian k-t space is applied. In (Vincenti et al., 2014) a closely related approach is applied to acquire four short axis and three long axis views of the heart in a single BH. shape model is fitted to estimate the volume of the left ventricle (LV).

In the mentioned methods, the application of a Cartesian acquisition scheme leads to limited spatio-temporal resolution and, in some cases, aliasing problems

along the phase-encoding direction (Vincenti et al., 2014). Moreover, the targeted temporal resolution must be strictly defined before the examination, as it would determine the acquisition pattern (roughly speaking, the temporal resolution will determine how often the center of the k-space is sampled). These limitations can be overcome by the application of a Golden radial (GR) trajectory in k-space (Winkelmann et al., 2007). Since no phase-encoding is used, there is no interference from objects outside the field of view and the wisely selected golden-angle step allows to continuously acquire data regardless of the final temporal resolution of the reconstructed images, resulting in a more versatile and simpler procedure.

Recently, motion estimation (ME) and motion compensation (MC) techniques have been introduced in CS methods in order to minimize the degradation of CS reconstructions due to inter frame motion (Asif et al., 2013; Lingala et al., 2015; Royuela-del Val et al., 2017a). In CS with ME/MC, motion is jointly estimated from the reconstructed images themselves which, in turn, will be affected by both remaining undersampling artifacts and noise. The degree to which these errors in the images affect the estimated motion will determine the final quality of the reconstructions. Therefore, the application of a robust ME method turns out crucial (Royuela-del Val et al., 2016a). However, the lack of a noise-free ground-truth for the images and the deformation fields hinders the performance analysis of the ME techniques and the CS reconstruction methods against noise in real situations. Signal to noise ratio (SNR) is also determinant in the choice of the regularization parameters involved in CS reconstruction (Doneva et al., 2012; Feng et al., 2013). A common procedure is to sweep the parameter space and select those parameters that provide the best reconstruction according to an expert criterion. This approach has clear limitations in real-world applications.

In this work we achieve higher acceleration factors with respect to recently published methods so whole-heart multi-slice cine single BH coverage is achieved. This is done by extending the Jacobian weighted temporal total variation (JW-tTV) (Royuela-del Val et al., 2017a) method, originally applied to the reconstruction of single-slice Cartesian acquired data, to use a GR acquisition scheme. This allows us to reach a x16 acceleration factor (with respect to a fully sampled Cartesian acquisition) that had remained unachieved so far. This proposal is compared with MASTeR (Asif et al., 2013), a related method which differs mainly in the ME technique used and which we have also extended to use GR. We show that quantitative cardiac function indicators, namely end diastolic (ED),

end systolic (ES) and EF values calculated from the images reconstructed with the proposed method are in accordance with those obtained from a gold standard multi-BH Cartesian acquisition.

In addition, and as a preliminary step, we analyze the effect of noise on the acquired data in two aspects. First, in the selection of the optimal value for the regularization parameter involved in the CS reconstruction in order to obtain a empirical rule to select it. Second, in the errors induced in the estimated motion fields and in the quality of the final images. To this end, we use the numerical phantom XCAT (Segars et al., 2010; Wissmann et al., 2014) to generate realistic ground truth deformation fields and synthetic k-space data affected by different levels of noise. The resulting extensions of both compared methods (JW-tTV-GR and MASTeR-GR) are tested.

## 5.2 Methods

### CS reconstruction of undersampled dynamic MRI with ME/MC

In CS with ME/MC, the reconstruction of an MRI image $\mathbf{m}$ from the acquired undersampled k-space data $\mathbf{y}$ can be formulated as (Royuela-del Val et al., 2016a)

$$\underset{\mathbf{m}}{\text{minimize}} \frac{1}{2} \parallel \mathbf{y} - \mathbf{E}\mathbf{m} \parallel_{\ell_2}^2 + \lambda \parallel \mathbf{\Phi}\mathcal{T}_{\Theta}\mathbf{m} \parallel_{\ell_1} \tag{5.1}$$

where $\mathbf{E}$ is the encoding operator that models the acquisition process. In Cartesian acquisitions, $\mathbf{E}$ comprises the multiplication of the image $\mathbf{m}$ by the coils sensitivity profiles and the application of the regular FFT followed by the undersampling of the data with the used sampling pattern. In cine cardiac MRI, the sparsifying transform $\mathbf{\Phi}$ is typically chosen to be the temporal Fourier transform or the temporal total variation, in order to exploit the temporal redundancy between different cardiac phases. However, inter-frame motion will affect the redundancy of the signal along time reducing, reducing its sparsity level. The MC operator $\mathcal{T}_{\Theta}$ comprises a set of spatial deformations, governed by the set of parameters $\Theta$, that deform each temporal instant in the dynamic image $\mathbf{m}$ to a common reference motion state. This way, the sparsity of the the resulting motion compensated sequence along the temporal dimension is restored and the quality of the reconstruction improved, consequently. The parameter $\lambda$, referred to as regularization parameter in the introduction section, establishes a trade off between data consistency and the sparsity of the solution.

Since the motion in $\mathbf{m}$ is not known beforehand, a regular CS reconstruction is performed as a first step, which is equivalent to solve Eq. (5.1), with $\mathcal{T}_\Theta$ set to the identity. Then, a ME step follows and $\mathcal{T}_\Theta$ is estimated. The ME technique consists on a groupwise registration method based on a B-spline deformation model (Rueckert et al., 1999), controlled by the set of control points $\Theta$, and a simple groupwise registration metric based on the variance of the intensity along time. Those control points that minimize the value of the registration metric are found by solving the following optimization problem:

$$\underset{\Theta}{\text{minimize}} \left\| \sum_{n=1}^{N} \left( \mathcal{T}_{\Theta,n}\mathbf{m}_n - \frac{1}{N} \sum_{k=1}^{N} \mathcal{T}_{\Theta,k}\mathbf{m}_k \right) \right\|^2 + R(\Theta) \tag{5.2}$$

where $R(\Theta)$ stands for an additional regularization term given by the second spatio-temporal derivatives of the motion fields that encourages smoothness of the estimated spatial deformations (Royuela-del Val et al., 2016a). Eq. (5.2) is solved by means of a non linear conjugate gradient algorithm. Once $\mathcal{T}_\Theta$ has been obtained, CS with ME/MC is performed by solving Eq. (5.1). The NESTA optimization algorithm (Becker et al., 2011) is used to this end. Once Eq. (5.1) has been solved, and iterative procedure can be followed by alternating the ME/MC and the image reconstruction steps to obtain successively refined motion fields and images. In this work, the number of ME iterations has been set to three.

Finally, in JW-tTV a modification is introduced in the computation of the sparsity regularization term. The $\ell_1$ term in Eq. (5.1) is substituted by a motion-based sparsity promoting metric given by

$$\|m\|_{\mathcal{T}_\Theta} = \left\| \sum_{n=1}^{N} |\mathcal{T}_{\Theta,n+1}\mathbf{m}_{n+1} - \mathcal{T}_{\Theta,n}\mathbf{m}_n| \, \mathcal{J}_{n+1/2} \right\|_{\ell_1} \tag{5.3}$$

where $\mathcal{J}_{n+1/2}$ stands for the Jacobian of the deformation, averaged between instants $n$ and $n+1$. The Jacobian is introduced in order to weigh the contributions of the temporal differences in Eq. (5.3) according to their corresponding spatial extent in the original sequence (before MC), instead of in the motion compensated one. Therefore, the following reconstruction problem results:

$$\underset{\mathbf{m}}{\text{minimize}} \, \frac{1}{2} \, \| \, \mathbf{y} - \mathbf{E}\mathbf{m} \, \|_{\ell_2}^2 + \lambda \, \|\mathbf{m}\|_{\mathcal{T}_\Theta} \tag{5.4}$$

### Adaptation to Golden Radial acquisition

As stated in the introduction, in this work we have adapted the previously proposed JW-tTV method to work with GR trajectories in k-space in order to

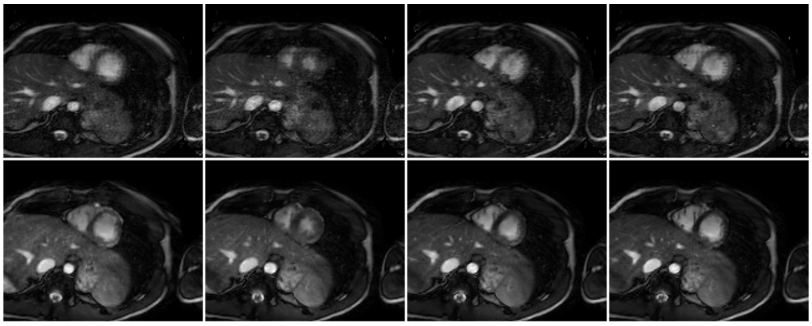

Figure 5.1: Comparison of a Cartesian (top) and GR (bottom) reconstruction of a medial SA slice of the heart for an equivalent acceleration factor of 16 at different cardiac phases (left to right).

overcome the limitations derived from Cartesian acquisitions. In the GR scheme (Winkelmann et al., 2007), radial profiles are continuously acquired with an angular separation given by the golden angle ($\sim 111.24°$).

In order to work with non Cartesian k-space data, the encoding operator in Eq. (5.4) is modified by substituting the regular FFT and the undersampling pattern by the calculation of a non–uniform FFT (NUFFT). To implement the NUFFT, we resort to the well established gridding algorithm (Beatty et al., 2005). In this algorithm, the k-space data is convolved with a finite kernel, sampled onto a Cartesian grid, converted to image domain performing a regular FFT and multiplied by a deapodization function to compensate for the effect of the convolution kernel in the frequency domain.

Even if efficient implementations exist, given the need of gridding operations the computational cost of the NUFFT is significantly higher than the Cartesian FFT. However, the benefits resumed in the introduction justify its application. In order to briefly compare the results obtained with the proposed GR method and the equivalent Cartesian counterpart, in Figure 5.1 the reconstruction of a single SA view of the heart of one volunteer is shown. The GR pattern covers the k-space more efficiently leading to better reconstructions, specially for the high acceleration factors involved in the single BH application.

### Comparison with MASTeR

The proposed method is compared in the results section with MASTeR (Asif et al., 2013) which mainly differs from JW-tTV in the method used to estimate

the motion in the image. In MASTeR, motion is estimated sequentially between each pair of consecutive frames to define a set of operators that predict each frame $\mathbf{m}_i$ out of its leading and trailing frames:

$$\begin{aligned} \mathbf{m}_i &= \mathcal{F}_{i-1}\mathbf{m}_{i-1} + \mathbf{f}_i \\ \mathbf{m}_i &= \mathcal{B}_{i+1}\mathbf{m}_{i+1} + \mathbf{b}_i \end{aligned} \tag{5.5}$$

where $\mathcal{F}_{i-1}$ and $\mathcal{B}_{i+1}$ denote the forward and backward MC operators. Residuals $\mathbf{f}_i$ and $\mathbf{b}_i$ are assumed to be sparse and are used as sparsity term:

$$\underset{\mathbf{m}}{\text{minimize}}\ \frac{1}{2} \parallel \mathbf{y} - \mathbf{E}\mathbf{m} \parallel_{\ell_2}^2 + \alpha \parallel \mathbf{f} \parallel_{\ell_1} + \beta \parallel \mathbf{b} \parallel_{\ell_1} \tag{5.6}$$

where $\mathbf{f}$ and $\mathbf{b}$ are the concatenation of the residuals for all the cardiac phases. In our implementation, we choose $\alpha = \beta = 0.5\lambda$, since there is no apparent reason to favor any of the two terms. A method based on complex wavelets is used for estimating inter-frame motion.

### Numerical phantom for heart motion and MR images simulation

XCAT (Segars et al., 2010) was used to obtain a ground truth both for reconstructed images and for the motion deformation fields. We modified MRXCAT (Wissmann et al., 2014) to simulate the k-space data with a desired SNR of a medial short axis slice with the following main parameters: b-SSFP sequence, TR/TE/flip angle = 3ms/1.5ms/60°, in-plane resolution of 1x1mm$^2$, field of view = 256x256mm$^2$. 320 radial profiles were acquired and grouped into 20 cardiac phases (16 profiles per phase). 8 virtual coils were simulated. MASTeR-GR and JW-tTV-GR were used for reconstruction and the motion fields estimated by each of those methods were stored for posterior analysis. A dense sweep on the regularization parameter $\lambda$ was performed for each SNR in order to find its optimal value in order to get both the maximum signal to error ratio (SER) and the best structure similarity index (SSIM) (Wang et al., 2004), calculated using the noise-free phantom image as the reference.

### In-vivo experiments: single BH whole-heart acquisitions

Eight healthy volunteers were scanned with a 32-element cardiac coil in two 1.5T Philips scanners (four each). Relevant scan parameters include: b-SSFP sequence, TR/TE/flip angle = 2.9ms/1.44ms/60°, field of view = 320x320mm$^2$,

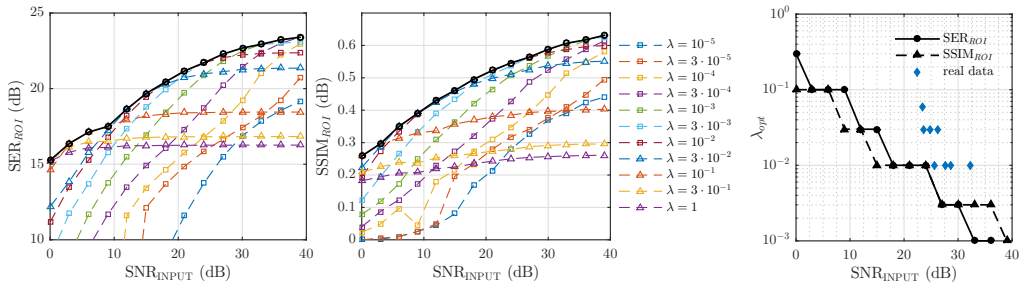


Figure 5.2: SER (left) and SSIM index (center) obtained for each combination of $\lambda$ in Eq. (5.4) and SNR value are plotted –dashed lines–. The envelope –continuous line– marks the optimal value of $\lambda$ according to each metric for each SNR value and is plotted separately (right). The value of $\lambda$ used to reconstruct the real data from volunteers is indicated in blue.

spatial resolution = 2x2mm$^2$, slice thickness = 8mm with no gap between slices. For each slice (12 to 14 were acquired, depending on volunteers heart size) between 216 and 272 radial profiles with 320 frequency encoding samples were acquired during a single cardiac cycle with ECG triggering. 13-16 cardiac phases were retrospectively reconstructed with a fixed temporal resolution of 46.4ms (16 profiles per frame). A fully sampled, Cartesian, multi BH scan was performed with similar parameters for comparison. Breath-hold duration ranged 9 to 15 seconds. Sensitivity maps were estimated from a separate scan.

All the reconstructions were run off line on a server with two Intel Xeon E5-2695 v3 CPU's @ 2.30 GHz and 64 GB of RAM using MATLAB (R2015a, The MathWorks, Natick, MA). At the current implementation, both methods are applied to each slice independently from the others, what makes parallelization of the reconstruction straight forward.

## 5.3 Results

Figure 5.2 shows the SER and SSIM values for the JW-tTV reconstruction of the phantom data for a range of SNR and $\lambda$ values. As the SNR diminishes, the optimal value of $\lambda$ increases steadily. Therefore, higher level of sparse regularization results in better reconstructed images, as predicted by CS theory (Donoho, 2006). Only small differences in optimal $\lambda$ appear depending on the quality metric used. These results were used as a reference to select $\lambda$ in the reconstruction of in vivo data, where the SNR was estimated from the fully sampled, Cartesian images taking a background region as a reference for noise level.

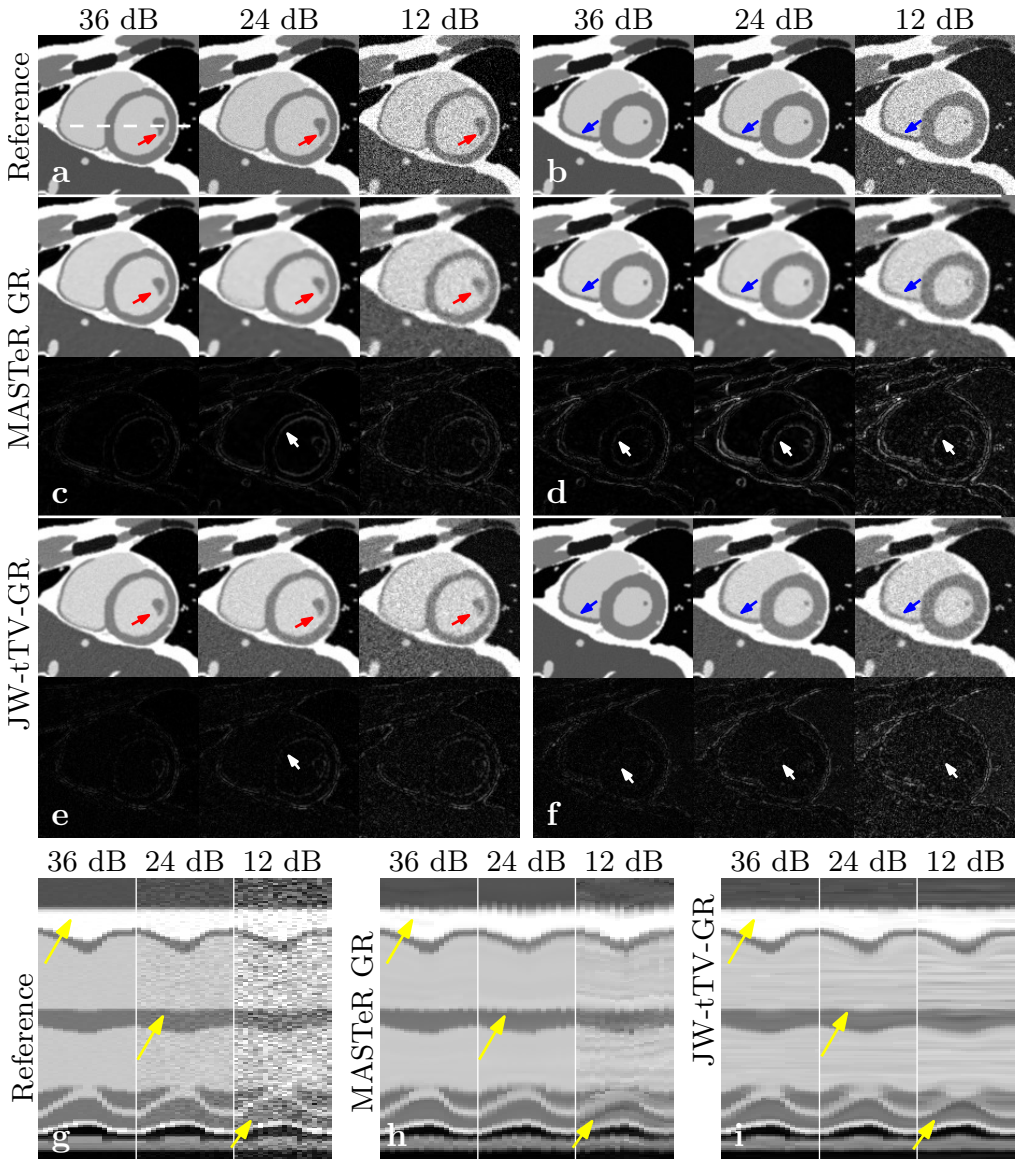


Figure 5.3: Phantom reconstructions for different SNR values. Reference noisy images reconstructed from fully sampled Cartesian data (a, b) and from Golden Radial undersampled data (16 spokes per frame) with MASTeR-GR (c,d) and JW-tTV-GR (e,f) at systole and diastole, respectively. Error images are shown scaled by a factor of 2. Temporal evolution of the dashed line in (a) for the corresponding reconstructions (g, h, i). In JW-tTV-GR reconstructions thin details such as borders of the papillary muscle (red arrows) or the wall of the right ventricle are better preserved and present sharper edges than MASTeR-GR. Errors in MASTeR-GR are mainly concentrated in the edges of the structures, due to edge blurring and motion errors (white arrows), while JW-tTV-GR presents noisy errors due to low SNR. In the temporal evolutions yellow arrows indicate areas where MASTeR-GR presents some erratic motion in the heart even for high SNR values, while in JW-tTV-GR this effect is much less present.

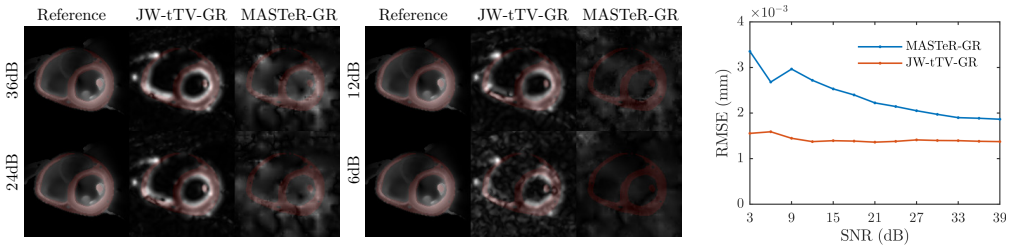


Figure 5.4: Absolute value of motion fields estimated with MASTeR and JW-tTV in the 14th phase of the cardiac cycle out of 20, corresponding with large inter frame motion after end-systole for different SNR values (left and center). Phantom ground truth is shown at the left of each image. Red mask represents left and right myocardium. Plot of the RMSE of the motion fields calculated over the myocardium mask for a range of SNR values (right). Larger errors and faster degradation for low SNR can be observed for MASTeR, while JW-tTV shows to be almost immune to the presence of noise.

After revision by an experienced observer, the final values of $\lambda$ were increased in order to maximize the subjective quality perception.

The reconstructions obtained for a selection of the SNR values simulated with the numerical phantom are summarized in Figure 5.3. Sharper edges are recovered with JW-tTV than with MASTeR, specially for lower SNR values. More interestingly, MASTeR reconstructions show an erratic motion in the temporal profiles than can be appreciated even for high SNR values. The presence of erratic motion grows as the SNR decreases. These results agree with the motion fields obtained with both ME/MC CS based methods, analyzed in Figure 5.4. For the whole range of SNR values simulated, the groupwise ME/MC technique employed in JW-tTV results in more precise estimations. The differences with the phantom ground-truth, measured as the root mean squared error on a mask over the myocardium, remain almost constant even for the lowest SNR values, while higher errors and faster degradation can be observed for MASTeR.

Figure 5.5 shows the results obtained from in-vivo data for two of the eight volunteers acquired. Sharper edges and finer details are better preserved with JW-tTV, while contrast between myocardium and blood pool is preserved. For each volunteer, ventricular volumes at end systole (ESV), end diastole (EDV) and ejection fraction (EF) were computed from the short axis slices using Simpson's rule and manual segmentation on a dedicated software for the three reconstructions. Functional parameters computed from fully sampled Cartesian reconstructions were used as reference values. Bland-Altman plots of the results are shown in Figure 5.6. The mean and standard deviation of the differences be-

| Method | ESV difference (ml) | EDV difference (ml) | EF difference (%) |
|---|---|---|---|
| MASTeR-GR | $1.65 \pm 3.62$ | $-4.23 \pm 2.62$ | $-2.63 \pm 2.61$ |
| JW-tTV-GR | $-0.28 \pm 3.06$ | $-2.98 \pm 5.00$ | $-0.73 \pm 2.19$ |

Table 5.1: Left ventricular volumes and EF differences between accelerated and reference scan. Mean ± standard deviations are shown.

tween the functional parameters computed with each method and the reference scan are summarized in Table 5.1. JW-tTV results in lower mean ESV, EDV and EF differences and lower standard deviation for ESV and EF than MASTeR reconstructions.

## 5.4 Discussion and conclusion

In this paper we have proposed a new reconstruction method based on the adaptation of a previously described ME/MC CS based method to comply with Golden Radial, multi-slice acquisitions. We have achieved an undersampling factor that allows us to cover the whole-heart (12-14 slices) with a temporal resolution of 46.4 ms, 13-16 cardiac phases with 16 profiles per frame, in a single BH of 10-13 seconds.

For a given undersampling factor, determined by the single BH application that we pursue, the experiments on the numerical phantom allowed us to study the effect of noise on the reconstructions and on the selection of the reconstruction parameters. How to choose the weight of the sparsity regularization in CS reconstructions is still an open problem of the technique. In this work we try to establish, for this specific application, a choice rule based on the SNR of the data. On real practice, this SNR can be easily obtained by the MRI scanner with a short noise acquisition at the beginning of the examination. However, after visual examination, the final value of the reconstruction parameter had to be increased to get better results. Two aspects could explain this fact: on the one hand, the metrics used (SER and SSIM) are known to be limited when used to quantify image quality perception; on the other, different systematic errors in the real data reconstruction that are absent on the simulated data could affect the results (e.g. errors in the sensitivity maps and in the k-space trajectories). Consequently, a higher regularization term could partially mitigate the effect of the systematic errors mentioned.

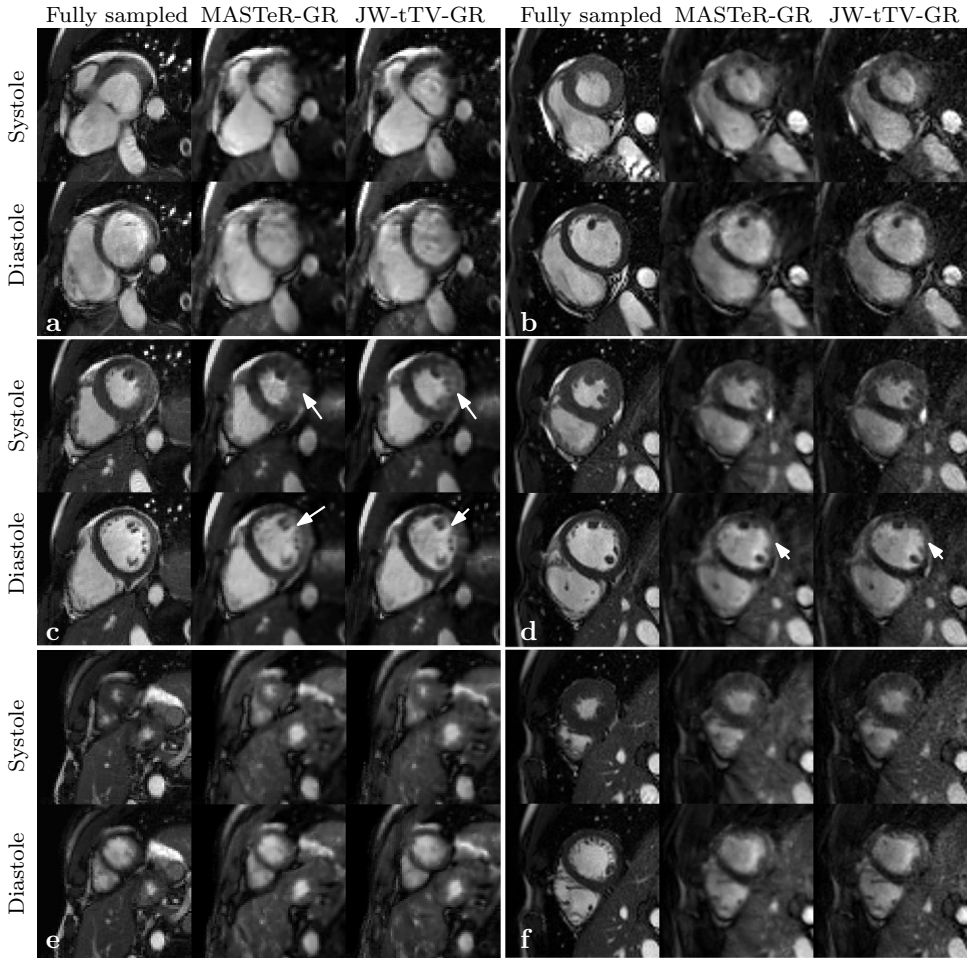


Figure 5.5: Cartesian fully sampled, MASTeR and JW-tTV reconstructions of the data from two of the volunteers acquired. Basal (a,b), medial (c,d) and apical (e,f) short axis views are shown both at systole and diastole. White arrows indicate areas where thinner details are recovered with JW-tTV therefore permitting better delineation of the papillary muscles at systole.

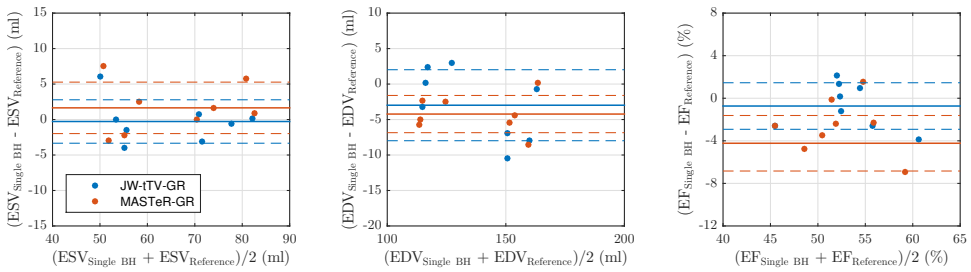


Figure 5.6: Bland-Altman plots of the ESV (left), EDV (center) and EF (right) calculated from the fully sampled data (reference values) and from the accelerated single BH acquisition with MASTeR and JW-tTV.

Simulated and in vivo results show that better ME and more detailed reconstructions are obtained with the adapted JW-tTV than with MASTeR. For the latter, some erratic motion is observed in the reconstructions that could be explained by the lower performance of the ME procedure in the whole range of SNR considered. These results illustrate how ME errors can propagate to the final solution and the importance of using a robust ME technique.

Accordingly with this observation, the erratic motion in MASTeR reconstructions seems to affect the LV functional parameters calculated, introducing a larger mean difference in ESV, EDV and EF, since it can introduce artificial volume variations in the images and makes more difficult to identify systolic and diastolic cardiac phases. It is worth mentioning the higher standard deviation in the calculation of the EDV with JW-tTW. As Figure 5.6 shows, in MASTeR reconstructions EDV values are systematically underestimated. With JW-tTV that bias does not occur, but underestimation takes place in volunteers with larger EDV. This fact increases the standard deviation of EDV differences in JW-tTV. However, the mean difference remains lower (in absolute value) than the one calculated from MASTeR reconstructions.

For the current MATLAB implementation, the reconstruction times for the single BH acquisitions lasted 12.5 min per slice with all the slices being reconstructed in parallel independently, what clearly limits the practical application of the proposed method. However, an initial reconstruction is provided in approximately 2 min that can be useful to check the correct planning of the acquisition. The introduction of coil compression techniques (Buehrer et al., 2007) and the development of a high performance implementation of the algorithm on graphics processing units could significantly reduce these reconstruction times.

Although the number of volunteers is reduced, reconstructed images and functional values computed from the highly accelerated data show preliminary evidence of the feasibility of the extended JW-tTV method to realize a whole heart cine examination in a single BH of short duration. For comparison, the acquisition time in the conventional Cartesian acquisition was between 1.7 and 2.2 minutes, without considering resting intervals between breath holds. This reduction in scan time could drastically impact on patient comfort and medical resources exploitation. However, further studies including intra and inter observer variability and both healthy volunteers and patients with heart disease are needed to fully validate these results.

CHAPTER

# SIX

# MULTIRESOLUTION RECONSTRUCTION OF REAL-TIME MRI WITH MOTION COMPENSATED COMPRESSED SENSING: APPLICATION TO 2D FREE-BREATHING CARDIAC MRI

**Published as:**

Javier Royuela-del-Val[1], Muhammad Usman[2], Lucilio Cordero-Grande[2], Federico Simmross-Wattenberg[1], Marcos Martín-Fernández[1], Claudia Prieto[2] and Carlos Alberola-López[1]. Multiresolution Reconstruction of Real-Time MRI with Motion Compensated Compressed Sensing: Application to 2D Free-Breathing Cardiac MRI. 13th IEEE International Symposium on Biomedical Imaging: From Nano to Macro (ISBI 2016). Prague, CZ.

[1] Laboratorio de Procesado de Imagen, Universidad de Valladolid, Valladolid, Spain.

[2] Division of Imaging Sciences and Biomedical Engineering, Centre for the Developing Brain, King's College London, London, UK.

**Abstract**

Real-time MRI is a novel noninvasive imaging technique that allows the visualization of physiological processes with both good spatial and temporal resolutions. However, the reconstruction of images from highly

undersampled data, needed to perform real-time imaging, remains challenging. Recently, the combination of Compressed Sensing theory with motion compensation techniques has shown to achieve better results than previous methods. In this work we describe a real-time MRI algorithm based on the acquisition of the k-space data following a Golden Radial trajectory, Compressed Sensing reconstruction and a groupwise temporal registration algorithm for the estimation and compensation of the motion in the image, all this embedded within a temporal multiresolution scheme. We have applied the proposed method to the reconstruction of free-breathing acquisition of short axis views of the heart, achieving a temporal resolution of 25ms, corresponding to an acceleration factor of 28 with respect to fully sampled Cartesian acquisitions.

**Keywords:** Magnetic resonance imaging (MRI), Compressive sensing & sampling, Image reconstruction – analytical & iterative methods

## 6.1 Introduction

The recent development of signal analysis based acceleration techniques in dynamic MRI has significantly pushed the achievable acceleration factors to unforeseen levels. Recently, the combination of Compressed Sensing (CS) theory (Donoho, 2006) with motion estimation (ME) and motion compensation (MC) techniques has been successfully applied to CS reconstruction of dynamic MRI based on the assumption that sparser representations of the signal can be obtained if some knowledge of the motion in the image is incorporated during the reconstruction Prieto et al. (2015), (Royuela-del Val et al., 2016a).

In real time (RT) MRI, the high acceleration factors needed to achieve the desired spatio-temporal resolution make the reconstruction problem highly ill-conditioned, becoming very sensitive to noise in the data and model inconsistencies. Moreover, ME/MC techniques lack the true dynamic image to estimate the motion from. A common approach is to perform the ME step on an initial reconstruction without MC which, however, may be corrupted by the undersampling artifacts that cannot be corrected in the first step. These artifacts, in turn, would hinder the estimation of the true motion in the dynamic image. In a previous work by Royuela-del Val et al. (2016a), a groupwise (GW) temporal registration procedure, which showed to be more robust to artifacts than its

pairwise counterparts, was proposed for ME/MC reconstruction of breath-hold cine acquisitions. However, the acceleration factors achieved could not enable its direct application to free-breathing RT imaging, due to the limitations of the Cartesian acquisition employed.

To overcome the previous limitations, in this work we propose a reconstruction algorithm with three key components. First, we adopt the golden-angle radial (GR) trajectory from Winkelmann et al. (2007) for continuous data acquisition in which the angular step between consecutive spokes is given by the Golden Ratio. For a given undersampling factor, GR provides a more efficient coverage of the k-space than a Cartesian scheme. Second, the GR allows to retrospectively set up an arbitrary window length (i.e. temporal resolution), which enables us to introduce a multiresolution approach in which finer temporal resolution reconstructions are obtained iteratively from coarser ones. Third, for ME/MC we resort to the GW registration method employed by Royuela-del Val et al. (2016a) to iteratively obtain MEs from coarser to finer temporal resolutions, avoiding the need of estimating the motion directly from highly undersampled data.

The proposed method is applied to the reconstruction of free-breathing, 2D short axis views of the heart of three healthy volunteers. Results are compared with those obtained with the non–linear inversion (NLINV) method from Uecker et al. (2010), in which both the images and coil sensitivity maps are jointly estimated. In NLINV, temporal regularization is introduced by enforcing the similarity between consecutive frames in a sequential way.

## 6.2 Theory

The reconstruction of accelerated MRI data can be generally formulated as solving a linear inversion problem $\mathbf{y} = \mathbf{Em}$, where $\mathbf{y}$ stands for the acquired multicoil k-t space data, $\mathbf{m}$ represents the sequence of images to be reconstructed and the encoding operator $\mathbf{E}$ comprises the multiplication by the coils sensitivity maps and the frame-by-frame undersampled spatial Fourier transform. Under the MC-CS framework (Lingala et al., 2015) both the image and the motion information are jointly reconstructed. In our proposal, we split the problem in two subproblems (reconstruction and ME/MC) and alternate between both following a multiresolution scheme.

### 6.2.1 Motion Compensated Reconstruction

The reconstruction problem, assuming motion is known beforehand, is formulated as:

$$\min_{\mathbf{m}} \left\{ \| \mathbf{y} - \mathbf{E}\mathbf{m} \|_2^2 + \lambda \| \mathbf{\Psi}\mathcal{T}_\Theta \mathbf{m} \|_{\ell_1} \right\} \tag{6.1}$$

with $\mathbf{\Psi}$ a spatio-temporal transform and $\lambda$ a trade off parameter between data fidelity and sparsity promotion. $\mathcal{T}_\Theta$ is a warping operator governed by the set of parameters $\Theta$ designed to compensate the motion in the image.

### 6.2.2 Groupwise temporal registration for ME/MC

During the ME/MC step a GW dissimilarity metric that provides a unique global measure of the differences between the images comprised within the sequence is minimized. In the current implementation, a simple sum of squared differences (SSD) metric (Metz et al., 2011) is used:

$$\min_{\mathbf{\Theta}} \left\{ \frac{1}{2} \| \mathcal{T}_\Theta \mathbf{m} - \overline{\mathcal{T}_\Theta \mathbf{m}} \|_2^2 + C(\mathcal{T}_\Theta) \right\}. \tag{6.2}$$

where $\overline{\mathcal{T}_\Theta \mathbf{m}}$ stands for the temporal average of the registered sequence. $C(\mathcal{T}_\Theta)$ is a regularization term related to the elastic energy of a bending plate (Rueckert et al., 1999) which penalizes non–smooth deformations. As it can be derived from this expression, there is no need for a fixed reference frame. The SSD metric relies on the assumption that the intensity of each pixel is preserved along time. Other metrics can be incorporated for different imaging modalities where such a condition is not met (Cordero-Grande et al., 2013).

The deformation model used in the GW registration algorithm is based on a non-rigid 2D+t free form deformations (FFD) with cubic B-splines, which has been widely used in practice and has shown to be flexible enough to describe the motion and deformation of anatomical structures (Rueckert et al., 1999). Eq. (6.2) is solved with a nonlinear conjugate gradient method.

### 6.2.3 Multiresolution reconstruction of Real-Time MRI

As discussed in the introduction, a major difficulty is to obtain both good initial reconstructions and accurate ME from highly undersampled data. To this end, we propose a multiresolution scheme (see Fig. 6.1) in which coarser reconstructions serve as initialization of the finer ones. An initial, low temporal resolution

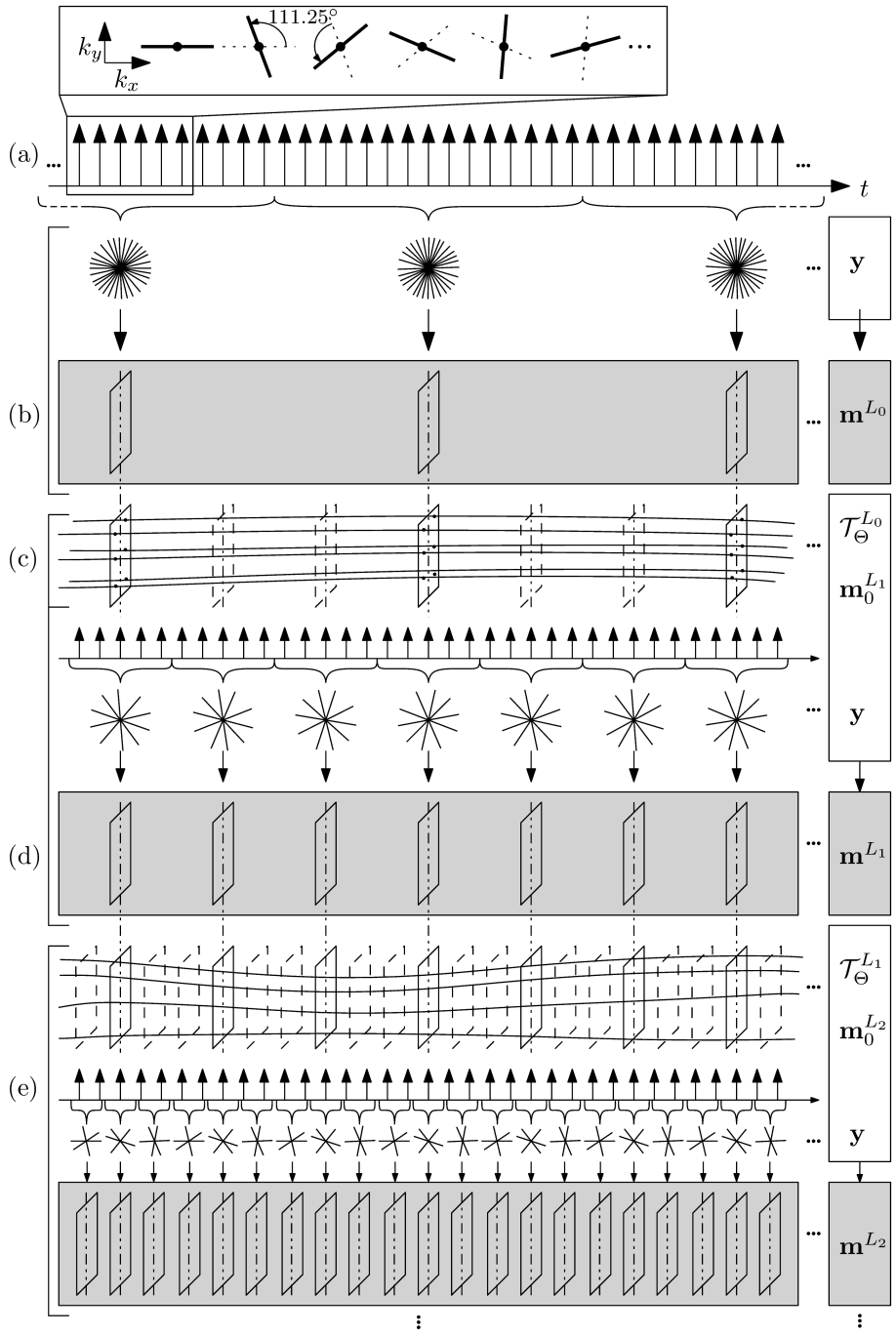


Figure 6.1: Proposed temporal multiresolution scheme. (a) Continuous data acquisition. (b) Initial low temporal resolution reconstruction. (c) Groupwise motion estimation and interpolation of intermediate frames to initialize the next level. (d) Motion compensated CS reconstruction. (e) Steps (c) and (d) are repeated until the target resolution level is reached.

sequence is obtained by a regular CS reconstruction equivalent to solving Eq. 6.1 with $\mathcal{T}_\Theta$ set to the identity. Since no motion information is available at this point, $\boldsymbol{\Psi}$ is set to a spatial wavelet transform. For the next levels temporal total variation is used. At each level, the method alternates until convergence between reconstruction (Eq. 6.1) and ME (Eq. 6.2).

In order to provide a good initialization to the next resolution level, frames could be interpolated as the weighted average of the surrounding frames. However, high inter-frame motion is present such straightforward interpolation can lead to corrupted images. To improve the quality of the interpolation, we make use of the motion information in the estimated deformation, as proposed by Cordero-Grande et al. (2012). Following the approach in (Metz et al., 2011), for each new frame to be interpolated at instant $t_j$ we obtain the transformation $\boldsymbol{T}_\Theta^{ij}(\boldsymbol{x}) = \boldsymbol{T}_\Theta(\boldsymbol{T}_\Theta^{-1}(\boldsymbol{x}, t_j), t_i)$ which aligns a (moving) frame at instant $t_i$ to the frame at instant $t_j$ (fixed image). The originally described B-splines registration method can be extended to guarantee the existence of $\boldsymbol{T}_\Theta^{-1}(\boldsymbol{x}, t_j)$ (De Craene et al., 2012). In our current implementation, the spatio-temporal regularization term and proper spacing on the grid of control points favor the invertibility and the inverse transform is therefore found numerically.

## 6.3 Application to 2D free-breathing cardiac MRI

Three healthy volunteers were scanned with a 32-element cardiac coil and a golden radial trajectory on a 1.5T Philips scanner. Other relevant scan parameters include: b-SSFP sequence, TR/TE/$\alpha$ = 2.9ms/1.44ms/60°, FOV = 320x320mm$^2$, spatial resolution = 2x2mm$^2$, slice thickness = 8mm. A single slice was continuously imaged for about 12 seconds.

Images were reconstructed following the scheme in Fig. 6.1 with three resolution levels and 15 and 9 radial spokes per frame used in the last level (135, 45 and 15 spokes per frame in each level for the first case and 81, 27 and 9 in the second). Corresponding final temporal resolutions are 44 and 26 ms. Parameter $\lambda$ was set to 0.1 attending to visual inspection of the results from one dataset and maintained for the other two. NLINV reconstructions were performed on the same data using the code available at http://www.user.gwdg.de/~muecker/realtime.html after griding the data to a Cartesian lattice with a Kaisser-Bessel window of size $L = 6$ and shape parameter $\beta = 13.8551$. The number of Newton iterations was

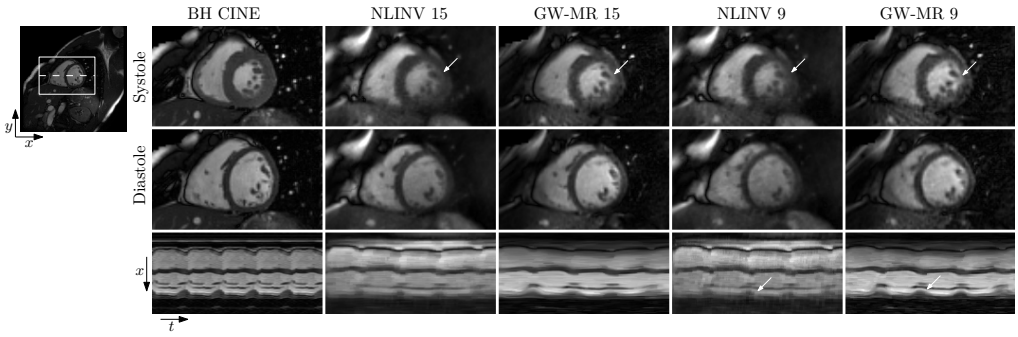


Figure 6.2: Short axis views of the heart of volunteer 1 reconstructed from a regular breath-hold examination (BH CINE) and from real time data with nonlinear inversion (NLINV) and the proposed method (GW-MR). Bottom row shows the temporal evolution of a horizontal line through the center of the left ventricle comprising about 4 seconds (BH CINE periodically replicated for comparison). For the real time reconstructions 15 and 9 spokes per frame were used as indicated. Arrows highlight the better depiction of small details between the papillary muscle and myocardium.

set to 3 and the scale factor for regularization to 0.9 and, as proposed, a median temporal filter of length 5 is applied after reconstruction to remove remaining artifacts (see Ref. (Uecker et al., 2010) for details).

Reconstructions were run off–line on a server with two Intel Xeon E5-2695 v3 CPU's @ 2.30 GHz and 64 GB of RAM using MATLAB (R2015a, The MathWorks, Natick, MA).

## 6.4 Results and discussion

Fig. 6.2 shows reconstructed images from one dataset at systole and diastole and the temporal evolution of a horizontal line across the left and right ventricles. The results with the proposed method (GW-MR) show sharper edges, and finer details can be observed in the interior of the left ventricle both at 15 and 9 spokes per frame. Differences in the reconstructions become more evident in their temporal evolution. NLINV reconstructions show poorer contrast between blood and myocardium in the left ventricle as well as severe remaining striking artifacts, specially at 9 spokes per frame, in spite of the temporal median filter required by NLINV method. In Fig. 6.3, NLINV results before temporal filtering are included for the other two volunteers at 9 spokes per frame. Remaining artifacts severely degrade the temporal evolution of the dynamic image and are not completely removed by the temporal filter. On the contrary, artifacts

are better removed by GW-MR without additional post-processing steps while preserving spatial detail. Results for the three volunteers are shown jointly in the video provided as supplementary material.

Average reconstruction times are plotted in Fig. 6.4. GW-MR approximately doubles the computational demand of NLINV with both algorithms running in MATLAB without further optimizations. 14–17 seconds per frame are required by GW-MR, what hinders its practical application. However, the algorithm is highly parallelizable and GPU implementations will be investigated as future work.

One limitation of our study is the lack of a ground truth in RT imaging to obtain a quantitative measurement of the quality of the reconstructions. In future work, the usage of a numerical phantom will provide such a quality metric. Functional parameters such as ventricular volumes and ejection fraction computed both from RT and standard segmented acquisitions will be compared as well.

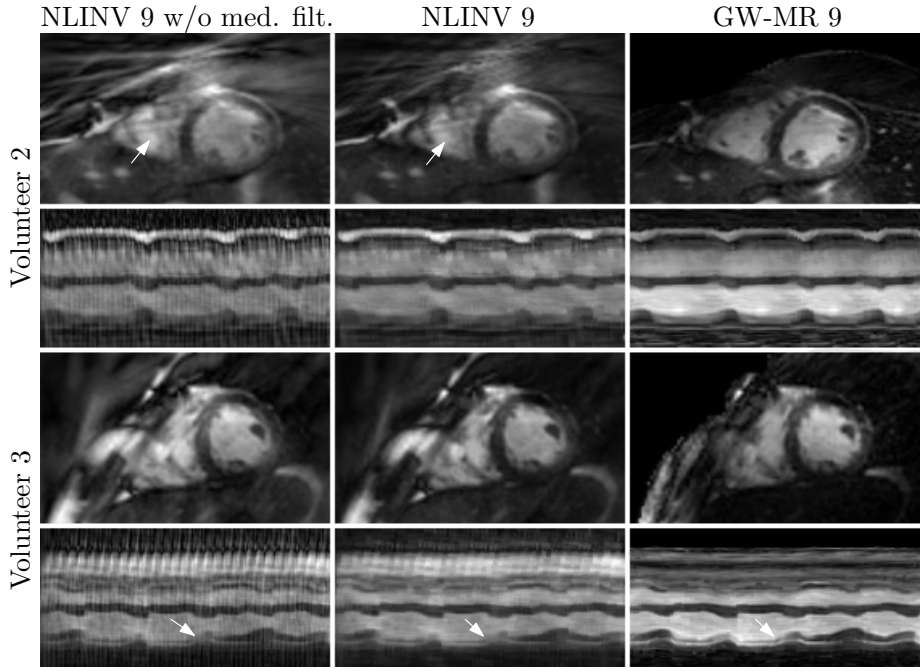


Figure 6.3: Diastolic phases and temporal evolution of a horizontal line through the center of the left ventricle reconstructed with NLINV without temporal filtering (left column), filtered (central column) and with GW-MR for volunteers two and three. Arrows in top row indicate a remaining artifact through the region of interest in NLINV reconstructions. Arrows in bottom row highlight the better depiction of the papillary muscle in GW-MR temporal evolution.

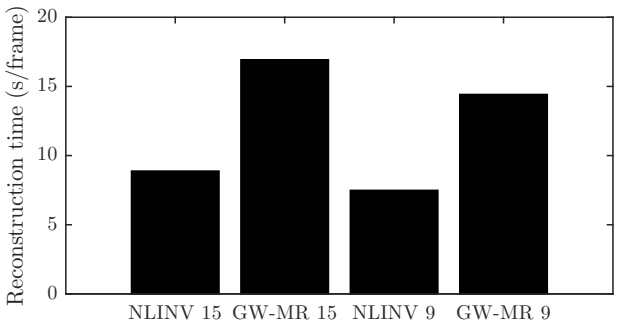


Figure 6.4: Average reconstruction time per frame with NLINV and the proposed method when 15 and 9 spokes per frame are used for the volunteer 3 data.

## 6.5 Conclusions

We have presented an algorithm based on continuous GR data acquisition and a robust GW registration method integrated in a temporal multiresolution scheme for ME/MC CS retrospective reconstruction of 2D RT MRI data. We have shown the application of this method to free-breathing, RT imaging of the heart employing only 9 spokes per frame, obtaining a final temporal resolution of 26 ms without view sharing or post-processing of the obtained images.

CHAPTER

# SEVEN

# CARDIO-RESPIRATORY MOTION ESTIMATION FOR COMPRESSED SENSING RECONSTRUCTION OF FREE-BREATHING 2D CINE MRI

**Accepted for publication as:**

Javier Royuela-del-Val[1], Muhammad Usman[2], Lucilio Cordero-Grande[2], Federico Simmross-Wattenberg[1], Marcos Martín-Fernández[1], Claudia Prieto[2] and Carlos Alberola-López[1]. Cardio-respiratory Motion Estimation for Compressed Sensing Reconstruction of Free-breathing 2D cine MRI. Proceedings of the 25th Anual Meeting of the International Society of Magnetic Resonance in Medicine (ISMRM 2017). Honolulu, HW, USA.

[1] Laboratorio de Procesado de Imagen, Universidad de Valladolid, Valladolid, Spain.

[2] Division of Imaging Sciences and Biomedical Engineering, Centre for the Developing Brain, King's College London, London, UK.

## 7.1 Synopsis

In this work a joint cardio-respiratory motion estimation technique is introduced for the compensation of both the respiratory and cardiac motion of the heart during free-breathing cardiac MRI examinations. The proposed technique is combined with an extra-dimensional reconstruction scheme in which respiratory and cardiac motions are resolved. Initial results for 2D cine cardiac MRI are presented for synthetic and real data.

## 7.2 Introduction

Respiratory motion is still an issue in MRI of the heart despite the introduction of Compressed sensing (CS) techniques Lustig et al. (2007), which significantly reduce the time needed for acquisition. Recently, an eXtra-Dimensional (XD) scheme has been proposed (XD-GRASP) Feng et al. (2016) which sorts k-space data according to both the respiratory and the cardiac phases at which they were were acquired. This way, cardiac and respiratory motions are separated and resolved in the final images. At reconstruction, temporal total variation (tTV) along the two pseudo-temporal dimensions defined (respiratory and cardiac phases) is used as sparse domain. An additional spatial TV regularization has been introduced. The following optimization problem results:

$$\underset{\mathbf{m}}{\text{minimize}} \frac{1}{2}\|\mathbf{y} - \mathbf{E}\mathbf{m}\|_2^2 + \lambda\|\nabla_{RC}\mathbf{m}\|_{\ell_1} + \lambda_s\|\nabla_{xy}\mathbf{m}\|_{\ell 1} \tag{7.1}$$

where $\mathbf{y}$ is the acquired k-space data, $\mathbf{E}$ the encoding operator (comprising coils sensitivities multiplication and undersampled non-uniform Fourier transform) and $\nabla_{RC}$ stands for the temporal finite differences operator along both respiratory and cardiac pseudo-temporal dimensions.

However, in this approach large motion between different cardio-respiratory states leads to a reduction of the sparsity of the signal after the application of temporal differences ($\nabla_{RC}$). CS based reconstruction methods have been successfully combined with motion compensation (MC) techniques either to correct for the respiratory motion Usman et al. (2013) or to estimate the heart beat motion to foster the sparsity of the dynamic data, hence improving the quality of the reconstructed images Royuela-del Val et al. (2017a). These methods have shown to enable higher acceleration factors than standard CS methods or alternatively, for a given acceleration factor, to give rise to better images.

In this work, we propose a MC technique to jointly estimate the respiratory and cardiac motions of the heart and we introduce it in a XD reconstruction scheme, enabling the MC-CS reconstruction of respiratory resolved cardiac MRI. We show initial results for the reconstruction of 2D free-breathing cardiac cine MRI, on both synthetic and real data.

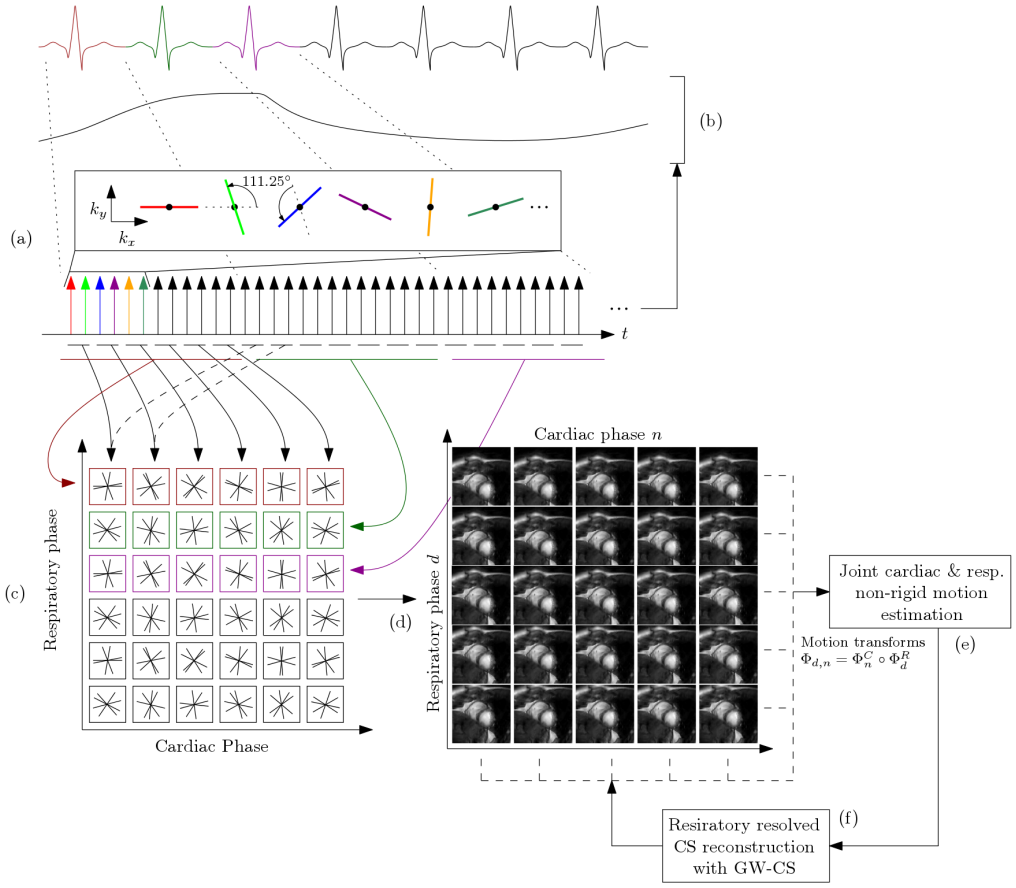


Figure 7.1: Acquisition and reconstruction diagram. Data is continuously acquired with a Golden Radial trajectory (a) with simultaneous ECG recording. The respiratory signal is then generated from the data itself (b). The k-space data is sorted according to its corresponding respiratory and cardiac phase (c) and an initial XD-GRASP reconstruction is performed (d). Respiratory and cardiac motion are jointly estimated from this initial reconstruction (e) and introduced in the final MC-XD-CS formulation (f).

## 7.3 Methods

The general procedure is summarized in Figure 7.1. Data is continuously acquired following a Golden Radial trajectory and ECG is recorded for synchronization.

### 7.3.1 Motion estimation

We model the cardio-respiratory motion as the composition of two independent spatial deformations:

$$\Phi_{r,c}^{R,C} = \Phi_r^R \circ \Phi_c^C \tag{7.2}$$

where $\Phi_r^R$ describes the respiratory deformation at respiratory state $r$ and $\Phi_c^C$ the cardiac motion at cardiac phase $c$. Both models are based on free-form deformations and a groupwise registration procedure Royuela-del Val et al. (2016a). In a first step data from each cardiac cycle is merged together. A low temporal resolution sequence results from both the respiratory signal and $\Phi^R$ are estimated. In a second step, the XD scheme is applied and cardiac motion is estimated jointly from all the images at different respiratory states.

### 7.3.2 MC-CS XD Reconstruction

By composing $\Phi^R$ and $\Phi^C$ we define the MC operator $\Phi^{R,C}$ that, when applied to the dynamic image $\mathbf{m}$, deforms it to a common cardio-respiratory configuration. We introduce it in the sparsity regularization term of the XD-CS reconstruction problem and solve:

$$\underset{\mathbf{m}}{\text{minimize}} \frac{1}{2}\|\mathbf{y} - \mathbf{E}\mathbf{m}\|_2^2 + \lambda\|\nabla_{RC}\Phi^{R,C}\mathbf{m}\|_{\ell_1} + \lambda_s\|\nabla_{xy}\mathbf{m}\|_{\ell 1} \tag{7.3}$$

### 7.3.3 Experiments

We first use synthetic data generated with the numerical phantom XCAT Segars et al. (2010); Wissmann et al. (2014). This way, a ground truth is available and the structure similarity index (SSIM) is calculated for quantitative validation. In order to study the sensitivity of the proposed method to errors in the respiratory synchronization, we reconstruct the simulated data using the respiratory signal provided by XCAT and the one estimated from the data.

Secondly, a healthy volunteer was scanned with a 32-element cardiac coil and the described trajectory on a 1.5T Philips scanner during 14 seconds. Other relevant scan parameters include TR/TE/$\alpha$ = 2.9ms/1.44ms/60° , FOV = 320x320mm$^2$, spatial resolution of 2x2mm$^2$. Reconstructed images are shown for visual quality assessment.

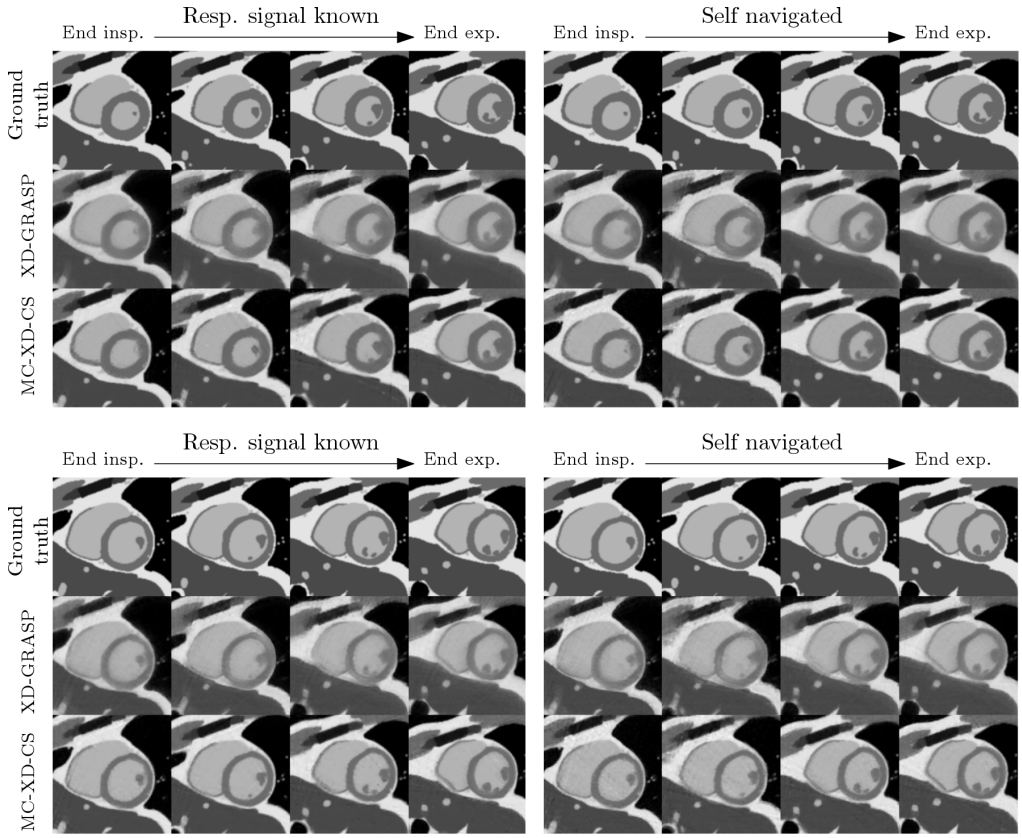


Figure 7.2: SSIM calculated on the images in Figure 2 for each cardiac phase. The SSIM has been averaged along the different respiratory states.

### 7.3.4 Results and discussion

In Figure 7.2 the results obtained from the synthetic data are shown at four respiratory states for systole and diastole. Sharper edges and better contrast between blood and myocardium can be appreciated in the proposed method when compared with XD-GRASP reconstructions, in which no MC is performed. No significant degradation of the image quality is observed when using the respiratory signal estimated from the data for self-navigation. In Figure 7.3, the SSIM calculated shows consistent superior performance of the proposed method along the cardiac cycle.

Figure 7.4 shows the results from the real data at systole (top) and diastole (bottom) for five respiratory states. Less undersampling artifacts and better small papillary muscles delineation are observed when the MC technique is introduced.

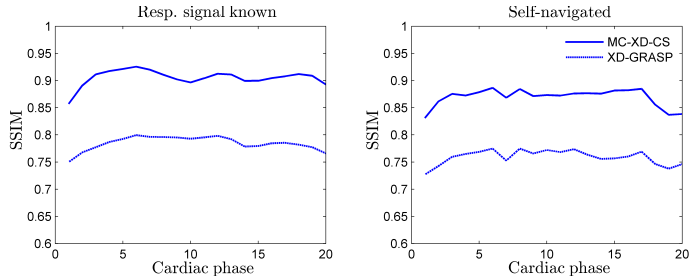


Figure 7.3: SSIM calculated on the images in Figure 7.2 for each cardiac phase. The SSIM has been averaged along the different respiratory states.

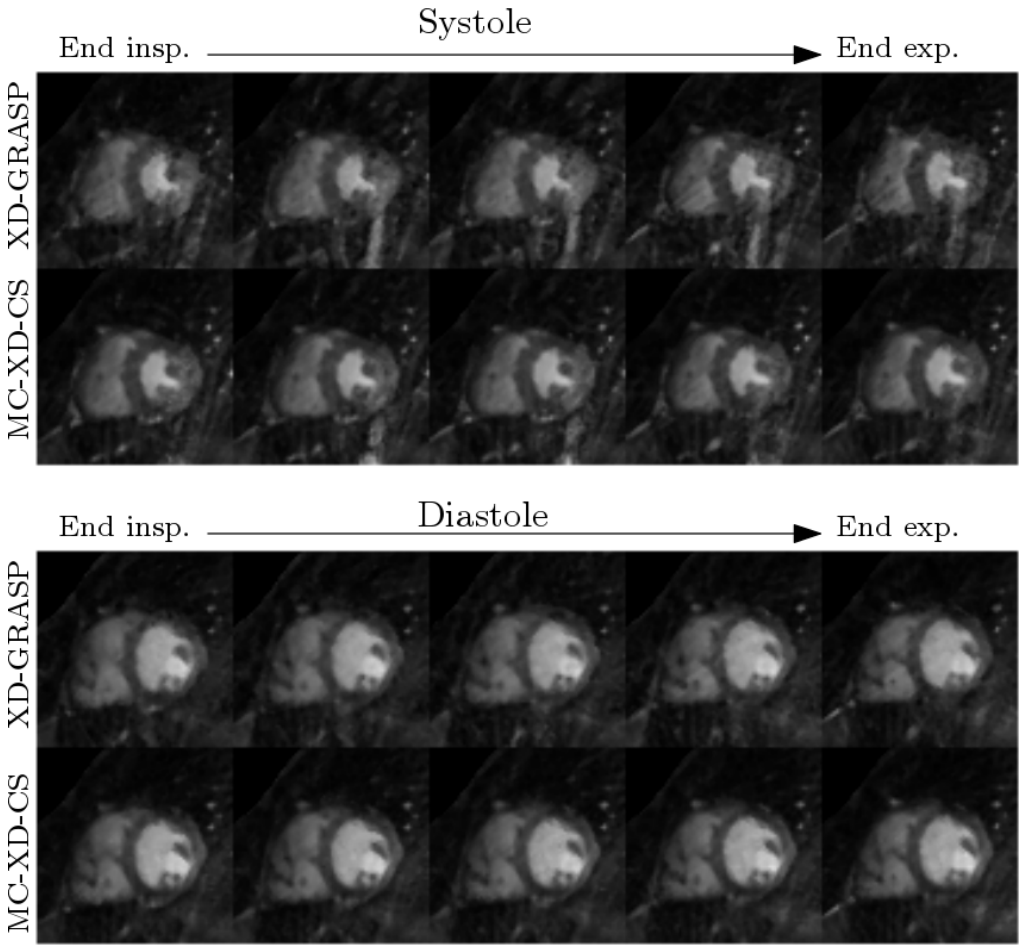


Figure 7.4: Results obtained from volunteer data. MC-XD-CS images shows less remaining undersampling artifacts and better delineation of papillary muscles.

### 7.3.5 Conclusion

To the best of our knowledge, in this work a joint cardio-respiratory non-rigid MC technique has been introduced for the first time in a XD CS reconstruction scheme. The results reported show better performance than the non-MC counterpart and robustness against respiratory synchronization errors.

CHAPTER

**EIGHT**

# LIBSTABLE: FAST, PARALLEL AND HIGH-PRECISION COMPUTATION OF $\alpha$-STABLE DISTRIBUTIONS IN R, C/C++ AND MATLAB

**Published as:**

Javier Royuela-del-Val[1], Federico Simmross-Wattenberg[1] and Carlos Alberola-López[1]. Libstable: Fast, Parallel and High-Precision Computation of alpha-Stable Distributions in C, MATLAB and R. Journal of Statistical Software, 78(1):1–25, 2017

[1] Universidad de Valladolid

## Abstract

$\alpha$-stable distributions are a family of well-known probability distributions. However, the lack of closed analytical expressions hinders their application. Currently, several tools have been developed to numerically evaluate their density and distribution functions or to estimate their parameters, but available solutions either do not reach sufficient precision on their evaluations or are excessively slow for practical purposes. Moreover, they do not take full advantage of the parallel processing capabilities of current multi-core machines. Other solutions work only on a subset of the $\alpha$-stable parameter space. In this paper we present a C/C++ library and front-ends for MATLAB and R that permit parallelized, fast and high precision evaluation of density, distribution and quantile functions,

as well as random variable generation and parameter estimation of $\alpha$-stable distributions in their whole parameter space. The library here described can be easily integrated on third party developments.

**Keywords:** $\alpha$-stable distributions, numerical calculation, parallel processing

## 8.1 Introduction

$\alpha$-stable distributions are a family of probability distributions that permit adjustable levels of heavy tails and skewness and include distributions such as Gaussian, Cauchy and Lévy as particular cases. They were first introduced by Lévy (1925) and have since been applied in many research fields. The increasing interest on $\alpha$-stable distributions is due, on the one hand, to the empirical evidence that they properly describe the behavior of real data exhibiting impulsiveness or strong asymmetries; on the other hand, the generalized central limit theorem (Samorodnitsky and Taqqu, 1994) states that the normalized sum of independent and identically distributed random variables with finite or infinite variance converges, if so, to an $\alpha$-stable distribution. This result provides theoretical support when the data under study can be interpreted as the superposition of many independent sources. This way, Mandelbrot and Wallis (1968) model precipitation data as $\alpha$-stable measurements, Fama (1965); Borak et al. (2011) use them to predict stock prices and asset returns, Simmross-Wattenberg et al. (2011); Willinger et al. (1997) show that the marginal distribution of aggregated network traffic may be accurately modeled by stable laws; in addition, Vegas-Sánchez-Ferrero et al. (2012) use them to characterize speckle noise in medical ultrasonic data, Salas-Gonzalez et al. (2013) model white and gray matter of the brain in magnetic resonance imaging as $\alpha$-stable random variables and Gonchar et al. (2003) characterize ion current fluctuations in plasma physics as being $\alpha$-stable. All these phenomena share the common property of being markedly impulsive in nature and, in many cases, strongly asymmetrical, so $\alpha$-stable distributions emerge as natural candidates to work with. However, stable distributions are not limited to modeling natural phenomena. Li et al. (2013) describe how to use them to compute distance (or similarity) in high-dimensional data and Li et al. (2014) use them to recover sparse signals under compressed sensing theory. Both of these proposals, in turn, have many applications on their own and the list is far from complete.

The major drawback for the application of $\alpha$-stable models is the lack of closed analytical expressions for their probability density function (PDF) or cumulative distribution function (CDF) except in particular cases, which makes the application of numerical methods a must. Besides, the non-existence of moments of order two or higher (except in the Gaussian case) increases the difficulty in estimating their parameters to fit real data. Several authors have addressed both the numerical evaluation of the PDF or CDF of $\alpha$-stable distributions (Nolan, 1997; Mittnik et al., 1999a; Belov, 2005; Menn and Rachev, 2006; Górska and Penson, 2011) and the estimation of their parameters (Fama and Roll, 1971; Koutrouvelis, 1981; McCulloch, 1986; Mittnik et al., 1999b; Nolan, 2001; Fan, 2006; Salas-Gonzalez et al., 2009) and have proposed different methods and algorithms for these purposes (details are discussed in Section 8.2). Some authors also provide implementations of their own or others' methods, offering software solutions or packages in various common computer languages. However, some of these solutions are not fully operational in their public domain versions and do not take advantage of multi-core processors (Nolan, 2006), have limited accuracy (Belov, 2005; Menn and Rachev, 2006) or take a computation time that results unaffordable for several practical applications (Veillette, 2010; Liang and Chen, 2013).

In this paper we present a C/C++ library and front-ends for MATLAB (The MathWorks, Inc., 2013) and R (R Core Team, 2015) that permit parallelized, fast and high precision evaluation of density and distribution functions, random variable generation and parameter estimation in $\alpha$-stable distributions. The library can be easily integrated in third party developments to be used by practitioners. Its utilization in MATLAB and R is straightforward and takes advantage of both the high efficiency of the compiled C/C++ code and the familiar interface and statistical tools of MATLAB and R environments.

The rest of the paper is organized as follows. In Section 8.2, currently proposed algorithms and methods to numerically evaluate the density and distribution functions of $\alpha$-stable distributions are described, as well as reported methods to estimate their parameters. In Section 8.3, the developed library and its functionality are presented. The results obtained with the library are discussed in Section 8.4. In Section 8.5, the usage of the proposed library is described. Finally, Section 8.6 describes main conclusions and further work possibilities derived from this work.

## 8.2 Numerical methods in $\alpha$-stable distributions

$\alpha$-stable distributions are typically described by their characteristic function (CF) due to the fact that no closed expressions exist for the general case. Let $\Phi(t) = \exp[\Psi(t)]$ denote this function with (Samorodnitsky and Taqqu, 1994):

$$\Psi(t)=\begin{cases} -|\sigma t|^{\alpha}\left[1-i\beta\tan\left(\frac{\pi\alpha}{2}\right)\operatorname{sign}(t)\right]+i\mu t, & \alpha\neq 1, \\ -|\sigma t|\left[1+i\beta\frac{2}{\pi}\operatorname{sign}(t)\ln\left(|t|\right)\right]+i\mu t, & \alpha=1, \end{cases} \tag{8.1}$$

where

$$\operatorname{sign}(t) \quad = \quad \begin{cases} 1, & t>0, \\ 0, & t=0, \\ -1, & t<0. \end{cases}$$

The four parameters above are (1) the stability index $\alpha \in (0, 2]$, (2) the skewness parameter $\beta \in [-1, 1]$, (3) the scale parameter $\sigma > 0$ and (4) the location parameter $\mu \in \mathbb{R}$. An $\alpha$-stable distribution is referred to as standard if $\sigma = 1$ and $\mu = 0$. When $\alpha = 2$ the distribution becomes normal with standard deviation $\sigma/\sqrt{2}$ and mean $\mu$ ($\beta$ becomes irrelevant). The Cauchy distribution results from setting $\alpha = 1$ and $\beta = 0$ with scale parameter $\sigma$ and location parameter $\mu$, and the Lévy distribution when $\alpha = 0.5$ and $\beta = 1$. These are the only cases for which the PDF can be expressed analytically. Otherwise, the PDF has to be calculated numerically.

The next subsections discuss different methods proposed in the literature to obtain the PDF and CDF, to estimate the parameters of $\alpha$-stable distributions and to generate samples of an $\alpha$-stable random variable.

### 8.2.1 Numerical computation of $\alpha$-stable distributions

The PDF and CF of any probability function are related via the Fourier inversion formula given by

$$f(x) = \frac{1}{2\pi}\int_{-\infty}^{+\infty}\phi(t)\mathrm{e}^{-itx}\,\mathrm{d}t = \frac{1}{2\pi}\int_{-\infty}^{+\infty}\mathrm{e}^{\psi(t)-itx}\,\mathrm{d}t. \tag{8.2}$$

When substituting Equation 8.1 in Equation 8.2 the resulting integral cannot be, as a rule, solved analytically; therefore it must be evaluated by numerical methods. To this end, the well-known fast Fourier transform (FFT) provides an algorithm to efficiently evaluate the previous integral. Mittnik et al. (1999a)

apply the FFT directly to calculate the PDF. However, this approach suffers from several important drawbacks. First, the algorithm provides the value of the integral on a set of evenly spaced points of evaluation. This is not valid for some applications, where the PDF or CDF must be evaluated at some specific set of points. A posterior step of interpolation is then required, which introduces additional computational costs and reduces precision. Second, the method is only suitable for $\alpha$ close to 2, for which the tails of the distribution decay more quickly. When $\alpha$ is small, the tails decay very slowly and the aliasing effect becomes more noticeable, thus reducing the achievable precision. Experimentally, the committed absolute error is in the order of $10^{-5}$, but relative error goes as high as $10^{-2}$. Menn and Rachev (2006) propose a method based on a refinement of the FFT to increase precision in the central part of the PDF. The tails of the distribution are calculated via the Bergström asymptotic series expansion (Zolotarev, 1986), which provides an alternative expression as an infinite sum of decaying terms. This way they achieve relative precision of about $10^{-4}$, but this precision heavily depends on the values of $\alpha$ and $\beta$ and the method is only applicable when $\alpha > 1$.

Górska and Penson (2011) follow a different approach and obtain explicit expressions for the PDF and CDF as series of generalized hypergeometric functions. However, the expressions involved in the calculation are expensive to evaluate and the results are only valid for some rational values of the parameters $\alpha$ and $\beta$, so they are not valid for the whole parameters space.

When compared with the FFT, direct integration of the expression in Equation 8.2 by numerical quadrature initially implies a higher computational cost, but evaluation can be performed at any desired set of points without the need of additional interpolation steps and there is no restriction on the values of the distribution parameters. This method has been implemented by Nolan (1999)*. However when $\alpha$ is small the integrand oscillates very quickly and its amplitude decays slowly along the infinite integration interval, which limits the achievable precision although many evaluations of the integrand are used. According to the author, the method results are valid only for $\alpha > 0.75$ and it achieves a precision in the order of $10^{-6}$. Similar results have been obtained later by Belov (2005), where the infinite integrand interval is divided in two (one bounded and the other infinite) and two quadrature formulae are applied.

*Although finally published in 1999, this article is already cited in Nolan (1997) as a "to appear in" reference, so the described software therein is earlier than 1997.

In order to overcome the previous difficulties, Nolan (1997) obtains a new set of equations from the original ones by means of an analytic extension of the integrand to the complex plane. This way, a continuous, bounded, non-oscillating integrand is obtained. Moreover, the integration interval becomes finite. The expressions obtained allow the author to achieve, by numerical quadrature, a relative accuracy in the order of $10^{-14}$ in most of the parameter space. For numerical convenience, a slightly different parameterization of the distribution is employed, based on Zolotarev (1986) M parameterization. The modification introduced consists in a shift of the distribution along the abscissae axis in order to avoid the discontinuity of the distribution at $\alpha = 1$. In this paper, we denote the change in parameterization by the subindex 0 and the resulting CF is given by $\Phi_0(t) = \exp[\Psi_0(t)]$ where

$$\Psi_0(t)=\begin{cases}-|\sigma t|^{\alpha}\left[1+i\beta\tan\left(\frac{\pi\alpha}{2}\right)\mathrm{sign}(t)\left(|\sigma t|^{1-\alpha}-1\right)\right]+i\mu_0 t, & \alpha\neq 1,\\ -|\sigma t|\left[1+i\beta\frac{2}{\pi}\mathrm{sign}(t)\ln\left(|\sigma t|\right)\right]+i\mu_0 t, & \alpha=1.\end{cases} \tag{8.3}$$

The parameters $\alpha$, $\beta$ and $\sigma$ keep their previous meaning while the original and modified location parameters $\mu$ and $\mu_0$ are related according to

$$\mu = \begin{cases} \mu_0 - \beta\tan\left(\frac{\alpha\pi}{2}\right)\sigma, & \alpha \neq 1,\\ \mu_0 - \beta\frac{2}{\pi}\sigma\ln(\sigma), & \alpha = 1.\end{cases} \tag{8.4}$$

With this modification, the resulting distribution is continuous in its four parameters, which is convenient when estimating the parameters of the distribution or approximating its PDF or CDF.

### 8.2.2 Parameter estimation of $\alpha$-stable distributions

As previously explained, the lack of closed expressions for the PDF or CDF of $\alpha$-stable distributions implies a major drawback to estimate their parameters. Therefore, the techniques employed for the estimation usually rely on numerical evaluations of these functions or, alternatively, are based on other properties of the distributions.

Several methods can be found in the related literature. Hill (1975) proposes the estimation of the $\alpha$ parameter by linear regression on the right tail of the empirical distribution. However, in many practical cases the method is not applicable because of the high number of samples needed to detect the tail behavior. McCulloch (1986) proposes an algorithm to estimate the four parameters

of the $\alpha$-stable distribution simultaneously from sample quantiles and tabulated values. The resulting estimator has a very low computational cost but a low accuracy as well. However, it can be conveniently used as an initial estimation for other methods. Koutrouvelis (1981) departs from the empirical CF to obtain, by means of recursive linear regressions on its log-log plot, estimators for $\alpha$ and $\sigma$ in a first step and for $\beta$ and $\mu$ on a second one. The method implies a higher computational cost than the quantile method, but yields more accurate results.

Maximum likelihood (ML) estimation is considered the most accurate estimator available for $\alpha$-stable distributions (Borak et al., 2011). However, numerical methods to both approximate the PDF and to maximize the likelihood of the sample must be used, which implies a very high computational cost due to the numerous PDF evaluations required to maximize the likelihood in the four-dimensional parameter space. However, increasing computer capabilities and the use of precalculated values of the PDF makes the use of this method possible in certain applications (Nolan, 2001).

### 8.2.3 Generation of $\alpha$-stable random variables

Given the lack of closed expressions for the CDF or its inverse (the quantile function, $\text{CDF}^{-1}$), the simulation of $\alpha$-stable distributed random variables cannot be achieved easily from a uniform random variable. Chambers et al. (1976) provided a direct method to generate an $\alpha$-stable random variable by means of the transformation of an exponential and a uniform random variable. The method proposed lacked a theoretical demonstration until Weron (1996) gave an explicit proof and slightly modified the original expressions. The resulting method is regarded as the fastest and the most accurate available (Weron, 2004).

Based on the methods described so far, several software tools are currently available. The program STABLE (Nolan, 2006) employs Nolan's expressions (Nolan, 1997) for the high precision computation of PDF, CDF and quantile function and maximum likelihood parameter estimation. However, a fully operational version of the software is not publicly available. Veillette (2010) has developed a MATLAB package that also applies Nolan's expressions for high precision PDF and CDF evaluation and Koutrouvelis (1981) method for parameters estimation based on the CF. However, the performance obtained is low when trying to achieve high precision or when fitting a large data sample. A package with similar features and characteristics has been reported by Liang and Chen (2013).

## 8.3 Algorithms and implementation

One purpose of the proposed library is to have a fast and accurate tool to numerically evaluate the PDF and CDF of $\alpha$-stable distributions. From the previous study, it may be concluded that those methods that employ Nolan's expressions give the most accurate results. Therefore, the developed library is based on them. However, these expressions have some issues which must be addressed. First, the mathematical expressions involved in the calculation are, in computational terms, expensive to evaluate. Second, although the integral involved in the calculations (a convenient transformation of Equation 8.2) has some desirable properties, it is generally hard to approximate. Therefore some strategies have to be elaborated in order to evaluate it accurately and efficiently.

### 8.3.1 Fast and accurate evaluation of Nolan's expressions

Nolan's expressions to calculate the PDF of a standard $\alpha$-stable distribution with $\alpha \neq 1$ are:

$$f_{\boldsymbol{X}}(x;\alpha,\beta) = \begin{cases} \dfrac{\alpha}{\pi(x-\zeta)|\alpha-1|}\displaystyle\int_{-\theta_0}^{\pi/2} h_{\alpha,\beta}(\theta;x)\,\mathrm{d}\theta & x>\zeta \\ \dfrac{\Gamma(1+\frac{1}{\alpha})\cos(\theta_0)}{\pi(1+\zeta^2)^{\frac{1}{2\alpha}}} & x=\zeta \\ f_{\boldsymbol{X}}(-x;\alpha,-\beta) & x<\zeta \end{cases} \tag{8.5}$$

where

$$\begin{aligned} \zeta(\alpha,\beta) &= -\beta\tan\left(\frac{\pi\alpha}{2}\right) \\ \theta_0(\alpha,\beta) &= \frac{1}{\alpha}\arctan\left(\beta\tan\left(\frac{\pi\alpha}{2}\right)\right) \\ h_{\alpha,\beta}(\theta;x) &= (x-\zeta)^{\frac{\alpha}{\alpha-1}}\,V_{\alpha,\beta}(\theta)e^{-(x-\zeta)^{\frac{\alpha}{\alpha-1}}\,V_{\alpha,\beta}(\theta)} \\ V_{\alpha,\beta}(\theta) &= (\cos(\alpha\theta_0))^{\frac{1}{\alpha-1}}\left(\frac{\cos(\theta)}{\sin(\alpha(\theta_0+\theta))}\right)^{\frac{\alpha}{\alpha-1}}\frac{\cos(\alpha\theta_0+(\alpha-1)\,\theta)}{\cos(\theta)} \end{aligned} \tag{8.6}$$

When $\alpha = 1$, the definition of the expressions changes to

$$f_{\boldsymbol{X}}(x;1,\beta) = \begin{cases} \int_{-\frac{\pi}{2}}^{\pi/2} h_{1,\beta}(\theta;x)\,\mathrm{d}\theta & \beta \neq 0 \\ \dfrac{1}{\pi(1+x^2)} & \beta = 0 \end{cases} \tag{8.7}$$

where

$$\begin{aligned} h_{1,\beta}(\theta;x) &= e^{-\frac{\pi x}{2\beta} V_{1,\beta}(\theta)} \\ V(\theta;1,\beta) &= \frac{2}{\pi}\left(\frac{\frac{\pi}{2}+\beta\theta}{\cos(\theta)}\right) e^{\frac{1}{\beta}(\frac{\pi}{2}+\beta\theta)\tan(\theta)} \end{aligned} \tag{8.8}$$

It is worth noticing that the change in the definition of the expressions above when $\alpha = 1$ does not imply a discontinuity in the PDF or CDF (Nolan, 1997). For a general distribution, the PDF is calculated for the corresponding standardized version ($\sigma = 1$ and $\mu_0 = 0$) and then properly scaled and shifted back:

$$\begin{aligned} f_{\boldsymbol{X}}(x;\alpha,\beta,\sigma,\mu_0) &= \tfrac{1}{\sigma} f_{\boldsymbol{X}}\left(\tfrac{x-\mu_0}{\sigma};\alpha,\beta\right) \\ F_{\boldsymbol{X}}(x;\alpha,\beta,\sigma,\mu_0) &= F_{\boldsymbol{X}}\left(\tfrac{x-\mu_0}{\sigma};\alpha,\beta\right) \end{aligned} \tag{8.9}$$

In Figure 8.1 the function $h_{\alpha,\beta}(\theta;x)$ to be integrated is represented both in linear and logarithmic scales. As the point of evaluation $x$ of the PDF increases, the integrand becomes closer to a singular peak. The same behavior occurs when $x$ tends to $\zeta$. The numerical method employed to evaluate the integral should avoid missing this peak as well as to evaluate the integrand at regions with a marginal contribution to the final result. In order to focus on the relevant areas, the integral is divided as represented in Figure 8.2. Before integrating, the peak of $h_{\alpha,\beta}(\theta;x)$ is located numerically. Then, a symmetric interval around the peak where the integrand holds above a determined threshold is defined. The value of the threshold depends on the accuracy required to evaluate the integral. This required accuracy can be easily adjusted by the user. With the interval of integration so divided, a first approximation to the final value of the integral is obtained by applying Gauss-Kronrod quadrature formulas (Press et al., 1994). Finally, the area under the rest of the integration interval is calculated only to the desired precision, monitoring the contribution of new intervals to the current value of the integral and stopping the procedure when additional contributions are irrelevant.

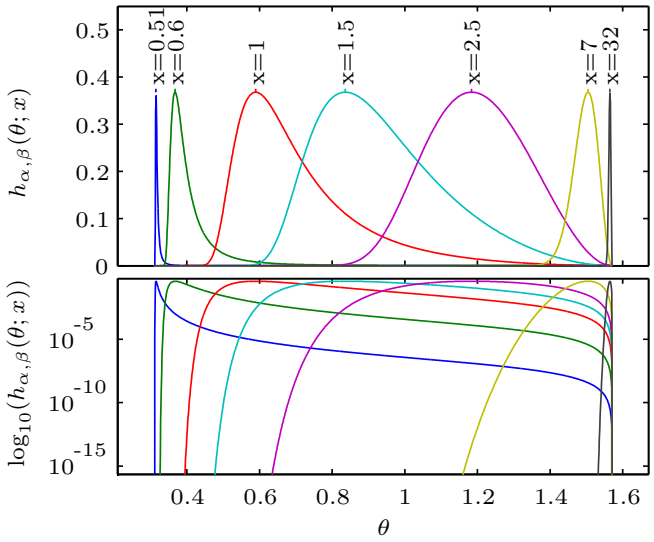


Figure 8.1: Integrand function $h_{\alpha,\beta}(\theta;x)$ for $\alpha = 1.5$ and $\beta = 0.5$ and various values of $x$ in linear (top) and logarithmic (bottom) scales. As $x$ increases or approaches $\zeta$, most of the area under the curve gets concentrated in a narrow peak close to one extreme of the integration interval.

When calculating the CDF, a similar approach is followed. In this case, the maximum of the integrand is always at one extreme of the integration interval (see Nolan, 1997, for details on the expressions involved), so there is no need to find it numerically. To calculate the quantile function, the CDF is numerically inverted. An initial guess of the value of the function is obtained by interpolation over tabulated CDF values and then a root finding algorithm is applied. Routines employed for numerical quadrature and root finding are supplied by the GNU Scientific Library (**GSL**, Galassi et al., 2009).

For the particular cases in which the PDF and CDF have closed analytical expression (Gaussian, Cauchy and Lévy distributions, as exposed in Section 8.2) **libstable** will make use of them to avoid unnecessary computations.

### 8.3.2 Parallelization of the workload

The evaluation of the PDF, CDF or $\text{CDF}^{-1}$ at one point is completely independent from the evaluation at any other different point. Besides, in practical applications it will be required to evaluate the functions in several points, as when estimating the $\alpha$-stable parameters of given data with a method based on the PDF or CDF of distribution. Therefore, the evaluation at different points

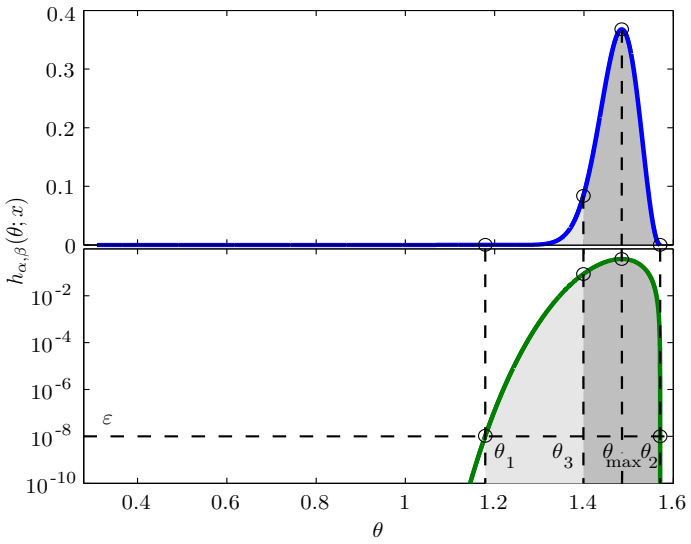


Figure 8.2: Subdivision of the integration interval for $\alpha = 1.5$, $\beta = 0.5$ and $x = 6$ in linear (top) and logarithmic scales (bottom). The maximum of the integrand ($\theta_{max}$) and points for which $h_{1.5,0.5}(\theta; x)$ crosses a threshold $\varepsilon$ ($\theta_1, \theta_2$) are located. Then, a symmetric interval around $\theta_{max}$ is determined ($\theta_3$).

can be done in parallel. When called, the library functions distribute the points of evaluation between several threads of execution. The number of available threads of execution can be fixed manually or determined automatically. When computation finishes, the results are gathered together. Parallelism has been implemented using POSIX Threads (**Pthreads**, Barney, 2011), which allows the programmer to accurately control the threads creation and execution. The distributions can be calculated in the original parameterization or in the modified one, given respectively by Equations 8.1 and 8.3.

### 8.3.3 Parameter estimation and random variable generation

Four different methods of parameter estimation of $\alpha$-stable distribution are available in the library. First, the McCulloch's (1986) method which yields very fast parameter estimation, at the cost of lower accuracy. Second, the iterative Koutrouvelis' (1981) method based on the sample CF, which produces better estimations with longer execution times. Third, maximum likelihood can be used directly. However, the elevated computational cost of both numerical evaluation of the PDF and maximization in the four-dimensional parameter space makes this method very slow when the sample size is large. For these cases, a modified

ML approach is implemented, in which the maximization search is only performed in the 2-D $\alpha$-$\beta$ space. On each iteration of the maximization procedure, $\sigma$ and $\mu$ are estimated with McCulloch's algorithm according to current $\alpha$, $\beta$ estimations.

The CMS method modified by Weron is used to simulate $\alpha$-stable random variables. To this end, a high quality uniform random number generator provided by the **GSL** is employed.

## 8.4 Results

In this section, the results obtained by the developed library are exposed and discussed. The analysis is focused on the precision and performance obtained when evaluating both the PDF and the CDF of $\alpha$-stable distributions.

### 8.4.1 Precision results

Since no tabulated values for these functions are available with enough precision in the literature, errors are measured against the numerical results provided by the program STABLE, which has been used frequently in the literature as ground truth (Weron, 2004; Belov, 2005; Menn and Rachev, 2006). Error is expressed in relative terms and measured for different values of the parameters $\alpha$ and $\beta$. The parameters $\sigma$ and $\mu$ are fixed to 1 and 0 respectively. The abscissae axis is divided in several intervals in a log-scale fashion. Errors committed in an evenly distributed set of points inside each interval are averaged. This way, the behavior at the tails and in the central region of the distribution can be analyzed independently.

The data obtained for a set of $\alpha$ and $\beta$ values is presented in Table 8.1. Omitted values correspond to intervals where the PDF or CDF equal zero or take on values below the machine minimum representable quantity. The precision obtained both at the tails and at the central part of the distribution is fairly high and in many cases close to the hardware precision limit employed in the calculations (about $10^{-16}$). The data obtained for a finer sweep of the parameters is summarized in Figure 8.3. The error data has been smoothed for convenient visualization with a median filter of size three. When $\alpha < 1$, the results obtained are in practice equivalent to those obtained by the program STABLE. When $\alpha$

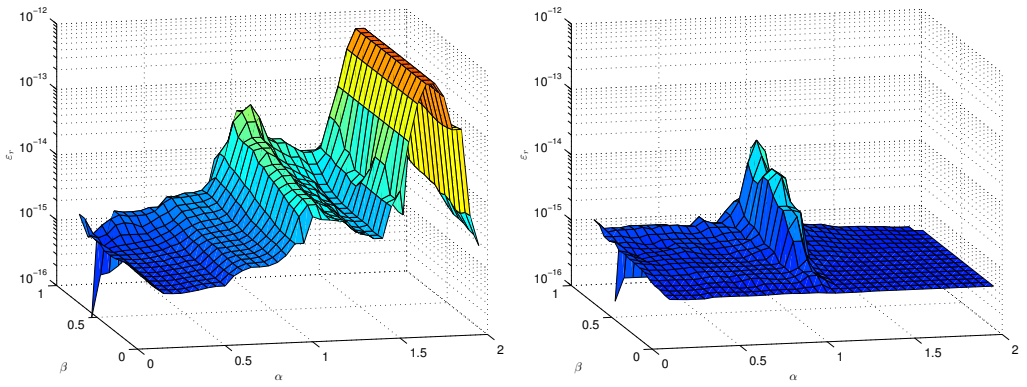


Figure 8.3: Averaged relative error in the calculation of the PDF (left) and CDF (right) of standard $\alpha$-stable distributions.

gets close to 1, the error increases since the expressions involved become singular and hard to integrate in this region. However, given the small relative error measured and the lack of exact values of the distribution, we cannot determine which software (the program STABLE used as reference or the proposed library) is in fact deviating from the true values of the distribution. In the calculation of the PDF the error increases also as $\alpha$ approaches 1.75. This can be due to the faster decay of the tails of the distribution, which makes small absolute differences in the values obtained translate into higher relative errors measured. Despite this, the relative error stays in the order of $10^{-13}$.

### 8.4.2 Performance results

The performance of the library is measured as the number of evaluations of the PDF or CDF it can execute per unit of time. To measure it, for a set of $\alpha$ and $\beta$ values, 100 calls to the library have been done, with 10000 evaluations of the PDF or CDF per call. The measurements are repeated setting the required precision to different values. The tests have been performed in a machine with four Quad-Core AMD Opteron(tm) Processor 8350 (16 cores in total) with a CPU frequency of 2.0 GHz. For comparison, results obtained for Veillette's MATLAB functions and with the **stabledist** package in R in the same machine are included. The program STABLE is only freely available for Windows operating system, so performance results are extrapolated from a similar machine running Windows.

Results for $\alpha = 0.75$ and $\beta = 0.5$ are summarized in Figure 8.4. For other values of the parameters, results exhibit the same behavior, up to a scale factor.

When moderate errors are tolerable, Veillete's MATLAB functions achieve a performance higher than the one of both program STABLE and the C/C++ library developed. This can be explained by the simpler quadrature method employed, which leads to a faster convergence when low precision is required. However, as precision requirements increase, the number of evaluations needed by the simpler quadrature method increases very quickly given its inferior convergence properties when compared with the more advanced rules and the strategy of integration used in **libstable**. Therefore, the performance of the MATLAB solution quickly decreases becoming much slower than the rest of the methods. Note that the MATLAB implementation is able to use several threads, so it is compared with the 16 threads curve. The performance of the **stabledist** R package is remarkably lower than both the program STABLE or the developed library, even for single threaded execution.

Finally, the parallel capability of the C/C++ library clearly outperforms the rest of alternatives when multiple processing cores are available (as it is usually the case in modern machines). For the CDF, the increase in performance with respect to the program STABLE is approximately equal to the number of threads used. In the case of the PDF, this increase is even higher given the superior performance with one execution thread. The results presented in Figure 8.4 allow us to estimate to what extent the proposed library is able to parallelize the workload to according to the Amdahl's law (Amdahl, 1967). Results indicate that between the 94% and 98% of the algorithm is being executed in parallel.

## 8.5 Usage of libstable

**Libstable** has been developed at the Image Processing Laboratory (LPI) to give support for various research projects based on $\alpha$-stable distributions, where it is used on a regular basis. It is distributed both as a C/C++ library with MATLAB and R front-ends. It has been thoroughly tested on specific applications. Its source code and sample programs are publicly available at `http://www.lpi.tel.uva.es/stable` under the GPLv3 (Free Software Foundation, 2007) license.

### 8.5.1 Compiling the library

The developed library can be easily compiled from the source code with the `make` command. **Libstable** depends on several numerical methods provided by

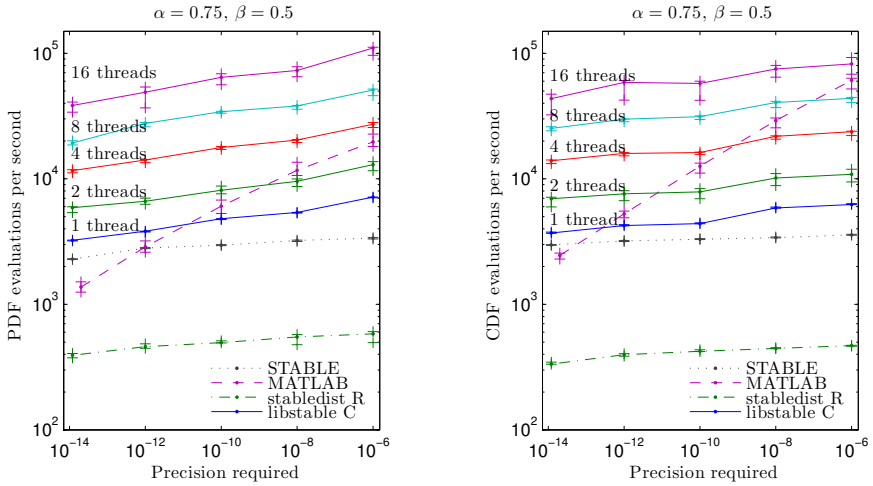


Figure 8.4: Performance of the calculation of PDF and CDF vs. required precision. Color indicates the number of execution threads employed. Median values and 95% confidence intervals are represented.

the **GSL** (Galassi et al., 2009), which must be installed in the system. After compilation, both shared (`libstable.so`) and static (`libstable.a`) versions of the library are produced.

Several example programs to test the main functions of **libstable** are also provided and compiled against the static version of the library by default. Further documentation on the library functions can be found within the library distribution.

### 8.5.2 Usage in C/C++ developments

The next example program (`example.c`) illustrates how to use **libstable** to evaluate the PDF of an $\alpha$-stable distribution with given parameters and with 0 parameterization (i.e., we use $\mu_0$ as opposed to $\mu$, recall Equations 8.3 and 8.4) at a single point $x$:

```
#include <stdio.h>
#include <stable_api.h>

int main (void)
{
  double alpha = 1.25, beta = 0.5, sigma = 1.0, mu = 0.0;
  int param = 0;
```

```
  double x = 10;
  StableDist *dist = stable_create(alpha, beta, sigma, mu, param);
  double pdf = stable_pdf_point(dist, x, NULL);
  printf("PDF(%g; %1.2f, %1.2f, %1.2f, %1.2f) = %1.15e\n",
                                  x, alpha, beta, sigma, mu, pdf);
  stable_free(dist);
  return 0;
}
```

The output of one execution of the example is:

```
PDF(10; 1.25, 0.50, 1.00, 0.00) = 3.225009046591297e-03
```

### Compiling and linking

If the **libstable** header files and compiled library are not located on the standard search path of the compiler and linker respectively, their location must be provided as command line flag to compile and link the previous program. The program must also be linked to the **GSL** and system `math` libraries. Typical command for compilation and static linking of a source file `example.c` with the GNU C compiler **gcc** is

```
$ gcc -O3 -I/path/to/headers -c example.c
$ gcc example.o /path/to/libstable/libstable.a -lgsl -lgslcblas -lm
```

The `-O3` option activates several optimization procedures of the **gcc** compiler. Other options can also be considered. When linking with the shared version of the library, the path to `libstable.so` must be provided to the system's dynamic linker, typically by defining the shell variable `LD_LIBRARY_PATH`. The path to the shared library must also be provided when linking the program:

```
$ gcc -L/path/to/libstable example.o -lgsl -lgslcblas -lm -lstable
```

### Setting general parameters

Some general parameters can be adjusted on the library, such as precision required or available number of threads. These parameters are stored as global variables that can be read and modified with the functions described below.

In multi-core systems, the functions

```
unsigned int stable_get_THREADS()
void stable_set_THREADS(unsigned int threads)
```

return and set up, respectively, the number of threads of execution used by the library. When setting the number of threads to 0, the library will use as many threads as processing cores are available in the system.

The relative tolerance indicates the precision required when calculating the PDF and CDF. The following functions return the current relative tolerance and set the desired one, respectively:

```
double stable_get_relTOL()
void   stable_set_relTOL(double reltol)
```

### Managing distributions

The library defines the structure `StableDist` which contains some values associated to an $\alpha$-stable distribution, such as its parameters, the parameterization employed and a random number generator. An $\alpha$-stable distribution with desired parameters $\alpha$, $\beta$, $\sigma$ and $\mu$ in parameterization `param` can be created by

```
StableDist * stable_create(double alpha, double beta,
                           double sigma, double mu, int param)
```

The function returns a pointer to a `StableDist` structure. This pointer is passed as an argument to other functions. Once the StableDist structure is created, the parameters of a distribution can be easily changed:

```
int stable_setparams(StableDist * dist, double alpha, double beta,
                     double sigma, double mu, double param)
```

The returned value can be one of the following predefined constants:

| | |
|---|---|
| INVALID: | Invalid or out of range parameters introduced |
| STABLE: | General $\alpha$-stable case |
| ALPHA_1: | $\alpha = 1$ case |
| GAUSS: | Gaussian distribution ($\alpha = 2$) |
| CAUCHY: | Cauchy distribution ($\alpha = 1$ and $\beta = 0$) |
| LEVY: | Lévy distribution ($\alpha = 0.5$ and $\beta = 1$) |

A copy of an existing distribution can be obtained by

```
StableDist * stable_copy(StableDist * src_dist);
```

To delete a distribution and free its associated memory resources call

```
void stable_free(StableDist * dist)
```

### Calculating PDF, CDF and CDF$^{-1}$

This section describes the functions provided to calculate the PDF, CDF and CDF$^{-1}$ of $\alpha$-stable distributions. Two possibilities are provided for each: a single point function and an vector function. The prototypes of the single point functions are:

```
double stable_cdf_point(StableDist * dist, const double x, double * err)
double stable_pdf_point(StableDist * dist, const double x, double * err)
double stable_inv_point(StableDist * dist, const double q, double * err)
```

Each function returns the value of the stable function being evaluated and stores in `err` an estimation of the absolute error committed. If this estimation is not required, a `NULL` pointer can be passed as argument instead. For the vector functions:

```
void stable_cdf(StableDist * dist, const double * x, const int Nx,
                double * pdf, double * err)
void stable_pdf(StableDist * dist, const double * x, const int Nx,
                double * cdf, double * err)
void stable_inv(StableDist * dist, const double * q, const int Nq,
                double * inv, double * err)
```

the number of evaluation points (`Nx`, `Nq`, respectively) must be provided. An estimation of the absolute error committed at each point of evaluation is stored in an array `err`. If this estimation is not required, a `NULL` pointer can be passed as argument instead.

### Random sample generation

In order to generate an $\alpha$-stable random sample with desired parameters and population size, a distribution must be created with those parameters as exposed above. Once the parameters have been set, the function

```
double stable_rnd_point(StableDist * dist)
```

returns a single realization of an $\alpha$-stable random variable. To obtain an vector of realizations the function

```
void stable_rnd(StableDist * dist, double * rnd, const unsigned int N)
```

stores in the `rnd` array `N` independent realizations of an $\alpha$-stable random variable.

When generating random samples, the function

```
void stable_rnd_seed(StableDist * dist, unsigned long int s)
```

initializes the internal random generator to a desired seed. This allows to reproduce results across different executions. Nevertheless, it will be usually desirable to obtain different results in different realizations, which involves to initialize the random generator to different seeds. This can be easily achieved by initializing to a time dependent seed such as

```
stable_rnd_seed(dist, time(NULL))
```

### Parameter estimation

Several methods are available in **Libstable** to estimate the parameters of $\alpha$-stable distributions from a data sample. Given its speed and simplicity, McCulloch (1986) method is always used as initial approximation to the final estimation. It can be invoked by the function

```
void stable_fit_init(StableDist * dist, const double * data,
                     const unsigned int N,  double * nu_c,double * nu_z)
```

This function sets the parameters of the distribution structure `dist` to the estimation obtained from the sample in `data`, of length `N`. `stable_fit_init` is employed in other iterative estimation methods which make use of the values stored in `nu_c` and `nu_z`. If these values are not required, a `NULL` pointer can be passed as an argument.

As previously exposed, the McCulloch estimator has low accuracy. **Libstable** provides other estimators when higher accuracy is required. Koutrouvelis (1981) iterative estimation is provided by the function

```
int stable_fit_koutrouvelis(StableDist * dist, const double * data,
                            const unsigned int N)
```

In this case, the parameters stored in the distribution `dist` when calling the function are considered as initial guesses of the final estimation. Therefore, `stable_fit_init` could be used before to obtain such approximation. The parameters in `dist` are then updated by the estimator procedure. If the iterative method finishes correctly, the function returns 0. Otherwise, a different value indicates that an error has occurred, such as no convergence of the iterative method or estimated parameter values out of their definition space (see section 8.2).

The high performance achieved in the calculation of the PDF allows to perform ML estimation directly in many practical situations. For best results, the library should be set to require only the needed relative precision (a value of $10^{-8}$ is recommended as a starting point) so that computational costs associated to the evaluation of the likelihood function is minimized. ML estimation of $\alpha$-stable distributions can be obtained by

```
int stable_fit_mle(StableDist *dist, const double *data,
                   const unsigned int N)
```

If the computational cost of this function is unacceptable, a modified ML method is provided. As exposed in section 8.3.3, it performs an optimization procedure only the $\alpha - \beta$ 2D space, thus simplifying the procedure and reducing the number of evaluations of the likelihood function required to find a solution. This method is implemented by the function

```
int_stable_fit_mle2d(StableDist *dist, const double *data,
                     const unsigned int N)
```

As in the Koutrouvelis estimator, ML and modified ML use the parameters stored in `dist` as initial guesses which are updated by the method. A return value different from 0 indicates some error has occurred during the execution of the algorithm.

An example of how to use the library to calculate the PDF, CDF and $\text{CDF}^{-1}$ with desired parameters, generate a random sample and, given this sample, estimate the parameters of an $\alpha$-stable distribution that best fits the generated data follows:

```
#include <stable_api.h>

int main(void)
{
  double x[100], q[100], pdf[100], cdf[100], inv[100], rnd[100];
  double alpha = 1.5, beta = 0.5, sigma = 2.0, mu = 4.0;
  int seed = 1234;
  int i;
  StableDist * dist;

  for (i = 0; i < 100; i++) {
    x[i] = -5 + i * 0.1;
    q[i] = 0.01 * (i + 0.5);
  }

  dist = stable_create(alpha, beta, sigma, mu, 0);
  stable_pdf(dist, x, 100, pdf, NULL);
  stable_cdf(dist, x, 100, cdf, NULL);
  stable_inv(dist, q, 100, inv, NULL);
  stable_rnd_seed(dist, seed);
  stable_rnd(dist, rnd, 100);

  stable_fit_init(dist, rnd, 100, NULL, NULL);
  stable_fit_koutrouvelis(dist, rnd, 100);

  printf("Estimated parameters: %f %f %f %f\n",
     dist->alpha, dist->beta, dist->sigma, dist->mu_0);
```

```
  stable_free(dist);
  return 0;
}
```

In this example, the only output on screen is

```
Estimated parameters: 1.535524 0.058148 1.799415 4.563211
```

### 8.5.3 Usage in MATLAB environment

MATLAB supports loading shared C libraries by calling the `loadlibrary` function. The shared version of the proposed library (`libstable.so`) and the header file `stable_api.h` are required. In order to start using **Libstable** execute the following command in MATLAB environment:

```
loadlibrary('libstable', 'stable_api.h')
```

Paths to `libstable.so` and `stable_api.h` must be in the current folder or included in MATLAB search path.

When the library is no longer needed, it can be unloaded by executing

```
unloadlibrary('libstable')
```

Several MATLAB functions in the form of `.m` files are provided to access the capabilities of **libstable**. These files can be easily modified by the user to adjust library parameters as needed. The managing of $\alpha$-stable distributions described in section 8.5.2 is performed by the provided functions, so it is not necessary to create or to delete the distributions.

#### Calculating PDF, CDF and CDF$^{-1}$

The functions

```
pdf = stable_pdfC(x, pars, pm)
cdf = stable_cdfC(x, pars, pm)
inv = stable_invC(q, pars, pm)
```

return a vector containing the evaluation of the PDF, CDF and CDF$^{-1}$, respectively, at the points in `x` (`q` for the CDF$^{-1}$). The parameters of the distribution are indicated in `pars = [alpha, beta, sigma, mu]`, and `pm = 0, 1` is the parameterization employed. The returned vector will have the same size as `x`.

By default, these functions set the library to use the maximum number of available threads of execution and set the relative precision of the library to a fixed value of $10^{-12}$. This values can be easily changed by modifying the corresponding `.m` files.

The letter "C" on the functions names is included to indicate that a C shared library is being invoked when calling the function.

### Random variable generation

The generation of $\alpha$-stable random variables is provided by the function

```
rnd = stable_rndC(N, pars, pm, seed)
```

A column vector containing `N` independent realizations of an $\alpha$-stable random variable with parameters `pars = [alpha, beta, sigma, mu]` in parameterization `pm = 0, 1` is returned. The seed to initialize the random numbers generator can be set by `seed`. If not provided, by default it is set to system time each time `stable_rndC` is called. These behavior can be modified in the function file.

### Parameter estimation

A MATLAB function is provided for each of the estimation methods described in section 8.5.2:

```
p = stable_fit_initC(data)
p = stable_fit_koutrouvelisC(data)
p = stable_fit_mleC(data)
p = stable_fit_mle2dC(data)
```

These functions perform McCulloch, Koutrouvelis, ML and modified ML estimation, respectively, in the sample data `data`. The estimated parameters are returned in `p` vector. By default, McCulloch estimator is used by other methods as initial estimation of the parameters. A user defined initial estimation can be used by passing an additional argument `p_ini = [alpha_ini, beta_ini, sigma_ini, mu_ini]`, e.g.,

```
p = stable_fit_mle2dC(data, p_ini)
```

The following lines serve as an example of a MATLAB session in which **Libstable** is used to calculate the PDF, CDF and CDF$^{-1}$ of an $\alpha$-stable distribution with desired parameters, generate a random sample and, given the sample, estimate the parameters of the $\alpha$-stable distribution.

In first place, the library must be loaded:

```
>> loadlibrary('libstable', 'stable_api.h')
```

Vectors of points of evaluation and parameters are initialized. The parameterization employed is also indicated:

```
>> x = -5 : .1 : 5;
>> q = 0.005 : 0.01 : 0.995;
>> p = [1.5, 0.5, 0.5, -1.0];
>> param = 0;
```

PDF, CDF, CDF$^{-1}$ are evaluated and the results stored in corresponding vectors:

```
>> pdf = stable_pdfC(p, x, param);
>> cdf = stable_cdfC(p, x, param);
>> inv = stable_invC(p, q, param);
```

A sample of `N=500` realizations of the $\alpha$-stable random variable is generated:

```
>> N = 500;
>> seed = 1234;
>> rnd = stable_rndC(p, N, param, seed);
```

From the generated sample, the original parameters are estimated by Koutrouvelis method:

```
>> p_est = stable_koutrouvelisC(rnd)

p_est =

    1.4969    0.5259    0.5246   -0.9508
```

Once the session has finished, the library can be unloaded:

```
>> unloadlibrary('libstable');
```

### 8.5.4 Usage in R environments

A R front-end is also distributed with **Libstable**. In order to use it the shared library and the front-end must be loaded in the current R session by typing:

```
R> dyn.load('/path/to/libstable.so')
R> source('/path/to/libstable.R')
```

The provided functions have a similar syntax as in the MATLAB front-end, and implement the same functionalities. By default, as many threads as available in the system are used.

#### Calculating PDF, CDF and CDF$^{-1}$

The functions

```
pdf  <- stable_pdf(x, pars, parametrization=0, tol=1e-12)
cdf  <- stable_cdf(x, pars, parametrization=0, tol=1e-12)
q    <- stable_q(p, pars, parametrization=0, tol=1e-12)
```

return a vector containing the evaluation of the PDF, CDF and CDF$^{-1}$, respectively, at the points in `x` (`q` for the CDF$^{-1}$). The parameters of the distribution are indicated in the vector `pars`. By default, the indicated parametrization and tolerance are used.

#### Random variable generation

The generation of $\alpha$-stable random variables is provided by the function

```
rnd <- stable_rnd(N, pars, parametrization=0, seed=0)
```

A vector containing `N` independent realizations of an $\alpha$-stable random variable with parameters given in `pars` is returned. The seed to initialize the random numbers generator may be set by `seed`. If not provided, by default it is set by default to the system time.

### Parameter estimation

An R function is provided for each of the estimation methods described in section 8.5.2:

```
p_est <- stable_fit_init(data, p_ini=NULL)
p_est <- stable_fit_koutrouvelis(data, p_ini=NULL)
p_est <- stable_fit_mle(data, p_ini=NULL)
p_est <- stable_fit_mle2d(data, p_ini=NULL)
```

These functions perform McCulloch, Koutrouvelis, ML and modified ML estimation, respectively, in the sample vector `data`. The estimated parameters are returned as a vector. By default the McCulloch estimator is used by the other methods as an initial estimate of the parameters, parameters, but a user defined initial estimate may be specified as an additional argument `p_ini=[alpha_ini, beta_ini, sigma_ini, mu_ini]`, e.g.,

```
p = stable_fit_mle2d(data, p_ini=c(1.45, 0.2, 2.0, 5.0))
```

The following lines illustrate how to use the package in an R session. First, load the shared libray and front-end:

```
R> dyn.load('/path/to/libstable.so')
R> source('/path/to/libstable.R')
```

Define parameter and abscissa vectors and evaluate the PDF and the CDF:

```
R> pars <- c(0.75, 0.5, 1.0, 0.0)
R> x    <- seq(from = -5, to = 10, by = 0.01)
R> pdf  <- stable_pdf(x, pars, parametrization = 0, tol = 1e-12)
R> cdf  <- stable_cdf(x, pars, parametrization = 0, tol = 1e-12)
```

Evaluate the quantile function at desired probabilities:

```
R> p  <- seq(from = 0.01, to = 0.99, by = 0.01)
R> q  <- stable_q(p, pars, parametrization = 0, tol = 1e-12)
```

Generate 500 random samples with given seed and estimate a new parameter vector from the sample with Koutrouvelis method:

```
R> N   <- 500;
R> rnd <- stable_rnd(N, pars, seed = 1234)
R> pars_est <- stable_koutrouvelis(rnd, p_ini = NULL)
```

Unload dynamic library when done

```
R> dyn.unload('/path/to/libstable.so')
```

## 8.6 Conclusions

In this paper, a C/C++ library with interfaces for R and MATLAB to work with $\alpha$-stable distributions have been presented. The method of evaluation of the PDF, CDF and quantile function provided achieves a high precision, in most cases in the same order of magnitude than the widely acknowledged ground truth STABLE program. Based on the methods provided by the library, maximum likelihood and other estimation techniques based on the PDF can also be done in reasonable times. If desired, less accurate estimates can also be obtained with much shorter execution times.

The developed library implements parallelization techniques to carry out its computations. Hence, it can take full advantage of current multi-core systems. Besides, the use of appropriate quadrature techniques and strategies of integration allows us to achieve an increment in performance with respect to current reference software when calculating the PDF with just one thread. As an example, when 16 threads of execution are available, a 25-fold increase in performance is achieved with respect to the program STABLE (Nolan, 2006) for PDF evaluation on the same machine. This improvement in performance reaches a 100-fold increase when compared with the R package **stabledist**.

The tools provided can be easily integrated in third party developments; to that end, we have provided MATLAB and R front-ends through which our library shows no appreciable loss of performance.

(a) PDF

| $\alpha$ | $\beta$ | $x$-axis interval | | |
|---|---|---|---|---|
| | | $[-1000,-10)$ | $[-10,10)$ | $(10,1000]$ |
| 0.25 | 0 | $7.2{\cdot}10^{-16}$ | $6.1{\cdot}10^{-16}$ | $7.2{\cdot}10^{-16}$ |
| | 0.5 | $9.3{\cdot}10^{-16}$ | $7.0{\cdot}10^{-16}$ | $7.0{\cdot}10^{-16}$ |
| | 1 | $--$ | $2.8{\cdot}10^{-16}$ | $5.9{\cdot}10^{-16}$ |
| 0.5 | 0 | $9.6{\cdot}10^{-16}$ | $6.7{\cdot}10^{-16}$ | $9.6{\cdot}10^{-16}$ |
| | 0.5 | $1.3{\cdot}10^{-15}$ | $9.2{\cdot}10^{-16}$ | $8.3{\cdot}10^{-16}$ |
| | 1 | $--$ | $5.8{\cdot}10^{-16}$ | $6.9{\cdot}10^{-16}$ |
| 0.75 | 0 | $2.8{\cdot}10^{-15}$ | $8.4{\cdot}10^{-16}$ | $2.8{\cdot}10^{-15}$ |
| | 0.5 | $6.2{\cdot}10^{-15}$ | $1.1{\cdot}10^{-15}$ | $1.9{\cdot}10^{-15}$ |
| | 1 | $--$ | $9.8{\cdot}10^{-14}$ | $2.0{\cdot}10^{-15}$ |
| 1 | 0 | $--$ | $--$ | $--$ |
| | 0.5 | $2.4{\cdot}10^{-12}$ | $1.3{\cdot}10^{-15}$ | $7.4{\cdot}10^{-13}$ |
| | 1 | $--$ | $8.4{\cdot}10^{-16}$ | $3.1{\cdot}10^{-13}$ |
| 1.5 | 0 | $1.8{\cdot}10^{-13}$ | $1.1{\cdot}10^{-15}$ | $1.8{\cdot}10^{-13}$ |
| | 0.5 | $4.7{\cdot}10^{-14}$ | $1.2{\cdot}10^{-15}$ | $1.9{\cdot}10^{-13}$ |
| | 1 | $--$ | $1.4{\cdot}10^{-15}$ | $3.9{\cdot}10^{-14}$ |

(b) CDF

| $\alpha$ | $\beta$ | $x$-axis interval | | |
|---|---|---|---|---|
| | | $[-1000,-10)$ | $[-10,10)$ | $(10,1000]$ |
| 0.25 | 0 | $1.8{\cdot}10^{-15}$ | $5.4{\cdot}10^{-16}$ | $2.6{\cdot}10^{-16}$ |
| | 0.5 | $2.4{\cdot}10^{-15}$ | $7.9{\cdot}10^{-16}$ | $3.6{\cdot}10^{-16}$ |
| | 1 | $--$ | $1.9{\cdot}10^{-16}$ | $3.4{\cdot}10^{-16}$ |
| 0.5 | 0 | $4.3{\cdot}10^{-15}$ | $5.2{\cdot}10^{-16}$ | $2.3{\cdot}10^{-16}$ |
| | 0.5 | $3.9{\cdot}10^{-15}$ | $5.5{\cdot}10^{-16}$ | $2.6{\cdot}10^{-16}$ |
| | 1 | $--$ | $3.5{\cdot}10^{-16}$ | $2.5{\cdot}10^{-16}$ |
| 0.75 | 0 | $1.6{\cdot}10^{-14}$ | $5.4{\cdot}10^{-16}$ | $2.2{\cdot}10^{-16}$ |
| | 0.5 | $1.8{\cdot}10^{-14}$ | $6.2{\cdot}10^{-16}$ | $2.4{\cdot}10^{-16}$ |
| | 1 | $--$ | $5.4{\cdot}10^{-16}$ | $2.3{\cdot}10^{-16}$ |
| 1 | 0 | $--$ | $--$ | $--$ |
| | 0.5 | $7.3{\cdot}10^{-14}$ | $6.1{\cdot}10^{-16}$ | $8.7{\cdot}10^{-8}$ |
| | 1 | $--$ | $3.8{\cdot}10^{-16}$ | $9.9{\cdot}10^{-8}$ |
| 1.5 | 0 | $6.0{\cdot}10^{-13}$ | $4.8{\cdot}10^{-16}$ | $2.2{\cdot}10^{-16}$ |
| | 0.5 | $1.2{\cdot}10^{-12}$ | $5.7{\cdot}10^{-16}$ | $2.2{\cdot}10^{-16}$ |
| | 1 | $--$ | $5.0{\cdot}10^{-16}$ | $2.2{\cdot}10^{-16}$ |

Table 8.1: Averaged relative error in the calculation of the PDF (a) and CDF (b) of standard $\alpha$-stable distributions in three intervals for a set of $\alpha$ and $\beta$ parameter values.

CHAPTER

# NINE

# CONCLUSIONS AND FUTURE WORK

This Chapter gathers the main contributions of this thesis, limitations of the described approaches and future research lines. References to other related papers in which the PhD candidate has been involved during the completion of this degree are also included.

## 9.1 Contributions

The thesis consists of a methodological *corpus* and a set of results that let us enumerate the following scientific contributions:

1. Motion compensation based on groupwise non-rigid registration improves cine cardiac image reconstruction with respect to both non-ME based techniques and sequential ME techniques.

2. Inclusion of a jacobian weighting in the temporal total variation term eliminates the need of spatial variation in our motion compensated reconstruction procedure.

3. Inclusion of a jacobian weighting in the temporal total variation term provides theoretical support to using forward and backward terms as empirically justified in the literature. This is independent, however, of using groupwise registration procedures as the ME procedure itself.

4. Reconstruction of cine cardiac images with the proposed ME technique and the jacobian weighting term is robust against very different initialization of the algorithm.

5. Our ME reconstruction technique is able of achieving single breath-hold whole heart imaging in acceptable clinical times.

6. Our ME reconstruction technique is able of achieving real-time cardiac 2D imaging in acceptable clinical times with acceptable spatial and temporal resolutions.

7. Inclusion of groupwise ME techniques improves FB reconstruction with respect to currently reported non-ME based techniques.

8. Calculations with *alpha*-stable distributions are feasible with our parallel library, providing high precision and performance tools.

## 9.2 Limitations of the current work

A key component in the MRI reconstruction methods proposed in this thesis is the ME technique applied. This method needs that two regularization weights are selected. Even if the results obtained have shown not to be very sensitive to the specific values of these parameters, it remains unknown whether these values should be modified when the ME method is used in application domains different from estimating the motion of the heart. With respect to this, a method has been proposed by Sanz-Estébanez et al. (2016) in which the regularization parameters are automatically chosen along the ME procedure.

A related limitation is the need for fitting the sparsity regularization weight in the reconstruction. An effort is made in Chapter 5 to find an heuristic rule to select this parameter based on the SNR of the data. However, these experiments are based in synthetically generated data, which are simpler than real images and, consequently, easier to reconstruct. Final results showed than slightly higher values of the parameter should be used when reconstructing real data. Therefore, the optimal selection of the regularization weight is still an open problem.

Another issue has to do with the convergence properties of the iterative reconstruction algorithm proposed, in which two optimization problems are solved

iteratively. The sensitivity of the reconstruction method with respect to the initialization has been tested in Chapter 3, what provides empirical evidence of robustness against getting stacked at a local minimum far from the ideal solution. However, no mathematical proof of convergence is provided.

As a part of the validation procedure, synthetic data generated both with numerical phantoms and from magnitude DICOM images where used in initial experiments. Even if the numerical phantom represents realistic geometries of the internal organs and their motion along both the cardiac and the respiratory cycles, the generated images are much sparser than real MRI data. Moreover, synthetic sensitivity maps are used for the multi–coil data generation, so perfect match —apart from added noise— between data and signal generation model exists. This is not true in real scenarios, in which multiple system imperfections such as gradient non-linearities, delays, errors in the estimated sensitivity maps, etc. are present. However, even taken these limitations into account, all the contributions presented in this Thesis include validation experiments with real data with the exception of the preliminary results presented in Chapter 7.

All the results presented are obtained for 2D modalities in which either just one or several slices are acquired. When several slices are reconstructed, these are processed slice by slice independently. Such an approach presents some implicit limitations:

- Typically, lower SNR is obtained from 2D acquisitions given the smaller amount of tissue excited in thin slices. As shown in Chapter 5, even though the $\ell_1$ norm regularization in CS formulation can mitigate the effect of noise in the data, lower SNR levels leads to reduced quality in the reconstructions.

- A high level of redundancy will be present between consecutive slices, while a *per*-slice approach cannot benefit from it. Therefore, further acceleration factors or better image quality can be expected if several slices are reconstructed jointly.

- *Trough-plane motion* takes place during data acquisition. The effect is more remarked in FB applications, in which the heart is displaced up and down by the diaphragm during respiration, but it is present as well in BH. In this situation, the ME technique will never be able to recover the true motion of the structures being imaged, obtaining just a partial representation of it.

Throuough this Thesis the proposed methods have been compared with CS–based methods in which only sparsity is considered as a regularization term. However, low–rank and PS approaches have not been considered although they have shown promising results in recent years in different MRI applications such as T1 weighted imaging of the brain (Haldar and Zhuo, 2016) and cardiac perfusion analysis (Lingala et al., 2011). PS methods have recently provided extremely high temporal resolution images of the full vocal tract (Fu et al., 2017). Both low–rank and PS methods have been combined with sparse regularizations and successfully applied to cardiac cine (Zhao et al., 2012; Miao et al., 2016), T1 and T2 mapping (Zhao et al., 2015), accelerated 4D flow (Cheng et al., 2016). A multi–scale low–rank approach has been recently introduced by Ong and Lustig (2016) which decomposes the image into different local detail scales. Dictionary learning techniques have also been developed for MRI reconstruction in which the sparse basis is learned from the data (Caballero et al., 2014; Liu et al., 2013; Wang and Ying, 2014) and recently combined with low–rank regularization (Ravishankar et al., 2017). Initial applications of deep learning approaches have also been recently presented by Wang et al. (2016).

On the implementation side, the parallel computations capabilities of modern multi–core systems has been exploited following different approaches. On the one hand the MRI reconstruction methods presented in Chapters 2 to 7 have been implemented in MATLAB, which inherently parallelizes the execution of the code when several cores are available. When handling with $\alpha$–stable distributions in Chapter 8, an explicit parallelization has been implemented with several execution threads launched simultaneously. However, the current implementation of the developed tools cannot take advantage of the GPU processing techniques available nowadays. In the case of $\alpha$–stable distributions, we have extended the proposed library in collaboration with other researchers, as described in Julián-Moreno et al. (2016).

## 9.3 Future Work

One key line of future work will be the extension of the proposed ME and the reconstruction methods to work with 3D acquisitions. These provide higher SNR values, higher acceleration factors given the redundancy between adjacent slices could be achieved and the problems derived from trough-plane motion would be solved. Moreover, a 3D acquisition would enable the application of more versatile

k-space trajectories, as those proposed by Piccini et al. (2011), by Prieto et al. (2015) or by Cheng et al. (2015) than have shown promising results in their application to MR angiography (MRA) and abdominal imaging.

In a multi-slice 2D acquisition a preliminary planning step is needed in which the technician defines the orientation of the planes to be acquired, which is a time consuming procedure in cardiac applications due to the oblique position of the heart and the variability between subjects. Even if the posterior acquisition is accelerated, the time required for planning cannot be avoided. As an additional shortcoming, if some orientation is not acquired during the examination or an error is made, this information will not be available and could only be obtained with a new examination. The development of a highly accelerated dynamic 3D reconstruction method with isotropic resolution could avoid the planning step, since the planing slices could be obtained retrospectively from a high resolution volume oriented according to the canonical planes of the MRI system.

However, even if higher acceleration factors can be achieved, the overall acquisition time needed to reconstruct a complete 3D dynamic volume will increase beyond the breath-hold capability of the subjects. Therefore, the introduction of free-breathing acquisition schemes as the double binning proposed by Feng et al. (2016) will be necessary. In Chapter 7 initial results with the FB acquisition scheme in combination with the developed ME technique are shown for synthetic and healthy volunteer data.

In current cardiac MRI examinations, additional hardware and long setup times are needed for the synchronization of the acquisition with the cardiac and respiratory motion. Some algorithms that are able to recover this synchronization information from the acquired data itself —commonly refereed as *self navigated* methods— have been proposed by Pang et al. (2014) or Coppo et al. (2015). The application of these techniques could help to reduce even further the overall examination time. Actually, in (Royuela-del Val et al., 2017c) we have obtained the respiratory signal out of the data directly.

At the time of writing of this document, the PhD candidate is actively working in the extension of the overall algorithm to 3D acquired data. The immediate drawback of this approach is the drastic increase in computational demands of the algorithm since it has to deal with much larger data amounts and more expensive computations. To this purpose, advanced implementations in modern GPU platforms will be applied to shorten the reconstruction times involved.

The wide range of methods that are being proposed for MRI reconstruction based on low–rank and PS approaches will be considered for future extensions of the developed methods specially to other MRI modalities in which the intensity of the tissues does not remain constant along time (such as perfusion studies) and for which the temporal TV does not fit as an ideal regularization term. Moreover, the inclusion of ME techniques will be studied. As an example of this possibility, Mohsin et al. (2017) have introduced a patch–based regularization scheme in which an implicit motion correction takes place.

Finally, in this work the tools developed for managing $\alpha$–stable distributions and their capability to model biomedical images have not been explored. In particular, totally skewed $\alpha$–stable distributions are well suited to model non–negative signals as proposed by Li et al. (2014), a situation that holds in other image modalities, such as CT. Moreover, recently proposed methods for radiation dose reduction in CT (Koesters et al., 2017) are based on CS in with the images are recovered from just a fraction of the originally needed projections. Therefore, the linkage between a powerful statistical signal model based on $\alpha$–stable distributions and the reconstruction of low dose CT from a reduced number of projections will be considered for future research lines.

# APPENDIX: RESUMEN EN CASTELLANO

La disponibilidad a lo largo de los últimos años de una cada vez mayor capacidad de cómputo ha cambiado la manera en que muchos problemas científico–técnicos pueden ser abordados en la actualidad. En esta Tesis Doctoral se abordan dos problemas de interés pero computacionalmente muy intensivos, a saber, la reconstrucción de imagen por resonancia magnética (IRM) dinámica a partir de datos altamente sub-muestreados y la consecución eficiente del cálculo numérico implicado en el manejo de distribuciones $\alpha$–estables para el modelado estadístico.

Sobre el primer problema, la IRM es actualmente la primera opción en cuanto a técnicas de imagen para el diagnóstico de numerosas enfermedades. Sus principales ventajas son su sobresaliente versatilidad y su capacidad de contraste entre tejidos blandos. Sin embargo, la IRM está a menudo limitada por los largos tiempos requeridos para adquirir toda la información necesaria para reconstruir las imágenes deseadas. Una forma de reducir este tiempo es reducir, a su vez, la cantidad de datos utilizados en la reconstrucción, acortando así la duración del examen. Sin embargo, conforme se reduce la cantidad de datos empleados emergen numerosos artefactos en las imágenes obtenidas. Para eliminarlos, podemos introducir cierto conocimiento a priori o *modelo* acerca de la estructura de las imágenes de interés durante el proceso de reconstrucción.

Uno de los principales objetivos de esta Tesis Doctoral es proporcionar un mejor modelo que los disponibles actualmente. En particular, en la tesis abordamos la reconstrucción de imágenes de resonancia magnética cine del corazón. Esta modalidad es comúnmente empleada para estudiar el movimiento del corazón a lo largo del ciclo cardíaco y para ella proponemos un modelo que toma en consideración no sólo la estructura de las imágenes, sino también el movimiento concreto del corazón que tiene lugar en ellas. El modelo es introducido en un

esquema de reconstrucción de IRM adaptado para diferentes aplicaciones y para la adquisición de las imágenes tanto en apnea como en respiración libre. Mostraremos resultados obtenidos tanto mediante simulación como con adquisiciones *in-vivo* de voluntarios sanos y de pacientes.

Sobre el segundo problema, las distribuciones $\alpha$–estables constituyen una amplia familia de distribuciones de probabilidad de relevancia en varias disciplinas científicas, que han sido propuestas también para el modelado y análisis de imágenes biomédicas así como para la recuperación de señales altamente submuestreads. Sin embargo, la falta de fórmulas cerradas para el cálculo de sus funciones de distribución y de densidad de probabilidad supone una importante limitación en su aplicación práctica. Para el cálculo de estas funciones deben aplicarse métodos numéricos con un elevado coste computacional, lo que dificulta, por ejemplo, la estimación de los parámetros $\alpha$–estables a partir de una muestra.

En esta Tesis Doctoral se proporcionan algunas de las herramientas necesarias para el uso de estas distribuciones como un modelo estadístico de utilidad. Se han desarrollado métodos para el cálculo numérico rápido y preciso de las funciones de distribución y densidad de probabilidad así como para la estimación de los parámetros $\alpha$–estables. Las herramientas desarrolladas hacen uso de las capacidades de cálculo en paralelo presentes en la mayoría de los sistemas de cómputo actuales.

Ambos problemas, aunque de naturalezas bien distintas, comparten el elevado coste computacional implicado como característica común. Se ha prestado por tanto especial atención al desarrollo de implementaciones eficientes en ambas situaciones.

El código generado durante el desarrollo de esta Tesis Doctoral y el material suplementario que puede encontrarse en las versiones digitales de los artículos presentados en esta Tesis Doctoral se han puesto a disposición junto a la versión electrónica de esta memoria así como en la página web del autor en:

`http://www.lpi.tel.uva.es/~jroyval`

Este resumen en castellano se complementa con un resumen de los objetivos, la metodología, los principales resultados y conclusiones de la Tesis Doctoral.

## Objetivos

El objetivo principal de esta Tesis es **proponer y aplicar mejores modelos así como proporcionar las herramientas necesarias para su implementación en dos problemas computacionalmente intensos: la reconstrucción de imágenes por resonancia magnética (IRM) dinámica a partir de datos altamente submuestreados y la aplicación de funciones de distribución $\alpha$–estables para el modelado estadístico**.

El objetivo principal se ha dividido a su vez en los siguientes objetivos individuales:

1. Proponer un mejor modelo para la reconstrucción de IRM dinámica a partir de datos altamente submuestreados que tenga en cuenta no sólo el carácter redundante de las imágenes sino también el movimiento presente en ellas; asimismo se pretende proporcionar las herramientas *software* necesarias para su aplicación.

   Para tal fin se definen los siguientes subobjetivos:

   (a) Proponer e implementar una técnica para la estimación del movimiento cardíaco que sea al mismo tiempo lo suficientemente flexible como para describir el movimiento del corazón y suficientemente robusta frente a los artefactos presentes en imágenes reconstruidas a partir de datos altamente submuestreados.

   (b) Proponer y desarrollar métodos de reconstrucción de IRM dinámica que incorporen el conocimiento sobre el movimiento del corazón con el objetivo de obtener una mejor representación de las imágenes a reconstruir. Se parte de la hipótesis de que esta información permitirá obtener imágenes de mejor calidad y mayores tasas de aceleración.

   (c) Proponer y desarrollar una extensión del método de estimación de movimiento que sea capaz de incorporar no sólo el movimiento del corazón a lo largo del ciclo cardíaco sino también el movimiento introducido por la respiración del paciente.

   (d) Comprobar la viabilidad de los métodos propuestos para obtener indicadores de función cardíaca utilizados comúnmente en la práctica clínica.

(e) Para cada uno de los subobjetivos anteriores, desarrollar una implementación eficiente que explote las capacidades de cálculo en paralelo de los sistemas de cómputo actuales.

2. Desarrollar las herramientas necesarias para aplicar como modelo estadístico las distribuciones $\alpha$–estables de manera viable. Para ello:

   (a) Desarrollar e implementar una técnica para la evaluación numérica de las funciones de densidad de probabilidad, de distribución y percentiles de estas distribuciones que aproveche las capacidades de cálculo en paralelo de los sistemas informáticos actuales.

   (b) Desarrollar e implementar una técnica para la estimación de parámetros de una distribución $\alpha$–estable a partir de una muestra dada.

   (c) Probar el redimiento y precisión de la técnica desarrollada en comparación con otras alternativas disponibles en la literatura.

   (d) Proporcionar una solución *software* de fácil manejo basada en las técnicas desarrolladas e integrar dicha solución en lenguajes de programación comunes y altamente extendidos.

# Metodología

## Imagen por resonancia magnética dinámica 2D

Como se ha descrito en la introducción y objetivos, uno de los principales objetivos de esta tesis es la verificación de la hipótesis de que la incorporacón de un método preciso y robusto de estimación de movimiento cardiaco puede mejorar la calidad de las imágenes reconstruídas.

En primer lugar se ha abordado el problema de la estimación de movimiento cardíaco. Se ha adaptado una técnica previamente propuesta para la estimación de desalineamientos entre cortes cardíacos a la estimación de movimiento cardíaco no rígido en IRM cine. El método resultante se ha introducido en un esquema basado en muestreo compresivo para la reconstrucción de vistas en eje corto del corazón. Se ha conseguido así mejorar los resultados obtenidos por las técnicas descritas hasta el momento. El capítulo 2, que constituye el primer artículo fundamental de esta Tesis, describe estas ideas.

El método anteriormente descrito requiere introducir dos términos de regularización (espacial y temporal), que implica la necesidad de ajustar parámetros libres a partir de datos de entrenamiento. Esta situación se ha mejorado proponiendo una modificación del término de regularización descrita en el capítulo 3, que constituye el segundo artículo fundamental de esta Tesis.

Los métodos anteriores están basados en la adquisición de datos siguiendo una trayectoria cartesiana. Se ha añadido la posibilidad de emplear estrategias de adquisición más avanzadas, basadas en trayectorias radiales, que han permitido elevar la tasa de aceleración alcanzable y, en particular, reconstruir 12 cortes cardíacos cubriendo completamente el corazón a partir de datos adquiridos en una única apnea de un voluntario sano. El capítulo 4 describe el resultado de este trabajo.

El siguiente paso ha consistido en la introducción del esquema de adquisición radial en la metodología descrita en el capítulo 3. Se ha completado la validación de la propuesta comprobando la robustez del método de estimación de movimiento y de reconstrucción frente al ruido, para lo que se han realizado simulaciones basadas en un fantoma numérico. La validez del método para la cuantificación de la función cardíaca global se ha comprobado a partir del examen de ocho voluntarios sanos. Los detalles se incluyen en el capítulo 5.

Se ha adaptado también el método propuesto para la reconstrucción retrospectiva de datos de IRM de tiempo real. En este caso, en contraposición a lo expuesto anteriormente, el paciente respira libremente y el movimiento respiratorio deberá ser descrito junto al cardíaco. Se ha propuesto una pirámide multirresolución temporal en la que se realizan reconstrucciones sucesivas de resolución temporal progresivamente mayor a partir de reconstrucciones anteriores más groseras. Se ha alcanzado una resolución temporal de 25 ms con una resolución espacial en el plano de 2 mm, con mejor calidad que métodos relacionados. Este trabajo se detalla en el capítulo 6.

A pesar de que los resultados previos permiten observar el corazón en respiración libre, el reducido tiempo de adquisición disponible para cada imagen, dado por la resolución temporal deseada, limita la calidad de las imágenes. Para evitar esta limitación se ha seguido en esta ocasión una metodología diferente. Los datos adquiridos se han clasificado doblemente de acuerdo a las fases cardíaca y respiratoria en las que fueron adquiridos. De esta forma 1) el tiempo de adquisición para cada imagen no está limitado por la capacidad de apnea del paciente ni por la resolución temporal objetivo y 2) ahora los movimientos cardíaco

y respiratorio pueden ser distinguidos y estimados por separado. En el capítulo 7 se muestran resultados obtenidos en datos sintéticos y en un voluntario sano.

### Distribuciones $\alpha$–estables

Como se ha indicado anteriormente, los cálculos relacionados con las distribuciones $\alpha$-estables implican un elevado coste computacional. La contribución realizada en este ámbito se enmarca en la programación paralela. En concreto, se ha desarrollado una librería *software* que permite la evaluación rápida, en paralelo y con una alta precisión de las funciones de distribución y de densidad de probabilidad, el cálculo de percentiles, la generación de variables aleatorias y la estimación de parámetros. En las pruebas realizadas se ha alcanzado una reducción de los tiempos de ejecución en un factor 25 con respecto a una aplicación compilada existente y de un factor 100 con respecto a una implementación en el lenguaje de programación R. Estas contribuciones se describen en el capítulo 8 que constituye el tercer artículo fundamental de esta Tesis.

## Conclusiones

Esta sección recopila las principales contribuciones de esta Tesis y posibles líneas futuras de trabajo.

### Contribuciones

1. La compensación de movimiento grupal mejora la reconstrucción de IRM cine cardíaco con respecto a técnicas sin compensación de movimiento o con compensación de movimiento secuencial.

2. La inclusión del jacobiano de la deformación como término de ponderación en el cálculo de la variación total temporal elimina la necesidad de regularización espacial adicional.

3. La inclusión del jacobiano de la deformación proporciona un soporte teórico al empleo de transformaciones secuenciales progresivas y regresivas, justificados únicamente de forma empírica en la literatura.

4. La técnica de reconstrucción desarrollada permite realizar un examen multicorte del corazón completo en una única apnea, en tiempos aceptables para la práctica clínica.

5. La técnica de estimación de movimiento grupal permite realizar IRM de tiempo real 2D con resoluciones espacial y temporal aceptables para la práctica clínica.

6. La introducción de técnicas de estimación de movimiento grupal mejora la reconstrucción de IRM cine 2D en respiración libre con respecto a las técnicas sin compensación de movimiento previamente reportadas.

7. El empleo de distribuciones $\alpha$–estable como modelo estadístico es realizable en tiempos de ejecución razonables mediante la librería paralela desarrollada para tal fin, la cual proporciona resultados de alta precisión y un rendimiento mayor que las opciones disponibles hasta el momento.

### Líneas futuras

Los resultados presentados en esta Tesis se restringen a aplicaciones 2D, en los que o bien se excita un único corte o se adquieren de forma secuencial un conjunto de éstos, los cuales se procesarían independientemente. Esta aproximación presenta ciertas limitaciones:

- Típicamente, en modalidades 2D se obtendrán relaciones de señal a ruido menores que en modalidades 3D debido al pequeño grosor de los cortes excitados.

- Entre cortes consecutivos existirá una alta redundancia, la cual ha sido ignorada.

- El movimiento en la dirección perpendicular al corte no puede ser recuperado por la técnica de estimación de movimiento e incorporado en la reconstrucción.

Debido a las limitaciones anteriores, se plantea la extensión a 3D de las técnicas desarrolladas como línea futura de desarrollo. Además, la aproximación 3D permitirá la aplicación de técnicas de adquisición de datos más avanzadas

disponibles en la literatura, como las propuestas por Piccini et al. (2011), Prieto et al. (2015) o Cheng et al. (2015).

En una examen tradicional multicorte 2D se requiere de una etapa de planificación previa a la adquisición de los datos para seleccionar la orientación de los cortes, su extensión y su número. El desarrollo de una técnica 3D con resolución isotrópica permitiría la eliminación de esta etapa previa, al poder obtener un volumen completo 3D dinámico a partir del cual obtener tantos cortes de interés como se deseen tras la adquisición.

En el caso 3D, a pesar de las altas tasas de aceleración, se requerirán tiempos de examen elevados, más allá de la capacidad de apnea del paciente. Por tanto, será necesario introducir esquemas de respiración libre. Se cuenta ya con experiencia previa para el caso 2D con datos sintéticos, presentada en el capítulo 7, y con datos reales de un voluntario sano enviados para su presentación en una conferencia internacional (Royuela-del Val et al., 2017c).

En los exámenes de IRM cardíacos actuales se requiere de equipamiento adicional para la sincronización de la captación de datos con los movimientos cardíaco y respiratorio. En la actualidad se han propuesto diversos algoritmos que permiten obtener esta información a partir de los propios datos adquiridos —normalmente denominados métodos auto-navegados—, como los propuestos por Pang et al. (2014) y Coppo et al. (2015). En el trabajo Royuela-del Val et al. (2017c) la señal respiratoria se ha obtenido ya a partir de los propios datos.

En el trabajo presentado en el capítulo 8 sobre el desarrollo de una biblioteca para el manejo de distribuciones $\alpha$–estables se ha explotado la capacidad de cálculo en paralelo de sistemas con múltiples núcleos. Sin embargo, la implementación actual no aprovecha las técnicas de cálculo en unidades de procesamiento gráfico (GPU) disponibles. Se ha extendido la librería desarrollada al cálculo en GPU en colaboración con otros investigadores, como se describe en el artículo de Julián-Moreno et al. (2016).

En el momento de escribir este documento, se está trabajando activamente en la extensión 3D de los algoritmos de reconstrucción de IRM propuestos en su conjunto. Una dificultad inmediata al plantear dicha extensión es el drástico incremento en los requerimientos de cálculo, por lo que se aplicarán las técnicas de cálculo en GPU mencionadas para reducir los tiempos de reconstrucción resultantes.

Por último, en este trabajo no se ha explorado la aplicación de las distribiciones $\alpha$–estables al modelado y análisis de imagen médica mediante las herramientas desarrolladas. En particular, las distribuciones $\alpha$–estables totalmente asimétricas son buenas candidatas para modelar señales no negativas (Li et al., 2014), como la obtenida en tomografía asistida por ordenador (TAC). Un método propuesto recientemente por Koesters et al. (2017) se basa en la teoría de muestreo compresivo para desarrollar una técnica de reconstrucción TAC que permite reducir sensiblemente la dosis de radiación recibida por el paciente debido a la menor cantidad de proyecciones necesaria. Por lo tanto, la relación entre un modelo estadístico basado en distribuciones $\alpha$–estables y la reconstrucción de TAC de baja dosis de radiación a partir de un número reducido de projecciones será considerado para líneas de investigación futuras.

# BIBLIOGRAPHY


Adluru, G., McGann, C., Speier, P., Kholmovski, E. G., Shaaban, A., and DiBella, E. V. (2009). Acquisition and reconstruction of undersampled radial data for myocardial perfusion magnetic resonance imaging. *Journal of Magnetic Resonance Imaging*, 29(2):466–473.

Amdahl, G. M. (1967). Validity of the single processor approach to achieving large scale computing capabilities. In *Proceedings of the Spring Joint Computer Conference*, pages 483–485, New York, NY, USA. Association for Computing Machinery.

Asif, M. S., Hamilton, L., Brummer, M., and Romberg, J. (2013). Motion-adaptive spatio-temporal regularization for accelerated dynamic MRI. *Magnetic Resonance in Medicine*, 70(3):800–812.

Avants, B. B., Tustison, N. J., Song, G., Cook, P. A., Klein, A., and Gee, J. C. (2011). A reproducible evaluation of ANTs similarity metric performance in brain image registration. *Neuroimage*, 54(3):2033–2044.

Barney, B. (2011). *POSIX Threads Programming Tutorial*. Lawrence Livermore National Laboratory, Livermore, CA, USA.

Bauer, P., Thorpe, A., and Brunet, G. (2015). The quiet revolution of numerical weather prediction. *Nature*, 525(7567):47–55.

Beatty, P. J., Nishimura, D. G., and Pauly, J. M. (2005). Rapid gridding reconstruction with a minimal oversampling ratio. *IEEE Transactions on Medical Imaging*, 24(6):799–808.

Becker, S., Bobin, J., and Candès, E. (2011). Nesta: A fast and accurate first-order method for sparse recovery. *SIAM Journal on Imaging Sciences*, 4(1):1–39.

Beister, M., Kolditz, D., and Kalender, W. A. (2012). Iterative reconstruction methods in X-ray CT. *Physica Medica*, 28(2):94–108.

Belov, I. (2005). On the computation of the probability density function of $\alpha$-stable distributions. In *Proceedings of the 10th International Conference of Mathematical Modelling and Analysis*, pages 333–341, Trakai, Lithuania.

Bhatia, K. K., Hajnal, J. V., Puri, B. K., Edwards, A. D., and Rueckert, D. (2004). Consistent groupwise non-rigid registration for atlas construction. In *Proceedings of the 2nd IEEE International Symposium on Biomedical Imaging: From Nano to Macro*, pages 908–911, Arlington, VA, USA.

Bogaert, J., Dymarkowski, S., Taylor, A. M., and Muthurangu, V., editors (2012). *Clinical Cardiac MRI*. Springer-Verlag, Berlin, Germany, second edition.

Borak, S., Misiorek, A., and Weron, R. (2011). Models for heavy-tailed asset returns. In *Statistical Tools for Finance and Insurance*, pages 21–55. Springer-Verlag, Berlin, Germany.

Buehrer, M., Pruessmann, K. P., Boesiger, P., and Kozerke, S. (2007). Array compression for MRI with large coil arrays. *Magnetic Resonance in Medicine*, 57(6):1131–9.

Caballero, J., Price, A. N., Rueckert, D., and Hajnal, J. V. (2014). Dictionary learning and time sparsity for dynamic mr data reconstruction. *IEEE Transactions on Medical Imaging*, 33(4):979–994.

Candès, E. J., Romberg, J., and Tao, T. (2006). Robust uncertainty principles: Exact signal reconstruction from highly incomplete frequency information. *IEEE Transactions on Information Theory*, 52(2):489–509.

Chambers, J. M., Mallows, C. L., and Stuck, B. W. (1976). A method for simulating stable random variables. *Journal of the American Statistical Association*, 71(354):340–344.

Chandarana, H., Block, T. K., Rosenkrantz, A. B., Lim, R. P., Kim, D., Mossa, D. J., Babb, J. S., Kiefer, B., and Lee, V. S. (2011). Free-breathing radial

3d fat-suppressed t1-weighted gradient echo sequence: a viable alternative for contrast-enhanced liver imaging in patients unable to suspend respiration. *Investigative Radiology*, 46(10):648–653.

Chen, X., Salerno, M., Yang, Y., and Epstein, F. H. (2014). Motion-compensated compressed sensing for dynamic contrast-enhanced MRI using regional spatiotemporal sparsity and region tracking: block low-rank sparsity with motion-guidance (BLOSM). *Magnetic Resonance in Medicine*, 72(4):1028–1038.

Cheng, J. Y., Hanneman, K., Zhang, T., Alley, M. T., Lai, P., Tamir, J. I., Uecker, M., Pauly, J. M., Lustig, M., and Vasanawala, S. S. (2016). Comprehensive motion-compensated highly accelerated 4d flow mri with ferumoxytol enhancement for pediatric congenital heart disease. *Journal of Magnetic Resonance Imaging*, 43(6):1355–1368.

Cheng, J. Y., Zhang, T., Ruangwattanapaisarn, N., Alley, M. T., Uecker, M., Pauly, J. M., Lustig, M., and Vasanawala, S. S. (2015). Free-breathing pediatric mri with nonrigid motion correction and acceleration. *Journal of Magnetic Resonance Imaging*, 42(2):407–420.

Coppo, S., Piccini, D., Bonanno, G., Chaptinel, J., Vincenti, G., Feliciano, H., van Heeswijk, R. B., Schwitter, J., and Stuber, M. (2015). Free-running 4d whole-heart self-navigated golden angle mri: Initial results. *Magnetic Resonance in Medicine*, 74(5):1306–1316.

Cordero-Grande, L., del Val, J. R., Sanz-Estébanez, S., Martín-Fernández, M., and Alberola-López, C. (2016). Multi-oriented windowed harmonic phase reconstruction for robust cardiac strain imaging. *Medical Image Analysis*, 29:1–11.

Cordero-Grande, L., Merino-Caviedes, S., Aja-Fernández, S., Alberola-López, C., and Alberola-lo, C. (2013). Groupwise Elastic Registration by a New Sparsity-Promoting Metric: Application to the Alignment of Cardiac Magnetic Resonance Perfusion Images. *IEEE Transactions on Pattern Analysis and Machine Intelligence*, 35(11):2638–2650.

Cordero-Grande, L., Vegas-Sanchez-Ferrero, G., de-la Higuera, P. C., and Alberola-Lopez, C. (2012). A markov random field approach for topology-preserving registration: Application to object-based tomographic image interpolation. *IEEE Transactions on Image Processing*, 21(4):2047–2061.

De Craene, M., Piella, G., Camara, O., Duchateau, N., Silva, E., Doltra, A., D'hooge, J., Brugada, J., Sitges, M., and Frangi, A. (2012). Temporal diffeomorphic free-form deformation: Application to motion and strain estimation from 3D echocardiography. *Medical Image Analysis*, 16(2):427–450.

Doneva, M., Nielsen, T., and Boernert, P. (2012). Parameter-Free Compressed Sensing Reconstruction using Statistical Non-Local Self-Similarity Filtering. In *Proceedings of the 20th Annual Meeting of the International Society of Magnetic Resonance in Medicine*, page 74, Melbourne, Australia.

Donoho, D. L. (2006). Compressed sensing. *IEEE Transactions on Information Theory*, 52(4):1289–1306.

Fama, E. (1965). The behavior of stock-market prices. *The Journal of Business*, 38(1):34–105.

Fama, E. and Roll, R. (1971). Parameter estimates for symmetric stable distributions. *Journal of the American Statistical Association*, 66(334):331–338.

Fan, Z. (2006). Parameter estimation of stable distributions. *Communications in Statistics - Theory and Methods*, 35(2):245–255.

Feng, L., Axel, L., Chandarana, H., Block, K. T., Sodickson, D. K., and Otazo, R. (2016). Xd-grasp: Golden-angle radial mri with reconstruction of extra motion-state dimensions using compressed sensing. *Magnetic Resonance in Medicine*, 75(2):775–788.

Feng, L., Grimm, R., Tobias Block, K., Chandarana, H., Kim, S., Xu, J., Axel, L., Sodickson, D. K., and Otazo, R. (2014). Golden-angle radial sparse parallel MRI: Combination of compressed sensing, parallel imaging, and golden-angle radial sampling for fast and flexible dynamic volumetric MRI. *Magnetic Resonance in Medicine*, 72(3):707–717.

Feng, L., Srichai, M. B., Lim, R. P., Harrison, A., King, W., Adluru, G., Dibella, E. V. R., Sodickson, D. K., Otazo, R., and Kim, D. (2013). Highly accelerated real-time cardiac cine MRI using k–t SPARSE-SENSE. *Magnetic Resonance in Medicine*, 70(1):64–74.

Free Software Foundation (2007). GNU General Public License, version 3.

Fu, M., Barlaz, M. S., Holtrop, J. L., Perry, J. L., Kuehn, D. P., Shosted, R. K., Liang, Z.-P., and Sutton, B. P. (2017). High-frame-rate full-vocal-tract 3d dynamic speech imaging. *Magnetic Resonance in Medicine*, 77(4):1619–1629.

Galassi, M., Davies, J., Theiler, J., Gough, B., Jungman, G., Booth, M., and Rossi, F. (2009). *GNU Scientific Library Reference Manual*. Network Theory Limited, Bristol, UK, 3rd edition.

Geyer, L. L., Schoepf, U. J., Meinel, F. G., John W. Nance, J., Bastarrika, G., Leipsic, J. A., Paul, N. S., Rengo, M., Laghi, A., and Cecco, C. N. D. (2015). State of the art: Iterative CT reconstruction techniques. *Radiology*, 276(2):339–357. PMID: 26203706.

Gonchar, V. Y., Chechkin, A. V., Sorokovoĭ, E. L., Chechkin, V. V., Grigor'eva, L. I., and Volkov, E. D. (2003). Stable Lévy Distributions of the Density and Potential Fluctuations in the Edge Plasma of the U–3M Torsatron. *Plasma Physics Reports*, 29(5):380–390.

Górska, K. and Penson, K. A. (2011). Lévy stable two-sided distributions: Exact and explicit densities for asymmetric case. *Physical Review E*, 83:061125.

Haldar, J. P. and Zhuo, J. (2016). P-loraks: Low-rank modeling of local k-space neighborhoods with parallel imaging data. *Magnetic Resonance in Medicine*, 75(4):1499–1514.

Hill, B. M. (1975). A simple general approach to inference about the tail of a distribution. *The Annals of Statistics*, pages 1163–1174.

Huang, F., Akao, J., Vijayakumar, S., Duensing, G. R., and Limkeman, M. (2005). k-t GRAPPA: A k-space implementation for dynamic MRI with high reduction factor. *Magnetic Resonance in Medicine*, 54(5):1172–1184.

Irarrazaval, P., Boubertakh, R., Razavi, R., and Hill, D. (2005). Dynamic three-dimensional undersampled data reconstruction employing temporal registration. *Magnetic Resonance in Medicine*, 54(5):1207–1215.

Julián-Moreno, G., López de Vergara, J. E., González, I., de Pedro, L., Royuela-del Val, J., and Simmross-Wattenberg, F. (2016). Fast parallel $\alpha$–stable distribution function evaluation and parameter estimation using OpenCL in GPGPUs. *Statistics and Computing*.

Jung, H., Sung, K., Nayak, K. S., Kim, E. Y., and Ye, J. C. (2009). k-t FOCUSS: A general compressed sensing framework for high resolution dynamic MRI. *Magnetic Resonance in Medicine*, 61(1):103–116.

Jung, H. and Ye, J. C. (2010). Motion estimated and compensated compressed sensing dynamic magnetic resonance imaging: What we can learn from video compression techniques. *Int J Imag Syst Tech*, 20(2):81–98.

Jung, H., Ye, J. C., and Kim, E. Y. (2007). Improved k–t BLAST and k–t SENSE using FOCUSS. *Physics in Medical Biology*, 52(11):3201–3226.

Kamesh Iyer, S., Tasdizen, T., and Dibella, E. V. R. (2012). Edge-enhanced spatiotemporal constrained reconstruction of undersampled dynamic contrast-enhanced radial MRI. *Magnetic Resonance Imaging*, 30(5):610–619.

Knoll, F., Bredies, K., Pock, T., and Stollberger, R. (2011). Second order total generalized variation (TGV) for MRI. *Magnetic Resonance in Medicine*, 65(2):480–491.

Koesters, T., Knoll, F., Sodickson, A., Sodickson, D. K., and Otazo, R. (2017). Sparsect: interrupted-beam acquisition and sparse reconstruction for radiation dose reduction. In *Proc. SPIE 10132, Medical Imaging 2017: Physics of Medical Imaging, 101320Q (March 10, 2017)*, pages 101320Q–101320Q–7.

Koutrouvelis, I. A. (1981). An iterative procedure for the estimation of the parameters of stable laws. *Communications in Statistics - Simulation and Computation*, 10(1):17–28.

Lévy, P. (1925). *Calcul des Probabilités*. Gauthier-Villars, Paris, France.

Li, P., Samorodnitsk, G., and Hopcroft, J. (2013). Sign cauchy projections and chi-square kernel. In *Advances in Neural Information Processing Systems*, pages 2571–2579, Harrahs and Harveys, Lake Tahoe, NV, USA.

Li, P., Zhang, C.-H., and Zhang, T. (2014). Compressed counting meets compressed sensing. In *Journal of Machine Learning Research: Workshop and Conference Proceedings*, pages 1–20.

Liang, D., Liu, B., Wang, J., and Ying, L. (2009). Accelerating sense using compressed sensing. *Magnetic Resonance in Medicine*, 62(6):1574–1584.

Liang, Y. and Chen, W. (2013). A survey on computing lévy stable distributions and a new MATLAB toolbox. *Signal Processing*, 93:242–251.

Liang, Z.-P. (2007). Spatiotemporal imaging with partially separable functions. In *2007 4th IEEE International Symposium on Biomedical Imaging: From Nano to Macro*, pages 988–991.

Lingala, S., DiBella, E. V., and Jacob, M. (2014). A generalized motion compensated compressed sensing scheme for highly accelerated myocardial perfusion MRI. *Journal of Cardiovascular Magnetic Resonance*, 16(Suppl 1):W23.

Lingala, S. G., DiBella, E., and Jacob, M. (2015). Deformation corrected compressed sensing (DC-CS): a novel framework for accelerated dynamic MRI. *IEEE Transactions on Medical Imaging*, 34(1):72–85.

Lingala, S. G., Hu, Y., DiBella, E., and Jacob, M. (2011). Accelerated dynamic mri exploiting sparsity and low-rank structure: k-t slr. *IEEE Transactions on Medical Imaging*, 30(5):1042–1054.

Liu, Q., Wang, S., Ying, L., Peng, X., Zhu, Y., and Liang, D. (2013). Adaptive dictionary learning in sparse gradient domain for image recovery. *IEEE Transactions on Image Processing*, 22(12):4652–4663.

Lustig, M., Donoho, D., and Pauly, J. M. (2007). Sparse MRI: The application of compressed sensing for rapid MR imaging. *Magnetic Resonance in Medicine*, 58(6):1182–1195.

Madore, B., Glover, G. H., and Pelc, N. J. (1999). Unaliasing by fourier-encoding the overlaps using the temporal dimension (unfold), applied to cardiac imaging and fmri. *Magnetic Resonance in Medicine*, 42(5):813–828.

Magarey, J. and Kingsbury, N. (1998). Motion estimation using a complex-valued wavelet transform. *IEEE Transactions on Signal Processing*, 46(4):1069–1084.

Mandelbrot, B. B. and Wallis, J. R. (1968). Noah, Joseph, and operational hydrology. *Water Resources Research*, 4:909–918.

McCulloch, J. H. (1986). Simple consistent estimators of stable distribution parameters. *Communications in Statistics - Simulation and Computation*, 15(4):1109–1136.

Menn, C. and Rachev, S. T. (2006). Calibrated FFT-based density approximations for $\alpha$-stable distributions. *Computational Statistics & Data Analysis*, 50(8):1891–1904.

Metz, C., Klein, S., Schaap, M., van Walsum, T., and Niessen, W. (2011). Nonrigid registration of dynamic medical imaging data using nD + t B-splines and a groupwise optimization approach. *Medical Image Analysis*, 15(2):238–249.

Miao, X., Lingala, S. G., Guo, Y., Jao, T., Usman, M., Prieto, C., and Nayak, K. S. (2016). Accelerated cardiac cine {MRI} using locally low rank and finite difference constraints. *Magnetic Resonance Imaging*, 34(6):707 – 714.

Mittnik, S., Doganoglu, T., and Chenyao, D. (1999a). Computing the probability density function of the stable Paretian distribution. *Mathematical and Computer Modelling*, 29(10–12):235–240.

Mittnik, S., Rachev, S., Doganoglu, T., and Chenyao, D. (1999b). Maximum likelihood estimation of stable paretian models. *Mathematical and Computer Modelling*, 29(10–12):275–293.

Mohsin, Y. Q., Lingala, S. G., DiBella, E., and Jacob, M. (2017). Accelerated dynamic mri using patch regularization for implicit motion compensation. *Magnetic Resonance in Medicine*, 77(3):1238–1248.

Nocedal, J. and Wright, S. (1999). *Numerical Optimization*. Springer-Verlag, Berlin, Germany.

Nolan, J. P. (1997). Numerical calculation of stable densities and distribution functions. *Stochastic Models*, 13(4):759–774.

Nolan, J. P. (1999). An algorithm for evaluating stable densities in Zolotarev's (M) Parameterization. *Mathematical and Computer Modelling*, 29(10–12):229–233.

Nolan, J. P. (2001). Maximum likelihood estimation and diagnostics for stable distributions. In Barndorff-Nielsen, O. E., Mikosch, T., and Resnick, S. I., editors, *Lévy Processes: Theory and Applications*, pages 379–400. Birkhäuser, Boston, MA, USA.

Nolan, J. P. (2006). *Users Guide for STABLE 4.0.xx*. Available online at http://academic2.american.edu/∼jpnolan/stable/stable.html.

Ong, F. and Lustig, M. (2016). Beyond low rank + sparse: Multiscale low rank matrix decomposition. *IEEE Journal of Selected Topics in Signal Processing*, 10(4):672–687.

Otazo, R., Kim, D., Axel, L., and Sodickson, D. K. (2010). Combination of compressed sensing and parallel imaging for highly accelerated first-pass cardiac perfusion MRI. *Magnetic Resonance in Medicine*, 64(3):767–776.

Pang, J., Sharif, B., Fan, Z., Bi, X., Arsanjani, R., Berman, D. S., and Li, D. (2014). Ecg and navigator-free four-dimensional whole-heart coronary mra for simultaneous visualization of cardiac anatomy and function. *Magnetic Resonance in Medicine*, 72(5):1208–1217.

Piccini, D., Littmann, A., Nielles-Vallespin, S., and Zenge, M. O. (2011). Spiral phyllotaxis: the natural way to construct a 3D radial trajectory in MRI. *Magnetic resonance in medicine*, 66(4):1049–56.

Press, W., Teukolsky, S., Vetterling, W., and Flannery, B. (1994). *Numerical Recipes in C: The Art of Scientific Computing*. Cambridge University Press, Cambridge, UK, 2nd edition.

Prieto, C., Batchelor, P. G., Hill, D., Hajnal, J. V., Guarini, M., and Irarrazaval, P. (2007). Reconstruction of undersampled dynamic images by modeling the motion of object elements. *Magnetic Resonance in Medicine*, 57(5):939–949.

Prieto, C., Doneva, M., Usman, M., Henningsson, M., Greil, G., Schaeffter, T., and Botnar, R. M. (2015). Highly efficient respiratory motion compensated free-breathing coronary mra using golden-step cartesian acquisition. *Journal of Magnetic Resonance Imaging*, 41(3):738–746.

Pruessmann, K. P., Weiger, M., Börnert, P., and Boesiger, P. (2001). Advances in sensitivity encoding with arbitrary k-space trajectories. *Magnetic Resonance in Medicine*, 46(4):638–651.

Pruessmann, K. P., Weiger, M., Scheidegger, M. B., and Boesiger, P. (1999). SENSE: Sensitivity encoding for fast MRI. *Magnetic Resonance in Medicine*, 42(5):952–962.

Ravishankar, S., Moore, B. E., Nadakuditi, R. R., and Fessler, J. A. (2017). Low-rank and adaptive sparse signal (lassi) models for highly accelerated dynamic imaging. *IEEE Transactions on Medical Imaging*, 36(5):1116–1128.

R Core Team (2015). *R: A Language and Environment for Statistical Computing*. R Foundation for Statistical Computing, Vienna, Austria.

Royuela-del Val, J., Cordero-Grande, L., Simmross-Wattenberg, F., Martín-Fernández, M., and Alberola-López, C. (2016a). Nonrigid groupwise registration for motion estimation and compensation in compressed sensing reconstruction of breath-hold cardiac cine MRI. *Magnetic Resonance in Medicine*, 75(4):1525–1536.

Royuela-del Val, J., Cordero-Grande, L., Simmross-Wattenberg, F., Martín-Fernández, M., and Alberola-López, C. (2017a). Jacobian weighted temporal total variation for motion compensated compressed sensing reconstruction of dynamic mri. *Magnetic Resonance in Medicine*, 77(3):1208–1215.

Royuela-del Val, J., Martín-Fernández, M., Simmross-Wattenberg, F., and Alberola-López, C. (2016b). Cardio-respiratory motion estimation for compressed sensing reconstruction of free-breathing 2d cine mri. In *Proceedings of the International Workshop on Imaging with Modulated/Incomplete Data. Graz University of Technology*, Graz, Austria.

Royuela-del Val, J., Simmross-Wattenberg, F., and Alberola-López, C. (2017b). Libstable: Fast, Parallel and High-Precision Computation of alpha-Stable Distributions in C, MATLAB and R. *Journal of Statistical Software*. (In press).

Royuela-del Val, J., Usman, M., Cordero-Grande, L., Simmross-Wattenberg, F., Martín-Fernández, M., Prieto, C., and Alberola-López, C. (2015). Single breath hold whole heart cine MRI with iterative groupwise cardiac motion compensation and sparse regularization (kt-WiSE). In *Proceedings of the 23rd Annual Meeting of the International Society of Magnetic Resonance in Medicine*, page 572, Toronto, CA.

Royuela-del Val, J., Usman, M., Cordero-Grande, L., Simmross-Wattenberg, F., Martín-Fernández, M., Prieto, C., and Alberola-López, C. (2016c). Multiresolution Reconstruction of Real-Time MRI with Motion Compensated Compressed Sensing: Application to 2D Free-Breathing Cardiac MRI. In *Proceedings of the 13th IEEE International Symposium on Biomedical Imaging: From Nano to Macro*.

Royuela-del Val, J., Usman, M., Cordero-Grande, L., Simmross-Wattenberg, F., Martín-Fernández, M., Prieto, C., and Alberola-López, C. (2016d). Whole-

heart single breath-hold cardiac cine: A robust motion-compensated compressed sensing reconstruction method. In *Proceedings of the 19th International Conference on Medical Image Computing & Computer Assisted Intervention. 1st International Workshop on Reconstruction and Analysis of Moving Body Organs (MICCAI/RAMBO 2016)*.

Royuela-del Val, J., Usman, M., Cordero-Grande, L., Simmross-Wattenberg, F., Martín-Fernández, M., Prieto, C., and Alberola-López, C. (2017c). Cardiorespiratory motion estimation for compresssed sensing reconstruction of free-breathing 2D cine MRI. In *Proceedings of the 25th annual meeting of the International Society of Magnetic Resonance in Medicine*, Honolulu, HW, USA. (Accepted).

Rueckert, D., Sonoda, L., Hayes, C., Hill, D., Leach, M., and Hawkes, D. (1999). Nonrigid registration using free-form deformations: application to breast MR images. *IEEE Transactions on Medical Imaging*, 18(8):712–721.

Salas-Gonzalez, D., Górriz, J., Ramírez, J., Schloegl, M., Lang, E., and Ortiz, A. (2013). Parameterization of the distribution of white and grey matter in MRI using the $\alpha$-stable distribution. *Computers in Biology and Medicine*, 43(5):559–567.

Salas-Gonzalez, D., Kuruoglu, E. E., and Ruiz, D. P. (2009). Finite mixture of $\alpha$–stable distributions. *Digital Signal Processing*, 19(2):250–264.

Samorodnitsky, G. and Taqqu, M. S. (1994). *Stable non-Gaussian Random Processes: Sstochastic Models with Infinite Variance*. Chapman and Hall/CRC, Boca Raton, CA, USA.

Sanz-Estébanez, S., Royuela-del Val, J., Sevilla, T., Revilla-Orodea, A., Aja-Fernández, S., and Alberola-López, C. (2016). Harmonic auto – regularization for non rigid groupwise registration in cardiac magnetic resonance imaging. In *Proceedings of the XXXIV Annual Congress of the Spanish Society of Biomedical Engineering (CASEIB)*.

Segars, W. P., Sturgeon, G., Mendonca, S., Grimes, J., and Tsui, B. M. W. (2010). 4D XCAT phantom for multimodality imaging research. *Medical Physics*, 37(9):4902–15.

Selesnick, I., Baraniuk, R., and Kingsbury, N. (2005). The dual-tree complex wavelet transform. *IEEE Signal Processing Magazine*, 22(6):123–151.

Simmross-Wattenberg, F., Asensio-Pérez, J. I., Casaseca-de-la-Higuera, P., Martín-Fernández, M., Dimitriadis, I. A., and Alberola-López, C. (2011). Anomaly detection in network traffic based on statistical inference and $\alpha$-stable modeling. *IEEE Transactions on Dependable and Secure Computing*, 8(4):494–509.

The MathWorks, Inc. (2013). *MATLAB – The Language of Technical Computing, Version 8.2.0*. Natick, MA, USA.

Tsao, J., Boesiger, P., and Pruessmann, K. P. (2003). k-t BLAST and k-t SENSE: Dynamic MRI with high frame rate exploiting spatiotemporal correlations. *Magnetic Resonance in Medicine*, 50(5):1031–1042.

Tsao, J. and Kozerke, S. (2012). MRI temporal acceleration techniques. *Journal of Magnetic Resonance Imaging*, 36(3):543–560.

Uecker, M., Zhang, S., and Frahm, J. (2010). Nonlinear inverse reconstruction for real-time MRI of the human heart using undersampled radial FLASH. *Magnetic resonance in medicine*, 63(6):1456–1462.

Uecker, M., Zhang, S., Voit, D., Merboldt, K.-D., and Frahm, J. (2012). Real-time MRI: recent advances using radial FLASH. *Imaging in Medicine*, 4(4):461–476.

Usman, M., Atkinson, D., Odille, F., Kolbitsch, C., Vaillant, G., Schaeffter, T., Batchelor, P. G., and Prieto, C. (2013). Motion corrected compressed sensing for free-breathing dynamic cardiac MRI. *Magnetic Resonance in Medicine*, 70(2):504–516.

Vegas-Sánchez-Ferrero, G., Simmross-Wattenberg, F. J., Martín-Fernández, M., Palencia, C., and Alberola-López, C. (2012). Caracterización de speckle con modelos de cola pesada. In *Proceedings of the XXX Annual Congress of the Spanish Society of Biomedical Engineering (CASEIB)*, San Sebastián, Spain.

Veillette, M. S. (2010). Alpha-stable distributions in MATLAB. Available on line at http://math.bu.edu/people/mveillet/research.html. Last access dec 2016.

Vincenti, G., Monney, P., Chaptinel, J., Rutz, T., Coppo, S., Zenge, M. O., Schmidt, M., Nadar, M. S., Piccini, D., Chèvre, P., Stuber, M., and Schwitter, J. (2014). Compressed Sensing Single–Breath-Hold CMR for Fast Quantification of LV Function, Volumes, and Mass. *JACC: Cardiovascular Imaging*, 7(9):882–892.

Vlaardingerbroek, M. T. and Boer, J. A. (2003). *Magnetic Resonance Imaging: Theory and practice*. Springer-Verlag, Berlin, Germany, third edition.

Wang, S., Su, Z., Ying, L., Peng, X., Zhu, S., Liang, F., Feng, D., and Liang, D. (2016). Accelerating magnetic resonance imaging via deep learning. In *2016 IEEE 13th International Symposium on Biomedical Imaging (ISBI)*, pages 514–517.

Wang, Y. and Ying, L. (2014). Compressed sensing dynamic cardiac cine mri using learned spatiotemporal dictionary. *IEEE Transactions on Biomedical Engineering*, 61(4):1109–1120.

Wang, Z., Bovik, A. C., Sheikh, H. R., and Simoncelli, E. P. (2004). Image quality assessment: From error visibility to structural similarity. *IEEE Transactions on Image Processing*, 13(4):600–612.

Weron, R. (1996). On the Chambers-Mallows-Stuck method for simulating skewed stable random variables. *Statistics & Probability Letters*, 28(2):165–171.

Weron, R. (2004). Computationally intensive Value at Risk calculations. In Gentle, J., Härdle, W., and Mori, Y., editors, *Handbook of Computational Statistics*, pages 911–950. Springer-Verlag, Berlin, Germany.

Willinger, W., Taqqu, M. S., Sherman, R., and Wilson, D. V. (1997). Self–Similarity Through High–Variability: Statistical Analysis of Ethernet LAN Traffic at the Source Level. *IEEE/ACM Transactions on Networking*, 5(1):71–86.

Winkelmann, S., Schaeffter, T., Koehler, T., Eggers, H., and Doessel, O. (2007). An Optimal Radial Profile Order Based ont the Golden Ratio for Time-Resolved MRI. *IEEE Transactions on Medical Imaging*, 26(1):68–76.

Wissmann, L., Santelli, C., Segars, W. P., and Kozerke, S. (2014). MRXCAT: Realistic numerical phantoms for cardiovascular magnetic resonance. *Journal of Cardiovascular Magnetic Resonance*, 16(1):63.

Yoon, H., Kim, K. S., Kim, D., Bresler, Y., and Ye, J. C. (2014). Motion adaptive patch-based low-rank approach for compressed sensing cardiac cine MRI. *IEEE Transaction on Medical Imaging*, 33(11):2069–2085.

Zhao, B., Haldar, J. P., Christodoulou, A. G., and Liang, Z. P. (2012). Image reconstruction from highly undersampled (k, t)-space data with joint partial separability and sparsity constraints. *IEEE Transactions on Medical Imaging*, 31(9):1809–1820.

Zhao, B., Lu, W., Hitchens, T. K., Lam, F., Ho, C., and Liang, Z.-P. (2015). Accelerated mr parameter mapping with low-rank and sparsity constraints. *Magnetic Resonance in Medicine*, 74(2):489–498.

Zolotarev, V. M. (1986). *One-Dimensional Stable Distributions*, volume 65 of *Translations of Mathematical Monographs*. American Mathematical Society, Ann Arbor, MI, USA.